

Diluted magnetic semiconductor Resonant Tunneling Structures for spin manipulation

**A Thesis submitted for the degree
of Doctor of Philosophy**

**Bavarian Julius–Maximilians–Universität
Würzburg**

submitted by

Anatoliy Slobodskyy

Würzburg, February 2005

Submitted:

Faculty of physic and astronomy

1. Supervisor: Prof. Dr. L.W. Molenkamp

for the dissertation

1. Prüfer:

2. Prüfer:

for oral exam

Day of the oral exam:

Doktorurkunde ausgehändigt am:

Contents

1	Introduction.	1
1.1	Spin electronics.	1
1.2	Spin injection and manipulation.	3
1.3	Spin detection.	4
2	Theory of Resonant tunneling.	7
2.1	Resonant tunneling.	7
2.1.1	Basics of resonant tunneling.	7
2.1.2	Coherent versus incoherent resonant tunneling process.	16
2.1.3	Elastic and inelastic scattering mechanisms, phonon replica.	20
2.2	Magnetic field influence on RTDs.	22
2.2.1	Magnetic field perpendicular to the QW.	22
2.2.2	Magnetic field in-plane of the QW.	24
3	Experiment.	27
3.1	Diluted magnetic semiconductors.	27
3.1.1	Giant Zeeman splitting.	27
3.1.2	[Zn,Be,Mn]Se DMS.	29

3.2	Setup and sample design.	32
3.2.1	Measurement setup and technique.	32
3.2.2	Charges in a RTD.	33
3.2.3	Multistabilities in resonant tunneling structures.	34
3.2.4	Sample design.	37
4	Spin selection in RTDs with magnetic QW.	39
4.1	Introduction.	39
4.2	Details of the experiment.	41
4.3	Results and simulation of spin resolved current through the device.	42
4.4	Summary.	47
5	RTD with magnetic QW as a spin detector.	49
5.1	Spin polarization at high magnetic field.	49
5.2	Influence of spin-polarized current on RTDs I-V characteristics.	50
5.3	Temperature dependence of the effect.	53
6	Double RTD with magnetic QWs for current spin polarization and detection.	57
7	RTD with magnetic injector or barriers for spin manipulation.	61
7.1	Introduction and the magnetic injector sample design.	61
7.2	Magnetic field induced change of I-V characteristic of RTD structure with magnetic injector.	63
7.3	Explanation of magnetic field influence on the transport in RTD with magnetic injector.	64
7.4	RTD with magnetic barriers for spin manipulation.	67

8 Spin resolved resonant tunneling in self-assembled quantum dots.	71
8.1 Self-Assembled II-V Quantum Dot as a Voltage-Controlled Spin-Filter.	71
8.2 Sample and measurements details.	72
8.3 Magnetic field evolution of the resonance peaks.	73
8.4 Understanding the effect of an external magnetic field.	75
Summary	79
Zusammenfassung	83
Bibliography	95

Chapter 1

Introduction.

1.1 Spin electronics.

Spin electronics, or in short spintronics, is a multidisciplinary field whose central theme is the active manipulation of the freedom of spin degree of charge carriers in solid-state systems. The generation of spin polarization usually means creating a nonequilibrium spin population. This can be achieved in several ways. Traditionally, spin has been oriented using optical techniques in which circularly polarized photons transfer their angular momenta to electrons, for device applications, however, electrical spin injection is more desirable. In electrical spin injection, a magnetic electrode is connected to the sample. When the current drives spin-polarized electrons from the electrode to the sample, nonequilibrium spin accumulates at the interface. The rate of spin accumulation is decreased by spin relaxation, the process of bringing the accumulated spin population back to equilibrium.

Injection and detection of a spin-polarized current in semiconductors was successfully demonstrated by R. Fiederling et al. [FKR⁺99], achieving a high spin injection efficiency of more than 90% as detected by electroluminescence emitted from a [Al,Ga]As light-emitting diode (LED). The experiment was carried out with a [Zn,Be,Mn]Se spin aligner to inject polarized electrons into the diode (LED).

A step towards understanding the process of electrical spin injection was made by G. Schmidt et al. [SFM⁺00]. They showed that the very low efficiency of electrical spin injection from ferromagnetic metals into semiconductor is explained in terms of conductance mismatch. In the nonmagnetic semiconductor, the conductance of both spin channels is identical and the difference in the conductance of spin channels in ferromagnetic metal causes the spin-polarization of the current. Due to a large conductance mismatch between metal and semiconductor, electron transport through the spin channels is totally dominated by the conductance of semiconductor. This fact limits the use of ferromagnetic metals as a material for spintronics, not only because of the relatively low $\sim 45\%$ spin-polarization of carriers within the ferromagnet, but also because

of the low resistance of the spin injecting metal as compared to the semiconductor into which the spin-polarized electrons are to be injected.

Although, ferromagnetic metals have a high Curie temperature which gives possibility for spin manipulation at room temperature without external magnetic field. An effective way to overcome the conductivity mismatch problem is to use 100% spin-polarized materials. One of the promising families of materials in this sense, are half metals, Heusler alloys [dGMvE83]. Half metal means that the only available states at the Fermi level in these materials are spin-polarized, resulting in 100% spin polarization. Moreover, the materials are ferromagnetic at room temperatures.

Another big issue in the field of spintronics in recent years is to design new ferromagnetic semiconductor materials with room temperature ferromagnetism. In order to achieve ferromagnetic behaviour, semiconductors are diluted with magnetic ions to make diluted magnetic semiconductors (DMS). The advantage of DMS, compared to metals, is that conductivity of the injector is similar to that of the nonmagnetic semiconductor used in applications, and in this way the conductance mismatch problem can be overcome.

Applications of spin electronics are successfully used in the "read" heads for magnetic hard disk drives, because of extreme sensitivity to external magnetic field. The effect used is known as giant magnetoresistance (GMR) [BBF⁺88] and results from the effect of the scattering of electrons on the interface of alternate ferromagnetic/paramagnetic layers. Depending on parallel or anti-parallel orientation of the layers, the resistance of the structure will be changed. The interfaces are normally used with a tunnel barrier in order to increase the effect and are called tunneling magnetoresistance (TMR). At the same time, GMR based random access memory (RAM), magnetic random access memory (MRAM), and computer hard disks are under rapid development.

A long-term goal for spintronics applications is quantum computation [LD98, Kan98]. The quantum algorithms require that the internal state of the quantum computer will be controlled with extraordinary precision, so that the coherent quantum state, upon which the quantum algorithms rely, is not destroyed.

In this thesis, we will discuss our recent results of measurements and simulation of magnetic RTD structures as possible applications for semiconductor spintronics. The thesis is organized as follows: In chapter 1 we discuss the principles of spin injection and manipulation. Chapter 2 reviews the theory of resonant tunneling. In chapter 3 we describe the details of the experiment. In the subsequent chapters we show our experiment results on spin selection (chapter 4) and spin detection (chapter 5), in all-II-VI RTD with magnetic QW, a two parallel RTD system (chapter 6), spin manipulation with RTDs with magnetic injector or barriers (chapter 7), and spin resolved resonant tunneling in self-assembled quantum dots (chapter 8). An overview of the results is presented as the summary. Finally, we present related results on "Spin Injection in the Nonlinear Regime: Band Bending Effects" as an appendix.

1.2 Spin injection and manipulation.

In 1990, Datta and Das proposed a design for a spin-polarized field-effect transistor, or SFET [DD90]. In a conventional FET, a narrow semiconductor channel runs between two electrodes - source and drain. When voltage is applied to the gate electrode, which is above the channel, the resulting electric field drives electrons out of the channel (for instance), turning the channel into an insulator. The Datta-Das spin FET has a spin-polarizer source and drain so that the current flowing into the channel is spin-polarized. When a voltage is applied to the gate, the spins rotate as they pass through the channel and the drain rejects these anti-aligned electrons. Naturally, in order to achieve proper spin selectivity at the drain, transport of the carriers must be quantum mechanically coherent. Flipping an electron's spin takes much less energy and can be done much faster than pushing an electron out of the channel. One can also imagine changing the orientation of the source or drain with a magnetic field, introducing an additional type of control: logic gates whose functions can be changed on the fly.

One of the most important and at the same time most complicated tasks in such kind of devices is to inject and manipulate spin-polarized electric current in the nonmagnetic media. Using DMS or Heusler alloys not necessarily means that 100% of spin-polarized current can be injected, because of the scattering on interface states. High electric-field diffusive regime, which has no analogue in metals, was shown to improve the spin injection efficiency [YF02]. The idea is that at reasonably high electric-fields, the spin-diffusion lengths will be different for different spin oriented currents. The enhancement of the spin injection efficiency also occurs for high electric-field spin injection through a spin-selective interfacial barrier. Additional interface effects and effects of band bending are analysed in [SGG⁺04].

There are many options to manipulate spin within the NMS. One of the effects being explored in order to manipulate spin within the material is the fact that in the presence of an electric field, the spin and momentum states of an electron can be coupled; this is known as spin-orbit (SO) coupling. An important SO coupling effect induced by structural inversion asymmetry is known as the Rashba effect [Ras60a, Ras60b, BR84]. Due to the Rashba SO interaction in a two-dimensional electron gas (2DEG) where an interfacial electric-field, arising from an asymmetric confining potential, is present, a momentum dependent splitting between the two spin directions appears. It is typically more important in small-gap zinc-blend-type semiconductors because of the proximity of the valence band and can be tuned by external electric fields (gate voltages). The Dresselhaus SO coupling is due to bulk inversion asymmetry and the interface inversion asymmetry [Dre55].

Quantum dots (QD) are considered an important instrument to manipulate spin orientation of current [RSL00]. The quantum coulomb blockade regime is assumed in order to incorporate the functionality of the quantum mechanical device. This puts additional limitations on the conditions at which the device could be operated. These conditions limit the use of the spin selector to very low temperatures (dilution refrigerators) and the injector Fermi energy must be smaller than the splitting of the levels in the QW. At the same time the spin injection from a ferromagnetic source into a semiconductor through a paramagnetic ion-doped nanocrystal

[ERR01] can either enhance the injection coefficient by several times or suppress it, depending on voltage.

1.3 Spin detection.

Very convincing optical methods of spin detection are proven to be useful [FKR⁺99]. Time-resolved photoluminescence also gives the possibility of following the dynamics of a spin over time, that allows the investigation of basic properties of structures for spintronics [MBSA01]. Effective optical detection of the spin injection is realised through measurements of the Hanle effect. The effect uses the degree of circular polarization of photons from recombination to measure the component of carrier spin along the direction of observation. For the Hanle effect, magnetic field B must have a component perpendicular to the orientation axes of the injected spins. Only projection of B perpendicular to the spin axis applies a torque and dephases the spins. There is a discrepancy in how to interpret the circular polarized light out of Spin-LED. In particular, the publication from Y. Ohno et al. [OYB⁺99] is based on the measurement of side emitted light. This quasi-Voigt geometry gives rise to different selection rules for optical transitions in GaAs based QWs compared to those applicable for top emission. This discrepancy was analysed in [FGO⁺03] where no significant effect of spin-polarized current in the side emitted light is seen.

One needs electrical methods of efficient spin detection in order to effectively implement it to devices. In external magnetic fields and in low temperatures, one could use diluted magnetic semiconductor. The spin-polarized materials alone are not spin detectors. In order to detect current spin-polarization one needs some strong indication of the spin current itself. Search for reliable spin-polarized current detectors has also stimulated the development of a novel detection technique that uses scanning tunneling spectroscopy combined with pulsed quasiparticle spin injection to minimize Joule heating. However, for a quantitative interpretation of the measured polarization, important additional factors need to be considered. For example, the Fermi surface may not be spherical, or the magnetic resonance force microscopy MRFM is very precise and allows single spin detection [RBMC04].

Several spin diodes have recently been proposed or demonstrated with the goal of either maximising the sensitivity of the current-voltage (I-V) characteristics to spin and magnetic field, or facilitating spin injection and its detection through semiconductor interfaces comprising a magnetic semiconductor as the injector. Magnetic tunneling diodes have been used for spin injection from a ferromagnetic to a nonmagnetic semiconductor, in p-GaMnAs/n-GaAs p-n junctions [KOT⁺01, JHLK⁺02, DLR⁺04]

Spin resonant tunneling diodes demonstrated in [SGS⁺03] have strong spin splitting of the levels in the QW that can be positively used for spin detection. The spin dependent transport trough the device is obvious and is easy to observe, even at intermediate fields and helium temperatures. Properly understanding and explaining the effect of the spin resolved transport makes

it possible to control the detected spin orientation by applying voltage to the device. Miniaturisation of the devices can lead to the possibility of integrating it into practical realisation schemes.

Chapter 2

Theory of Resonant tunneling.

2.1 Resonant tunneling.

2.1.1 Basics of resonant tunneling.

Studies of superlattices were launched by the work of L. Esaki and R. Tsu (1970) [ET70], who considered the electron transport in a superlattice, i.e. in an additional periodic potential created by doping or changing the composition of semiconductor materials with the period larger than, but comparable to, the lattice constant of crystal. In this “man-made crystal,” as Esaki called it, a parabolic band breaks into minibands separated by small forbidden gaps with Brillouin zones determined by this period.

Later, Tsu and Esaki considered resonant tunneling in superlattice structures [TE73] where they assumed a finite superlattice and calculated the tunneling probability for the structure using the transfer matrix method. The authors show the presence of a negative differential resistance (NDR) and resonant peaks in the current-voltage (I-V) characteristics.

The first experimental demonstration of quantum well (QW) heterostructure physics was done by (Chang et al., 1974) [CET74]. They measured the tunneling current and conductance as a function of an applied voltage in GaAs-GaAlAs double barriers and found current maxima associated with resonant tunneling. Later in the same year Esaki and Chang (1974) [EC74] observed resonant tunneling in superlattices that typically comprised of fifty periods.

To understand the principles of the resonant tunneling peak formation in the I-V characteristic of a resonant tunneling diode (RTD) let us look at the simplified picture that is shown in Fig. 2.1

A schematic drawing of an RTD is shown in Fig. 2.1(a). The device consists of five components. 1) Doped injector. 2) First tunnel barrier. 3) Quantum well with quantized states. 4) Second

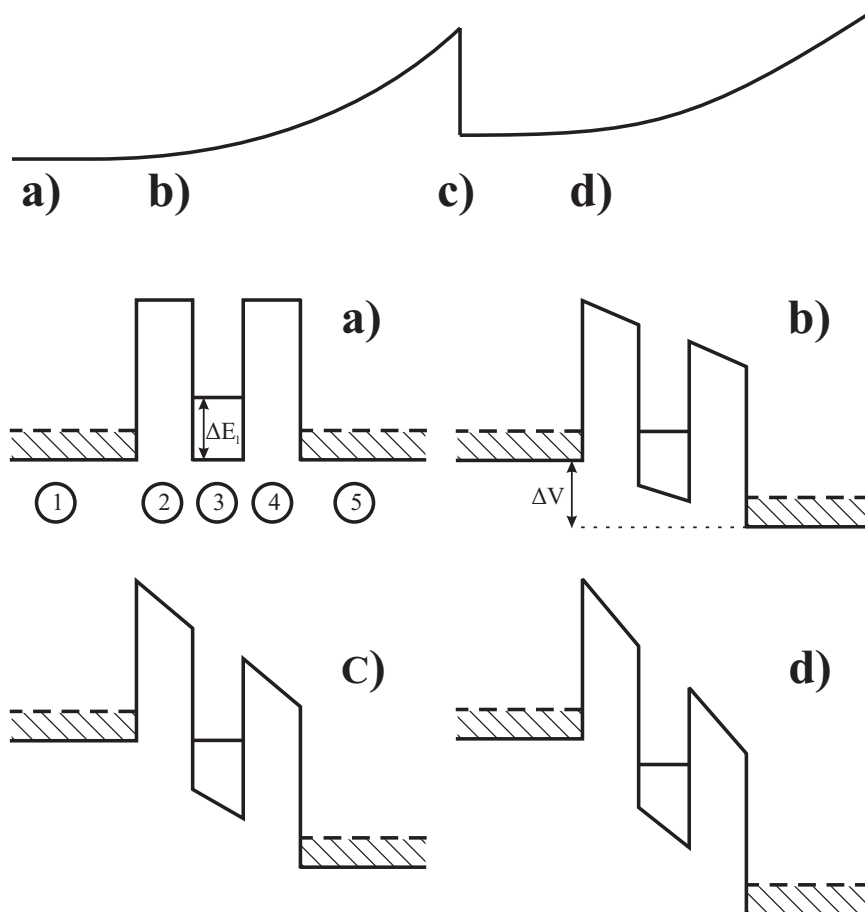


Figure 2.1: The principles of resonant tunneling. a) Double barrier quantum well structure at 0 bias. b) The structure at bias ΔV . Level in the quantum well is aligned with the Fermi level in the injector. Resonant current begins to flow. c) At a higher bias the bottom of the conduction band in the injector is aligned with the level in the quantum well. Maximum resonant current. d) Increased bias pushes the level in the quantum well below the occupied states in the injector. Resonant current does not flow in this configuration.

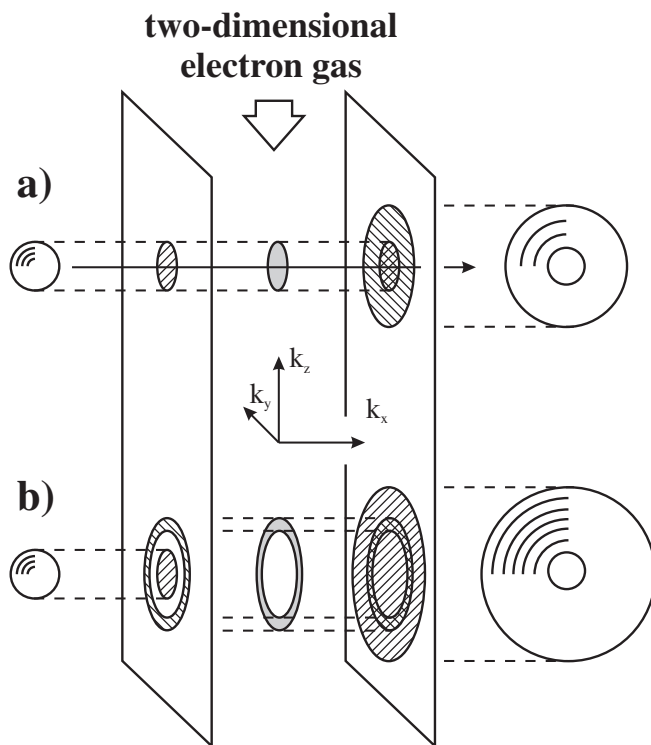


Figure 2.2: L. Esaki's picture of resonant tunneling. Construction of shadows of energy surfaces on two k_y - k_z planes corresponding to two barriers. a) RTD at resonance bias. b) The structure out of resonance.

tunnel barrier. 5) Doped collector.

Because of the quantization of the states in the quantum well and energy conservation during tunneling process, tunneling electrons passing the first barrier cannot find states in the QW with the appropriate energy and resonant tunneling is suppressed.

At a bias ΔV across the structure, as shown in Fig. 2.1(b) the energy shift of the levels in the QW with respect to the injector is $\sim e\Delta V/2$, for a symmetric structure. When the level in the QW is aligned in energy with the Fermi level in the injector, the resonant tunneling current starts to flow and defines the beginning of the resonant peak in the I-V characteristic.

As the applied voltage is increased, the resonant tunneling current increases and reaches its maximum at the point where the level in the quantum well reaches the bottom of the injector conduction band as it is shown in Fig. 2.1(c). From this simple picture one can see that the voltage difference from the beginning of the resonant peak to its maximum point is basically twice the Fermi energy in the injector divided by e .

At an even higher bias the level in the quantum well is moved below the conduction band levels in the injector (see Fig. 2.1(d)) and the resonant tunneling current turns off.

A similar but more detailed picture of the process of resonant tunneling is presented in Fig. 2.2. This picture was presented by L. Esaki in his Nobel Lecture, 1973 "Long journey into tunneling" [Esa73]. In addition to energy conservation during the tunneling process that is discussed in Fig. 2.1 the Esaki picture adds the idea of in-plane momentum conservation.

In the figure, the two k_y - k_z planes correspond to the two barriers in the RTD structure. The sphere on the left side of the double barrier structure represents a Fermi sphere in the injector. The sphere on the right side of the structure represents an energy sphere in which electrons have the same total energies as electrons in the Fermi sphere on the left. The ring structure between the barrier planes depicts the DOS in the quantum well.

The overlap between the levels in the injector, quantum well and collector is shown by the overlap of their projections onto the planes of the barriers. The two conditions of energy and k -vector conservation are thus satisfied.

Fig. 2.2(a) presents the resonant tunneling structure under resonance conditions, where the overlap of the projections of the Fermi sphere in the injector and the two-dimensional DOS in the QW onto the plane of the first tunnel barrier is obvious. The energy sphere in the collector is big enough to overlap with both projections of the DOS. The maximum resonant tunneling current will flow through the structure in this configuration.

Fig. 2.2(b) presents the RTD out of resonance. The overlap between the injector DOS and the DOS in the QW is absent. The ring structure in the QW is formed because the only states presented are the two dimensional states with the energies of the tunneling electrons. This representation corresponds to the total energy conservation during tunneling process. Although there is an overlap between the DOS in the QW and the collector, the resonant condition that requires an overlap of the states on both barriers is broken. At higher bias voltages, the radius of the DOS ring in the QW will increase and the radius of the energy sphere in the collector will increase even more. The resonance current will therefore reach a maximum when the radius of the DOS in the QW is equal to the radius of the Fermi sphere in the injector and will abruptly vanish after this. An important property of the RTD structure shown in the figure is the width of the allowed energy states in the QW. It shows that, due to broadening, the states have some width and distribution which play a role on the device I-V characteristic.

The next sophistication to the description was brought by S. Luryi in 1985 [Lur85] and is depicted in Fig. 2.3. His idea includes all that is previously presented and introduces the influence of band banding and the effect of density of states in the injector.

At zero bias the resonant state in the QW is higher in energy than the levels in the injector and the tunneling current does not flow through the system. The situation is depicted in Fig. 2.3(a) in the same manner as was shown in Fig. 2.1(a).

At bias V , as shown in Fig. 2.3(b), the tunneling electrons will have states available in the QW and a resonant tunneling current will flow through the structure. The situation is similar to the one depicted in Fig. 2.1(b)(c) except that in this case a charge accumulation region is shown in the injector area just before the first barrier. This feature is very important and can dramatically change the properties of the device. Very often, a two-dimensional electron gas (2DEG) is formed in the charge accumulation region and the picture of resonant tunneling must be treated with a two-dimensional DOS in the injector instead of a Fermi sphere. In the present example, we consider the case that no 2DEG is yet formed. This is also the case for the experimental

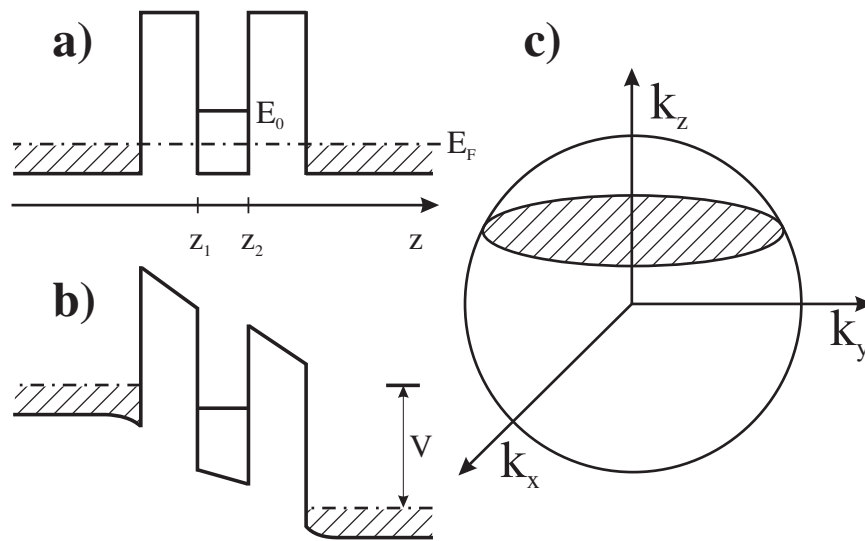


Figure 2.3: *S. Luryi's picture of resonant tunneling. a) RTD without bias. E_F - Fermi energy. E_0 - quantized energy level in the QW. b) The structure at the resonance. V - applied bias. c) k -vector representation of the resonant condition in the structure.*

structures we study later in this thesis.

On the collector side of the structure, a depletion region is formed just after the second tunnel barrier. The main influence of this feature is that the shape of the second barrier is changed, this also has an influence on the resonant tunneling current because, as it will be shown, an important requirement for high resonant tunneling current is symmetry between the barriers.

In Fig. 2.3(c), the sphere represents the Fermi sphere in the injector and the shaded area is the overlap in energy between the sphere and the plane of the QW energy level. The shaded area represents the states in the injector from which the electrons can take part in the resonant tunneling process. The energy level in the QW is presented as a plane in k_x - k_y . This is correct according to the parabolic band approximation. The shaded area will be shifted down in k_z at higher bias.

As one can see with increased bias the overlap area between the Fermi sphere and the level in the QW will be increased, thus indicating increased number of states taking part in the resonant tunneling and thus increased current flow.

When the plane of the level in the QW crosses zero k_z , the negative states can no longer take part in the tunneling process and the resonant current does not flow through the structure.

From the diagrams previously considered, one can conclude that the I-V characteristics of an RTD should have peaks that begin at the point when the level in the QW is aligned with the Fermi level in the injector and they have a maximum when the bottom of the conduction band in the injector is aligned with the level in the QW. Thereafter the current should stop and only increase again when the second QW level is aligned with the states in the injector.

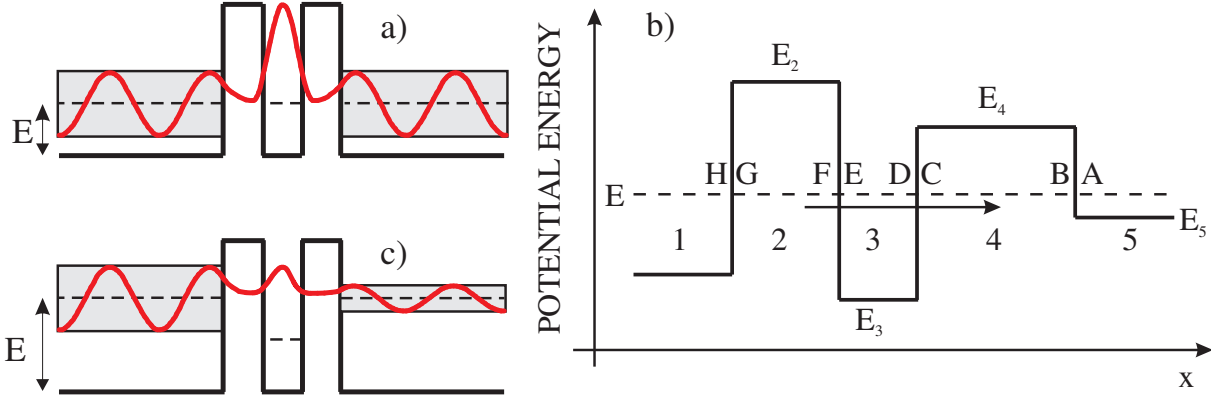


Figure 2.4: Wave function across an asymmetric RTD structure a) at resonant conditions, c) out of resonant conditions along with b) the structure of asymmetric RTD.

In comparison with a Fabry-Perot resonator in optics, one can expect a resonant enhancement of the tunneling current in RTD at certain voltages. This occurs when the energy of an incident electron (one near the Fermi level in the emitter) matches that of the unoccupied state in QW corresponding to the same lateral momentum. Under such conditions, the amplitude of the resonant mode builds up in the QW to the extent that the wave, leaking in both directions, practically cancels the incident wave and enhances the transmitted one. The diagram is schematically depicted in Fig. 2.4(a) and shows that the tunneling probability for such a device can be as big as one.

According to Ricco and Ya. Azbel in [RA84] and Kane [Kan69], for the potential-energy diagram of Fig. 2.4(b), the global transmission coefficient T_G of the whole barrier (i.e. from points H to A) can be exactly derived and given by:

$$T_G = \frac{C_0}{C_1 T_l T_r + C_2 \frac{T_l}{T_r} + C_3 \frac{T_r}{T_l} + C_4 \frac{1}{T_l T_r}} \quad (2.1)$$

where T_l and T_r represent the transmission coefficient of the left and right barrier respectively, (between points G-F and C-B) and are exponentially dependent on energy. In Eq. (2.1) the C_i are (phase) factors which are exhibiting much weaker energy dependence and, in primary order, can essentially be treated as constants (of the same order of magnitude). Let us consider the case of “strong localization” which requires all T 's to be small ($\ll 1$). Under this condition, the denominator of Eq. (2.1) is dominated by the last term, and the global transmission coefficient T_G simplifies to the “normal” transmission coefficient T_{GN} corresponding to T_G in the absence of a resonance

$$T_{GN} \approx \frac{C_0}{C_4} T_l T_r \approx T_l T_r \quad (2.2)$$

In this case, the presence of the potential-energy well between the two barriers has, in practice, little or no effect. In particular, it were as if points E and D in Fig. 2.4 (b) were coincidental and no well was present. This suppresses the tunneling probability as shown in Fig. 2.4(c)

The energy levels E_n of a finite square-well potential of width L and depth V_0 are given by [Sch68]

$$E_n = \frac{\hbar^2}{2m(L/2)^2} \xi_n^2 \quad (2.3)$$

for $n = 1, 2, \dots$, where ξ_n denotes one of the positive solutions of

$$\begin{cases} \xi \tan \xi = \sqrt{A^2 - \xi^2} & \text{for } n \text{ odd} \\ \xi \cot \xi = -\sqrt{A^2 - \xi^2} & \text{for } n \text{ even,} \end{cases}$$

where

$$A \equiv \frac{L/2}{\hbar} \sqrt{2mV_0}$$

At the energies calculated from Eq. (2.3), the coefficient C_4 in Eq. (2.1) goes to zero; the leading term is consequently cancelled out, and a resonance occurs. In this case, as seen from Eq. (2.1), the global (resonance) transmission coefficient T_{Gres} becomes

$$T_{Gres} \approx C \frac{T_{min}}{T_{max}} \approx \frac{T_{min}}{T_{max}} \quad (2.4)$$

where T_{min} and T_{max} represent the smaller and larger among T_l and T_r , respectively, while C is either C_0/C_2 or C_0/C_3 depending on whether $T_{max} = T_l$ or T_r .

By directly comparing Eqs. (2.2) and (2.4) it is obvious that the resonance always implies an increased transmission coefficient since the ratio is

$$T_{Gres}/T_{GN} = 1/T_{max}^2 \quad (2.5)$$

Such an increase is, therefore, greater for the smaller T_{max} and vanishes in the limiting case of $T_{max} \rightarrow 1$ (which, on the other hand, is incompatible with the assumption of strong localization).

At the resonant energies defined by Eq. (2.3) T_{Gres} there is unity when $T_l = T_r$. Eq. (2.5) clearly indicates that the transmission coefficient can easily increase by several orders of magnitude for arbitrary small changes in T_{max} .

Because T_l and T_r are non zero, the localised states are, strictly speaking, quasi eigenstates with a finite lifetime and energy width. The assumption of strong localisation, however, implies that they can be considered as “real” eigenstates for all practical purposes.

The peak produced by the resonance in the transmission coefficient and (hence in the measured currents) has a finite energy width ΔE which is physically due to the non zero probability of tunneling out of the well. Such a width is related to the (resonant) state lifetime and is termed “natural (homogeneous) broadening”. For this reason, ΔE increases with the electron escape probability, thus essentially with T_{max} [RA84],

$$\Delta E \propto T_{max} \quad (2.6)$$

The finite width of the resonance peaks plays a relevant role in experiments. It makes the energy matching condition required to produce a resonance less critical (although the amplitude of the effect decreases away from the level centre).

An illustration of the ideas described by Eqs. (2.2), (2.4) and (2.6) is presented in Fig. 2.5. The previous conclusions were done on the basis of the WKB approximation, which is not an exact solution, they are perfectly valid for small energies (smaller than the height of the barriers). In particular, as one can see from the figure, the tunneling probability for the RTD of the resonance and for the single barrier are similar at low energies.

Spreading in the particle energies will cause broadening of the resonance. Assuming that the electron distribution can be considered constant over the whole ΔE , the current contribution due to the resonant peak is

$$J_{res} \propto T_{max} \frac{T_{min}}{T_{max}} \quad (2.7)$$

where the first term accounts for the fraction of electrons involved and the second represents the global transmission coefficient at resonances. Without resonance the same amount of carriers would produce a current J_{off} , given by

$$J_{off} \propto T_{max}^2 T_{min} \quad (2.8)$$

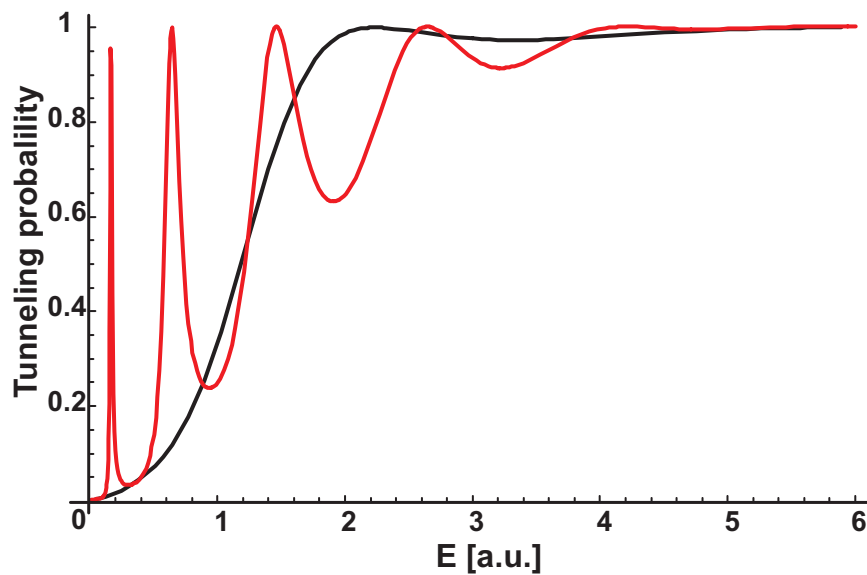


Figure 2.5: Tunneling probability of an symmetric RTD solved by transfer matrix method (red line) as compared with tunneling probability of a single tunnel barrier (without QW - black line).

It is then obvious that a resonance can give rise to an extremely large current increase.

$$\frac{J_{res}}{J_{off}} = \frac{1}{T_{max}^2}, \quad (2.9)$$

in agreement with the results obtained for the tunneling probabilities (2.5).

It should be noted that the conclusions about tunneling probability were based on solutions of the time-independent Schrödinger equation and hence describe a stationary situation. This, in turn, requires the carrier wave function at resonance (strongly) localised within the well (to a degree which decreases with increasing T_{max}), in other words T_{Gres} to be $\approx T_{min}/T_{max}$.

Such a requirement, from a physical point of view, means that the carriers must be predominantly localised (trapped) within the well or, equally, that QW must be “filled up” with carrier (up to the level described by the stationary wave function), before resonant tunneling is fully established.

The effect should be taken into account every time the states in the QW are not occupied at the starting point of an experiment. This is often the case, for example when the levels are higher than the Fermi level in the injector and collector. Under this condition, a transient width time constant τ_0 is required for the system to approach its final configuration. During such a transient time, the incoming (tunneling) particles essentially become trapped within the well where the probability density coefficient gradually increases.

Although τ_0 must depend on the initial condition, it is commonly accepted that it should be of the order of the resonant state lifetime, hence exponentially increases with the barrier phase area [HK86].

$$\tau_0 \approx \frac{\hbar}{\Delta E} \propto \frac{1}{T_{max}} \quad (2.10)$$

2.1.2 Coherent versus incoherent resonant tunneling process.

In fact, the tunneling mechanisms as they are discussed in the previous section 2.1.1 can be divided into two extreme interpretations [Lur89, Pri87, But88]: 1) The incoherent (classical) “sequential tunneling” description of resonant tunneling first into and then by a distinct process, out of, a localised QW state [Lur85]. 2) The coherent description of resonant tunneling as an electron wave phenomenon analogous to the resonant transmission of light through a Fabry-Perot etalon [RA84].

The inherent width ΔE of the resonance peak in the coherent tunneling transmission probability $T(E)$, compared with \hbar/τ_{scat} , gives us an estimate of the dominating process in the tunneling. Here τ_{scat} is the lifetime for lateral scattering of an electron in the two-dimensional subband associated with the resonant quasilevel and E is the energy associated to the perpendicular to the plane momentum of the electron.

If $(\Delta E/\hbar)\tau_{scat} \gg 1$, then one expects coherent resonant tunneling.

If $(\Delta E/\hbar)\tau_{scat} \ll 1$, sequential process should prevail.

It may be applied by taking $\tau_{scat} \approx \mu m^*/e$, where μ is the electron mobility for the “well” subband.

While the packet is momentarily “trapped” in the well, its wave function is essentially that of a state of the well subband, with the assigned value of the wavevector parallel to the heterostructure plane. Then if τ_{scat} is substantially less than this resting time the packet state will scatter within the well, to states outside the resonance range of E and with loss of coherence — hence the resonance character of the state will be destroyed. But if τ_{scat} is substantially greater than this resting time the scattering will not occur and the resonance will not be destroyed. We expect this resting time to be, essentially, the transient width time constant (2.10).

The foregoing discussion does not tell us what happens when $(\Delta E/\hbar)\tau_{scat} \simeq 1$. Obviously in that situation a more sophisticated analysis of the electrons’ encounter with the heterostructure is required.

In three-dimensional RTD, the negative differential resistance NDR arises solely as a conse-

quence of the dimensional confinement of states in a QW, and the conservation of energy and lateral momentum in tunneling. This statement being true for both the coherent and the sequential pictures. It should be noted that in the sequential picture the NDR is only associated with the first tunneling step and the device designer is free to describe it by a circuit element in series with an ordinary resistance, corresponding to the second tunneling barrier. In contrast, in the coherent picture the NDR is an overall property of the RTD system.

The total transmission probability for a carrier to traverse the sample is

$$T_{tot} = T_c + T_j$$

where T_c is the probability for a carrier to traverse the sample coherently and T_j is the transmission probability for carriers which have suffered an inelastic event. The coherent transmission probability cannot be calculated as if there were no inelastic events in the sample, since it is also affected by the presence of these processes.

In a completely coherent limit $T_j = 0$ the coherent transmission probability through two barriers in series exhibits resonances near the energies of quasi-eigenstates of the well,

$$T_c = T_{res} \frac{\frac{1}{4}\Gamma_e^2}{(E - E_r)^2 + \frac{1}{4}\Gamma_e^2}$$

with a peak value at resonance

$$T_{res} = \frac{4T_1T_2}{(T_1 + T_2)^2}$$

The peak value is 1 if the transmission probabilities of the two barriers are equal, and given by $T_{res} \simeq 4T_1/T_2$ in the case that $T_1 \ll T_2$, see Eq. (2.4). $\Gamma_e = \Gamma_1 + \Gamma_2$ is the total elastic width; Γ_1 and Γ_2 are the partial elastic widths of the resonant level. $1/\tau_e = \Gamma_e/\hbar$ is the decay rate of the resonant state. For a double barrier structure using WKB approximation

$$\Gamma_1 = \hbar\nu T_1, \quad \Gamma_2 = \hbar\nu T_2$$

Here ν is an attempt frequency, and in the case of a square well is given by $\nu = 2w/v$, where w is the width of the well and v is the velocity of a carrier in the well at the resonant energy E_r . At energies E away from E_r , transmission is still coherent but typically many orders of magnitude smaller than T_{res} , and, approximately,

$$T_c = T_{off} \propto \frac{1}{4} T_1 T_2$$

The equation was already used, see Eq. (2.2). The peak-to-valley ratio T_{res}/T_{off} is exponentially large if the transmission probabilities are exponentially small, see Eq. (2.5). Such huge peak-to-valley ratios have not been observed experimentally; inelastic scattering is one reason for this discrepancy. But there are also other reasons, e.g., the averaging over an energy range due to a three-dimensional incident distribution [Lur85], deviations from an ideal planar structure, and elastic scattering due to impurities [Pri87]

In the case of completely incoherent transmission, every carrier reaching the inelastic scatterer loses phase. In this limit a carrier cannot travel from one side of the resonant well to the other without being scattered inelastically. This process is a special limit of the sequential tunneling process. In general, the sequential tunneling process permits many oscillations in the well with frequency ν before the carrier loses phase memory. Total transmission probability in this limiting case is

$$T_j = \frac{T_1 T_2}{T_1 + T_2} = \left[\frac{1}{T_1} + \frac{1}{T_2} \right]^{-1}$$

Using $R = (\hbar/e^2)T_{tot}^{-1} = (\hbar/e^2)T_j^{-1}$ the equation yields the series addition of resistors, $R = R_1 + R_2$. If inelastic scattering is so strong that every carrier loses phase memory while traversing the well, the resistance of the structure contains no detailed information about the geometrical arrangements of the scatterers (separation of the barriers), but is the sum of the resistances due to the individual scatterers.

The crossover from coherent resonant to sequential transmission can be studied by applying the formula of Breit and Wigner [BW36, LL77]. The applicability of this formula to tunneling through disordered conductors in the presence of inelastic scattering is mentioned in by Azbel et al. [AHD84]. However, the results presented in the article are not compatible with the Breit and Wigner approach. Subsequently results which are compatible with the Breit and Wigner formula were obtained for a symmetrical double barrier by Stone and Lee [SL85]

The key point of Breit and Wigner is the notation that if there is elastic resonant transmission from channel 1 to channel 2

$$T_{21} = \frac{\Gamma_1 \Gamma_2}{(E - E_r)^2 + \frac{1}{4} \Gamma^2} \quad (2.11)$$

then the weakly coupled inelastic channels are also characterised by resonant transmission and couple to the elastic transmission with partial width Γ_3 and Γ_4 . Where Γ is the sum of all the

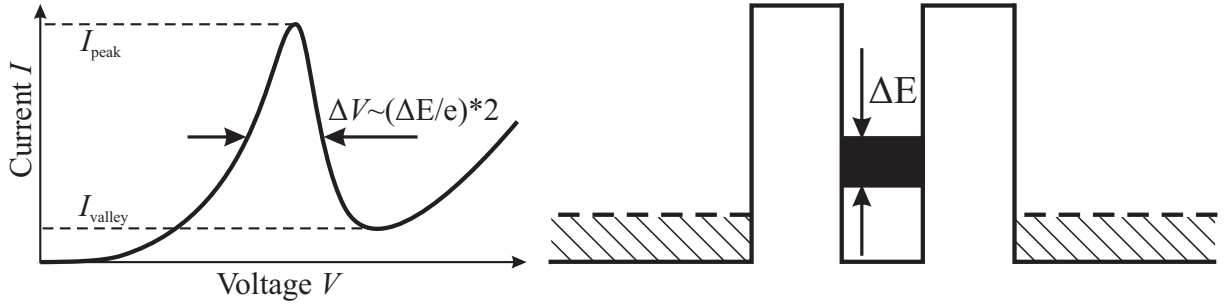


Figure 2.6: Illustration of broadening of the resonance peak (left) and the energy level in the QW (right).

partial rates and shown as ΔV in Fig. 2.6

$$\Gamma = \sum_{j=1}^{j=4} \Gamma_j = \Gamma_e + \Gamma_i \quad (2.12)$$

and $\Gamma_i = \Gamma_3 + \Gamma_4$ is the total inelastic width.

The total transmission probability is then

$$T_{\text{tot}} = T_{\text{res}} \frac{\frac{1}{4} \Gamma_e \Gamma}{(E - E_r)^2 + \frac{1}{4} \Gamma^2}$$

where $T_{\text{res}} = 4\Gamma_1\Gamma_2/\Gamma_2^2$. The peak value of the total transmission probability at resonance is $T_{\text{res}}\Gamma_e/\Gamma$. Thus the inclusion of inelastic or sequential events leads to a decrease of the peak value and broadens the resonance.

The resonance transmission probabilities for RTDs with resonant level at 100 meV and different scattering parameters are presented in Fig 2.7.

In the crossover region $\Gamma_e \simeq \Gamma_i$ we have not only a decrease of the peak value of the transmission with inelastic scattering, but also an increase of the off-resonance transmission probability.

$$T_{\text{tot.off}} \propto \frac{1}{4} \frac{\Gamma}{\Gamma_e} T_1 T_2$$

Using the same approach one can easily simplify the equation for the density of states in a

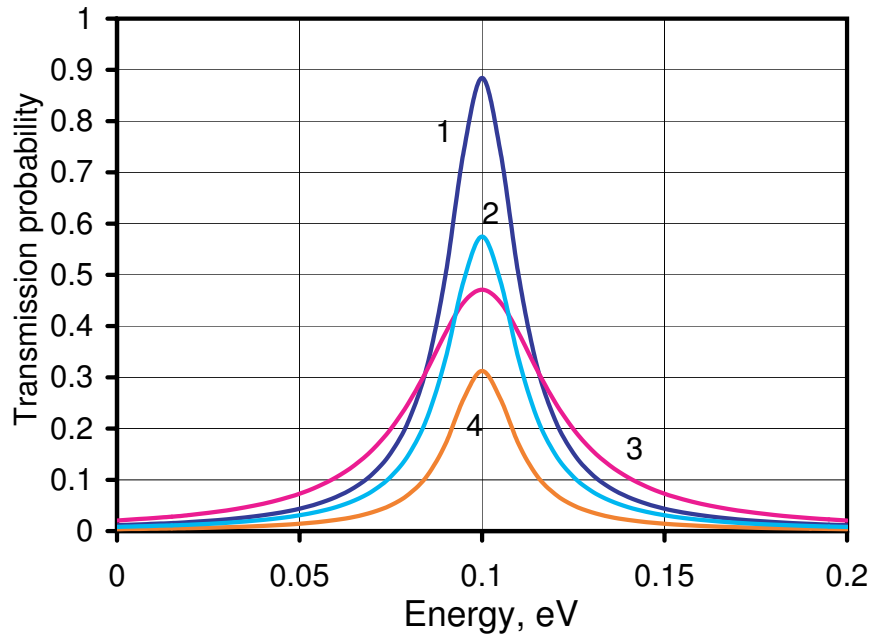


Figure 2.7: Transmission probability of an RTD calculated by Breit and Wigner formula. 1. Initial parameters. 2. Γ_2 is doubled. 3. Γ_i is doubled. 4. Γ_1 is halved.

quantum well to the next compact formula in the presence of inelastic scattering [IP96]

$$\rho_w(E) \approx \frac{1}{\pi} \frac{\Gamma}{(E - E_r)^2 + (\Gamma/2)^2} \quad (2.13)$$

This formula holds true if each partial width is much smaller than both the resonant energy E_r and the difference between the height of the barriers and E_r .

2.1.3 Elastic and inelastic scattering mechanisms, phonon replica.

In the elastic scattering process [WLP⁺88, FS89, FHS90] the total energy of the particle remains unchanged, but the wavevector is altered. The situation occurs, for example, in scattering by a dopant impurity ion, carrier-carrier scattering, plasmon scattering, alloy scattering, interface roughness and so on. Electron-electron, electron-hole and hole-hole scattering processes are important at high carrier concentrations. At high and intermediate concentrations, plasmon scattering (due to collective oscillations of the carrier gas) is of importance. Alloy scattering is important in ternary alloys, e.g. ZnMnSe, AlGaAs and others.

An inelastic scattering process [SL85, ZC92, BB98] is a scattering process where the electron suffers a fixed energy loss as well as a change of the wavevector. This is the case for electron scattering by lattice vibrations (phonons) where the electron loses energy and the lattice gains

it.

The elastic scattering mechanisms can be relatively easily studied in RTD structures in magnetic fields perpendicular to the plane of the QW [LAE⁺89]. If the width of resonant peak is smaller than distance between Landau levels, one would expect formation of peaks in the valley region. The peaks are associated with Landau levels [LL77] in the quantum well. The Landau levels energies are $E_n = \hbar\omega_c(n + \frac{1}{2})$ where $n = 0, 1, 2, 3, \dots$ the Landau level number and $\omega_c = \frac{eB}{m}$ is the cyclotron frequency. The role of the magnetic field perpendicular to the plane of the QW is to reduce in-plane movement of the electrons to defined (cyclotron) energies, in another words the in-plane k-vector will be quantized. Taking into account the definition of the elastic scattering process, this means that the scattering will be suppressed in the space between the Landau levels and enhanced at the energies equal to the energies of the levels. Obviously, by comparing the amplitude of the Landau oscillations in the valley current of the RTD one can gain information about the magnitude of the elastic scattering. The oscillations associated with Landau levels are not seen in the k-vector conserving resonant tunneling (with constant effective mass), because in this case inter-Landau level transitions are not allowed.

On the other hand, in the valley of the resonant tunneling peak one can often find a phonon replica [GTC87a]. The phonon-assisted tunneling is an inelastic scattering that leads to a phase coherence breaking [ZC92]. The physical picture of the inelastic electron-longitudinal(LO)-phonon scattering can be seen as follows. The electron tunneling from the emitting lead to the collecting one, which will spend some time in the QW and if the time is longer than the scattering time, an LO phonon will be emitted and the k-vector component, as well as the energy of the electron, will be changed. The electron will then tunnel sequentially. The change in energy is equal to the longitudinal phonon energy E_{LO} that is material specific and can be measured by optical means (e.g. Raman spectroscopy [ASDR88]).

Under a perpendicular magnetic field applied to the QW plane the phonon energy will not change. Although, separated by the distance E_n from the E_{LO} the Landau levels' peaks will be formed. So that at increased magnetic fields the Landau levels of the main resonance peak can cross the phonon replica peak. Under such conditions, in order to investigate elastic scattering, it is important that the main peak and the phonon replica are well separated.

The classical first resonant peak in the IV characteristic is shown in Fig 2.8. The main resonant peak is located at 105 mV and has a peak to valley ratio of 2.5 (the ratio is important because it quantifies the part of the resonant current compared to background current). The broader feature which can be seen at approximately 165 mV is an LO phonon replica.

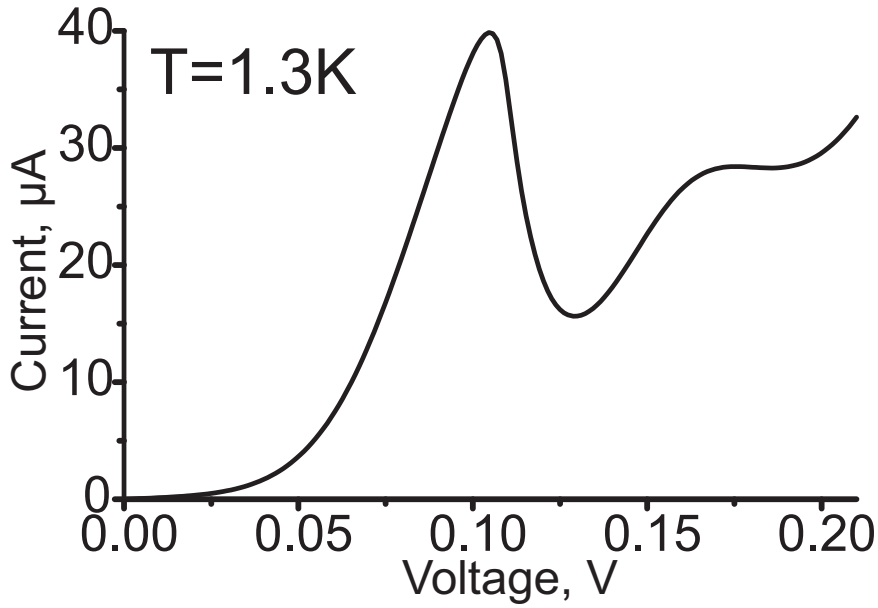


Figure 2.8: Typical I - V characteristic of an RTD at low temperature.

2.2 Magnetic field influence on RTDs.

2.2.1 Magnetic field perpendicular to the QW.

In the presence of a magnetic field perpendicular to the tunnel barriers in an RTD, the motion of the carriers in the well is no longer described by plane waves. The effect of the magnetic field on carriers is to force them to move in circular cyclotron orbits perpendicular to the field, quantizing an in-plane kinetic energy of the electron states into discrete Landau levels as it is depicted in Fig. 2.9 (left). The total energies of the electrons are given by

$$E = E_C + (n + \frac{1}{2})\hbar\omega_C \pm \frac{1}{2}g^*\mu_B B$$

where E_C is the confinement energy of the potential well and ω_C is the cyclotron frequency defined as $\frac{eB}{m_{\parallel}^*}$ where m_{\parallel}^* is the in-plane ($\perp B$) effective mass of the circularly moving charge.

The last term of the equation is a regular Zeeman splitting with a Lande-factor g^* and $\mu_B (= eh/2m_0)$ is the Bohr magneton. The cyclotron diameter is given by:

$$d_C = 2\sqrt{\frac{2(n + \frac{1}{2})\hbar}{eB}}$$

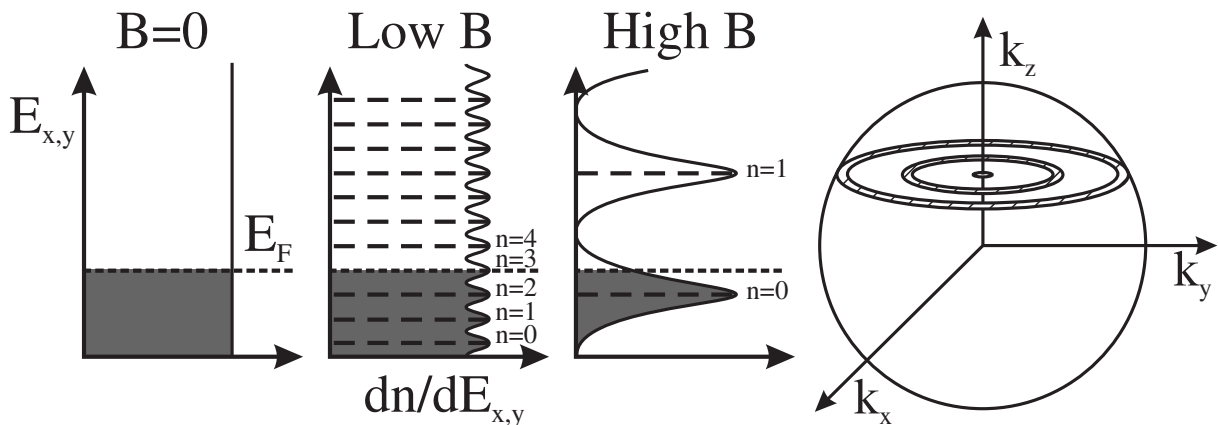


Figure 2.9: From left is a density of states in a 2D electron gas in a magnetic field for the cases of zero magnetic field, low magnetic field, and high magnetic field. From right is the S. Luryi's [Lur85] picture of sequential resonant tunneling in a perpendicular magnetic field. The shaded area of each diagram indicates states occupied by electrons. For simplicity, additional splitting due to the spin states is not taken into account in the diagrams. Note that the Fermi level (E_F) does not necessarily remain independent of field as shown here.

If the effective masses in the injector and in the QW are equal as it is shown in Fig. 2.9 (right) the k -vector conservation will prevent inter-Landau levels' transitions (oscillations in I-V curve). In other words, the electrons are tunneling through the structure preserving Landau number or its cyclotron orbit. But it is possible that on the positive differential slope of the resonance additional step-like features will appear in the perpendicular magnetic field as it is shown by Zaslavsky et al. and T. Gonçalves da Silva et al. [ZTSS89, dSM88]. The idea can be understood as an increasing current step when the next cyclotron orbit crosses the Fermi level in the injector, see Fig. 2.9 (right).

In the case that the electron effective masses in the injector and quantum well are not equal, one can expect to observe features in the I-V curve at constant magnetic field or equivalently oscillations in current when magnetic field is swept at constant voltage. Charge accumulation in the injector can significantly increase the effect [GTC87b]. The current-voltage characteristics of resonant tunneling structures are drastically influenced by the difference of electronic effective masses between the electrodes and the quantum well. In particular, if the mass in the well is larger than that in the emitter, the current peak is shifted to lower voltages, relative to the more conventional case of equal masses [OMW90]. The effect is seen on the Luryi's picture of resonant tunneling Fig 2.3 as the QW energy level plane in $k_x - k_y$ would be curved up or down in k_z depending on whether the effective mass in the emitter is bigger or smaller than the one in the QW.

With the k -vector not conserving "scattered" resonant tunneling, additional inter-Landau levels oscillations are seen in an I-V curve under a perpendicular magnetic field that makes it possible to study the elastic scattering process (see section 2.1.3).

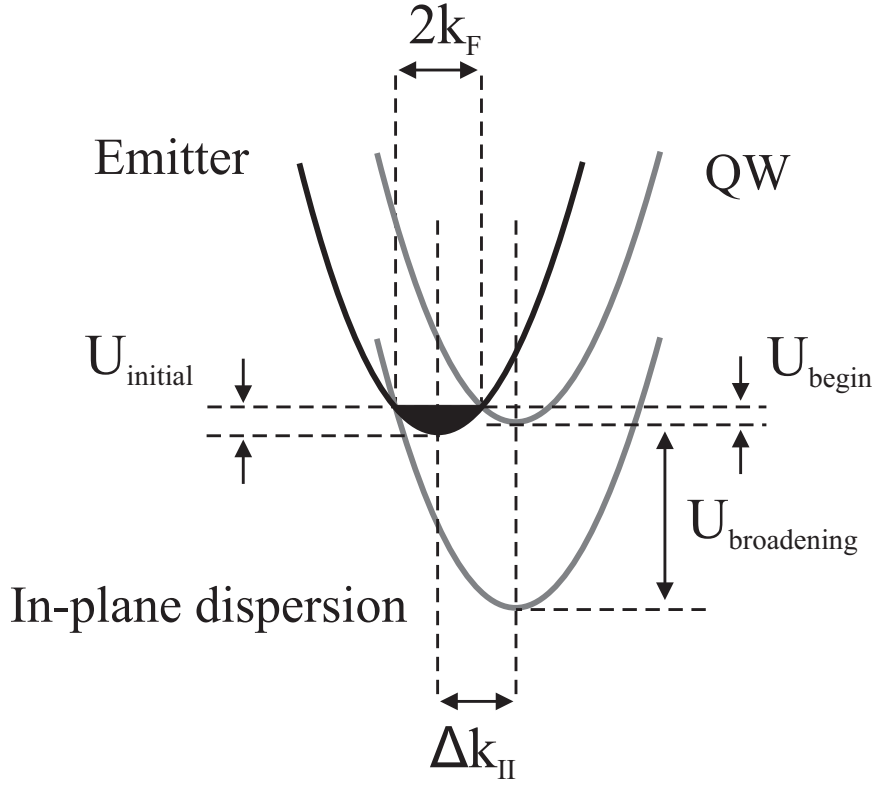


Figure 2.10: Schematics of the broadening of the resonance. The interaction of the in-plane dispersions of the emitter (black) and QW (grey) states represents the satisfaction of energy and momentum conservation conditions. Notice that the $U_{initial}$ is much smaller than the $U_{broadening}$.

2.2.2 Magnetic field in-plane of the QW.

Taking into account both energy and in-plane momentum conservation during tunneling into a QW, a resonant peak in the I-V characteristic (at zero magnetic field) starts when a level in the QW is aligned with Fermi energy in the injector. The resonant peak ends when this level passes the bottom of the conduction band in the injector (details in section 2.1.1). The effect of a magnetic field perpendicular to the electron tunneling direction is to shift an electron k-vector while tunneling (Lorentz force), so that it arrives in the quantum well with increased in-plane momentum. In this case, one needs to apply the energy conservation and “shifted” momentum conservation rule as depicted in Fig 2.10 and introduced by [ARM⁺90]. $U_{initial}$ is the Fermi level in the injector and consequently the width of the resonance from the onset to maximum, U_{begin} is a shift in the beginning of the resonance and $U_{broadening}$ is a new width of the resonance. Shift in the in-plane k-vector is

$$|\Delta k_{II}| = \frac{eB\Delta z}{\hbar}$$

As one can see $U_{broadening} > U_{initial}$ means that the resonance is broadened in a traversal

magnetic field. Moreover, the resonant is shifted to higher voltages (at the beginning of the resonance as well as at its maximum). The maximum of the resonant peak is not, in this case, the last energy at which the level in the QW overlaps with the levels in the injector (because the maximum overlap will occur before it).

Great experimental and theoretical attention was given to the problem of resonant tunneling under a transversal magnetic field. A quenching of the bistability in a bistable RTD with increased in-plane magnetic field, that was observed experimentally [ZLT⁺90], can be used to investigate NDR region without use of NOR (see 3.2.3). At even higher magnetic fields, the broadening dominates and the resonance is basically smeared out. Instead, formation of the magnetically induced oscillations is possible. These oscillations were explained in terms of the edge states bound to the first barrier [HPE⁺89] and related to Landau levels' quantization of the tunneling electrons. Theoretical investigation of coherent and sequential tunneling in double barriers with transverse magnetic fields [PBT89] show that in some cases one can distinguish the level of sequential tunneling from coherent with transverse magnetic field.

Very interesting experimental as well as theoretical investigation of RTD in a tilted magnetic field [GBGV91] evidently shows that in their RTD inter-Landau levels transitions are possible in tilted magnetic field. Coherent transport model accounts for this affect and allows an explanation of the appearance of several satellites of the resonant current peak. Magnetic field dependence is in good agreement with expected Landau levels spectra.

The big question about the in-plane magnetic field dependence of the phonon replica is not sufficiently addressed in literature. As it was shown in section 2.1.3, phonon-assisted tunneling is an inelastic scattering process which leads to the breaking of phase coherence. Inelastic scattering means that the electron suffers energy loss as well as a change of wavevector. The energy loss is fixed by LO phonon energy, but the k-vector is partially randomised, still it is limited to the allowed quantized values in the QW. Experimental observations of the transverse magnetic field dependence of the resonant peak and phonon replica [LKW⁺98] show quadratic shift in the magnetic field of the resonant peak maximum and magnetic field independent position of the phonon replica.

Chapter 3

Experiment.

3.1 Diluted magnetic semiconductors.

3.1.1 Giant Zeeman splitting.

Paramagnetic DMS in a magnetic field has a spin splitting of the levels in the conduction and valence band that is much larger than the value caused by the regular Zeeman term and is called “giant Zeeman splitting”.

The origin of the normal (regular) Zeeman effect is that in a magnetic field, the angular momentum quantum state can undergo a displacement from degeneracy, which can be understood classically, as Lorentz predicted. For example, the p-orbital has three possible angular momentum quantum states that are degenerate (of the same energy) under normal circumstances. However, each angular momentum quantum state has a magnetic dipole moment associated with it, so the effect of a magnetic field is to separate the three states into three different energy levels. One state increases in energy, one decreases in energy, and one remains at the same energy. Zeeman discovered the effect, but under closer investigation it did not concur with Lorentz. The electron spin had not been discovered at the time of Zeeman’s original experiments, so the cases where it contributed were considered anomalous. In fact, it was the anomalous Zeeman effect that led to the discovery of spin.

In general, both orbital and spin moments are involved, and the Zeeman interaction takes the form

$$\Delta E = \frac{e}{2m}(\vec{L} + 2\vec{S}) \cdot \vec{B} = g_L\mu_B m_j B \quad (3.1)$$

where g_L is the electron Landé g-factor and is one of the basic parameters in semiconductors that describes the magnitude of the Zeeman splitting of electronic states in magnetic fields. The g-factor in semiconductors differs from the free electron g factor in vacuum, $g=2.0023$, due to the spin-orbit interaction [RLZ59, BKR⁺03]. Depending on the semiconductor material, this interaction can change the effective g-factor by up to an order of magnitude and become positive as well as negative. $\mu_B = \frac{e\hbar}{2m_e} = 9.2740154 \times 10^{-24} \text{ J/T} = 5.788382 \times 10^{-5} \text{ eV/T}$ is a Bohr magneton. m_j is a z-component of the total angular momentum. B is a magnetic field.

In the DMS materials a strong exchange interaction exist between the localised d-electrons of magnetic ions and the band electrons. When a magnetic field is applied the net alignment of the ions spin leads to the free carriers giant Zeeman energy splitting. This splitting is usually much larger then the regular Zeeman one (Eq. 3.1) due to the direct action of magnetic field on electron spin. In the case of giant Zeeman conduction band spin levels splitting ΔE of the DMS as a function of magnetic field B is given by a modified Brillouin function [GPF79]:

$$\Delta E = N_0 \alpha x s_0 B_s (s g \mu_B B / k_B (T + T_{eff})) \quad (3.2)$$

where $N_0 \alpha$ is the s-d exchange integral, x , s , and g are the manganese concentration, manganese spin, and g-factor respectively, and μ_B is the Bohr magneton. B_s is the Brillouin function of spin s . s_0 and T_{eff} are, respectively, the effective manganese spin and the effective temperature. These phenomenological parameters are needed to account for antiferromagnetic $Mn^{++} - Mn^{++}$ exchange interactions [TvODP84, Fur88]. Functional dependencies of these parameters on composition based on the data for $Zn_{1-x}Mn_xSe$ epilayers given by $S_{eff} = -0.804 + 0.364/(x - 0.109)$ and $T_{eff} = 47.2x - 281x^2 + 714x^3$ [KYK⁺02].

Obviously, giant Zeeman splitting in low magnetic fields is stronger at lower temperatures. The explanation for this is that the material is in a paramagnetic state and the effect is a collective influence of oriented Mn^{++} atoms. Increased temperature disorients the manganese system and in this way decreases the effect of the magnetic field. Therefore in order to reach the same giant Zeeman splitting one has to apply higher magnetic fields. Simultaneously, decreasing temperature below T_{eff} does not make a great difference to the value of the splitting. The constant T_{eff} term will dominate and the decreased temperature will not increase the value of giant Zeeman splitting in a constant magnetic field. This effect can be qualitatively understood as an interaction between manganese atoms which dominates small temperature disorder at low temperatures.

The most pronounced influence of giant Zeeman splitting on properties of materials in magnetic field were observed in [Cd,Mn]Se, [Cd,Mn]Te, [Zn,Mn]Se, [Zn,Mn]Te [Sha86, SO87]. Where the effect of the density of states near Fermi energy produced large, but complicated magnetoresistance. Magnetic field induced change in the properties of the compound semiconductors could be colossal if the carrier concentration was near to metal-insulator transition.

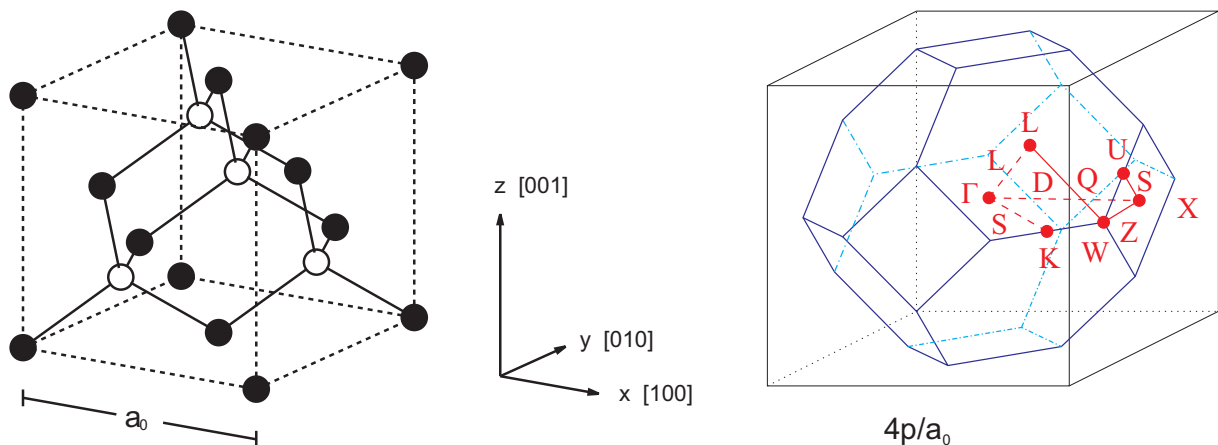


Figure 3.1: Zinc Blende crystal structure (left) with the first Brillouin zone for a fcc-Bravais lattice (right).

3.1.2 [Zn,Be,Mn]Se DMS.

The term ‘‘Diluted Magnetic Semiconductors’’ (DMS) was coined around 1980 [Gal79, PPV⁺82] and represents alloys of semiconductors and magnetic ions (transition metals or rare earths) which exhibit a variety of cooperative effects via spin exchange interactions [FK86]. The exchange interaction between the conduction carriers and the localised moments of the magnetic ions can drastically alter the transport, optical, and magnetic properties of the host semiconductor. In general, DMS are based on II-VI and III-V semiconductors.

One of the most promising magnetic ions is manganese (Mn). The manganese Mn^{2+} has a half-filled d-shell that gives spin (5/2) per Mn atom. It does not produce carriers which are incorporated in II-VI semiconductors (isovalent) that allow control of the carriers type and concentration independent of the Mn concentration.

Incorporation of the Mn ions in majority semiconductors is complicated by the fact that the manganese tends to segregate into separate phase, because of the fact that advanced growth methods are required in order to receive good material quality.

ZnSe is a well-known semiconducting material with band gap of 2.8 eV. Optical properties attract most attention in this wide band gap semiconductor. On the other hand, the material is known to have interesting electrical properties. It can be successfully doped by both n and p-type dopands, this is important for investigation of the fundamental transport properties of semiconducting structures. A crystal structure along with first Brillouin zone of ZnSe crystal lattice is shown in Fig. 3.1. The lattice structure of the ZnSe crystal is a zinc-blende face-centred cubic (fcc) Bravais lattice. The high-symmetry lines are indicated in the figure in red colour.

Semiconductor alloy [Zn,Be]Se is very interesting from optical as well as transport and device engineering points of view. Beryllium incorporated in the ZnSe semiconductor replaces zinc

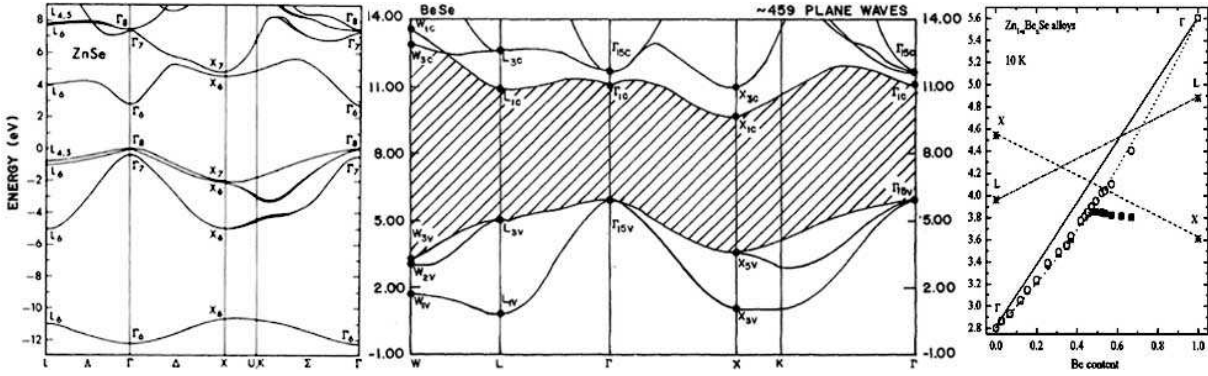


Figure 3.2: Energy-band structure of ZnSe and BeSe along with band gap evolution in $Zn_{1-x}Be_xSe$ with Be content (from left to right after [CC76, Stu70, CTF00] accordingly).

and thus have little influence on the electronic structure of the material. Growth of the alloy is non-trivial and the advanced growth technique as molecular beam epitaxy (MBE) is used to produce good quality of ternary alloy. Taking into account the Vegard's law for composition dependence of the lattice constant (approximately linear) and the fact that for ZnSe lattice constant is of 5.6676 \AA and for BeSe it is 5.139 \AA that means that the [Zn,Be]Se-ternary alloy can be grown lattice matched to GaAs substrates with only 3% Be content. The simplified approximation for the lattice constants [Zn,Be]Se is

$$\alpha_0(Zn_{1-x}Be_xSe) = -0.52x + 5.66$$

where x is the Be content $0 \leq x \leq 1$.

Another important influence of Be on ZnSe crystal is to change the band gap. The picture is illustrated in Fig. 3.2. As one can see the ZnSe crystal has direct $\Gamma - \Gamma$ and BeSe has indirect $\Gamma - X$ band gap. Detailed evolution of the band gap with Be content is shown in the last right inset of the figure. It can be seen that the composition dependence of the band gap is not linear but rather has a bowing parameter. As it is shown in the [CTF00] the best fit for the low-temperature, direct band gap of $Zn_{1-x}Be_xSe$ alloys is

$$E_g^\Gamma(x) = 2.8(1 - x) + 5.6x - 0.97x(1 - x)$$

where x is the Be content and the bowing parameter is $b = 0.97 \text{ eV}$.

In addition to the band gap change the band offset is changed with Be incorporation. Band offset for the conduction band is shown to be $\sim 60\%$ of the band gap change [KKL⁺00]. This makes possible to design fairly complicated structures in a very flexible way. For example, the tunneling or resonant tunneling structure can be grown with parameters very close to well known [Al,Ga]As structures. One of the major advantages of this structure as compared with a

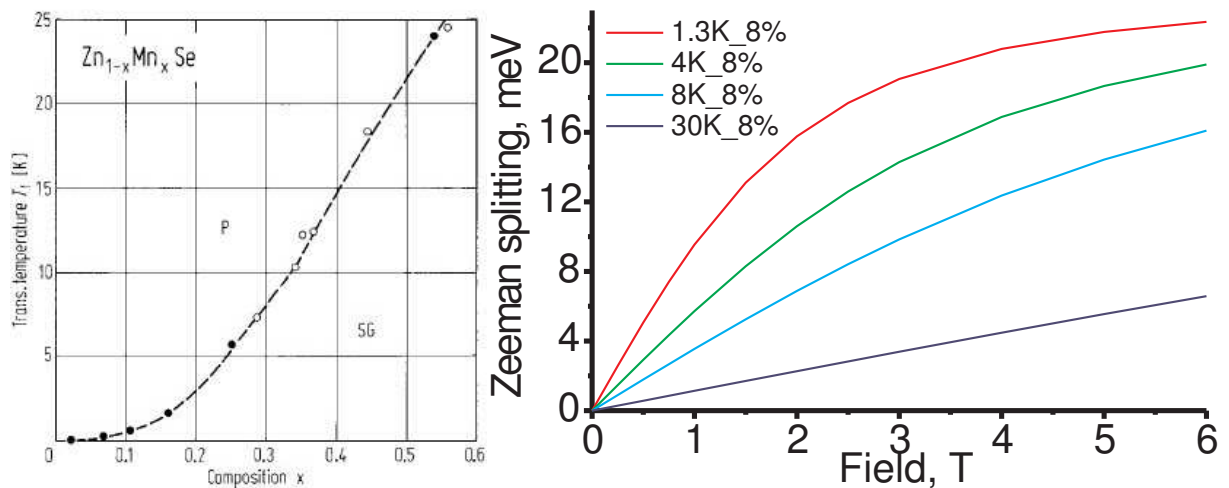


Figure 3.3: Left - magnetic phase diagram of $Zn_{1-x}Mn_xSe$ ternary DMS (after [LB87]). Right - temperature dependence of the magnetic field induced conduction band giant Zeeman splitting for the DMS with 8% Mn.

known one is that the indirect transition is much higher in energy.

The diluted magnetic semiconductor [Zn,Mn]Se is intensively used for investigation of fundamental properties of semiconductors. It is II-VI binary compound in which a magnetic ion (M^{++}) is substitutionally incorporated into the host crystal in the place of group-II element (Zn). Solid solution of $Zn_{1-x}Mn_xSe$ crystallise in the zinc-blende structure at $x \leq 0.30$ and in wurtzite at $0.33 \leq x$. A reasonably good quality of the material can be grown by MBE with manganese concentration up to 55 %.

The band gap of the ternary compound has highly nonlinear composition dependence. So, that at low Mn content the band gap is decreased, but after that it is bowed up and at low temperatures it comes back to its initial value at around 4 %. At higher contents the band gap is basically linearly increased [BBK⁺86]. Additionally, the return point when the band gap is equal to the initial one strongly depends on temperature. The return point happens at higher Mn concentrations for higher temperatures.

Magnetic phase of the DMS is shown in Fig. 3.3 (left). At higher Mn concentrations the magnetic phase is changed from paramagnetic to spin glass (see [LB87]).

The most exciting property of this material is the giant Zeeman splitting that in a mediate magnetic field and at low temperatures is as great as 100 meV. 20 % of the total splitting corresponds to splitting of the conduction band. As it is explained in the previous section 3.1.1 the splitting has nonlinear magnetic field dependence and saturates at high fields. The temperature dependence of the magnetic field induced giant Zeeman conduction band splitting for the $Zn_{0.92}Mn_{0.08}Se$ DMS is shown in Fig. 3.3.

Such a large splitting of the conduction band in magnetic field is shown to give an extremely

high electron polarization $\sim 100\%$ even at low fields [FKR⁺99]. In the same way as Y. Shapira used density of states in CdMnSe conduction band to explain magnetoresistance data [Sha86] one could use the idea to explain the electron spin polarization. So, with an increased magnetic field the density of states for different spin species of electrons will be split in energy. It is possible (in the case DOS has irregular shape) that the states for one spin specie will be out of the Fermi level range and the only allowed states for electrons will be spin-polarized.

The quaternary compound [Zn,Be,Mn]Se is a novel material system. It can be used to investigate basic properties of semiconductors, electrical devices and spin transport. This tuneable compound material is ideal for quantum devices design. In particular, in this system the band gap, magnetic properties, as well as carriers concentration can be tuned independently. Incorporation of [Be,Mn] in ZnSe does not introduce carriers and the material can be grown with sufficient quality using MBE.

3.2 Setup and sample design.

3.2.1 Measurement setup and technique.

I-V characteristics were measured on RTD structures in order to detect the effect of resonant tunneling. The measurements were done in a wide range of temperatures using low temperature cryostats depending on the temperature range desired. The majority of measurements were performed in a ^4He bath cryostat equipped with a needle valve between the main ^4He bath and a sample space. A standard 8 T superconducting magnet is used to apply magnetic field to the sample. A ^3He measurement cryostat equipped with 10 T superconducting magnet is used to reach temperatures in the range below 1 K and down to ~ 300 mK. A $^3\text{He} / ^4\text{He}$ Dilution Refrigerator with 16 T magnet is used to measure samples at temperatures below 300 mK.

The samples are bonded (normally with an ultrasonic needle and a gold wire) to chip carrier contact pads. The 18 pins chip carrier is placed on a sample stick and inserted in the cryostat. Electrical contacts to the chip carrier are ensured by gold covered springs supporting highly conductive needles. Resistance of the wires going down a cryostat is normally of the order of 3 - 5 ohms.

In order to prevent the measurement circuit from going into oscillations (see section 3.2.3) a voltage stabilised power supply is connected to the sample in parallel with low impedance parallel resistance [LAE⁺89] as in Fig 3.4. Current flowing through the device is calculated from a voltage drop measured over the low impedance reference resistance. Ideally (to improve voltage stabilisation) one does not use R_{serial} and keeps $R_{\text{reference}}$ and R_{parallel} as small as possible. Although, as we already know, these precautions are not always sufficient to remove bistabilities, in our case, use of NOR is extremely difficult. At the same time, first resonances could be easily stabilised with parallel resistor.

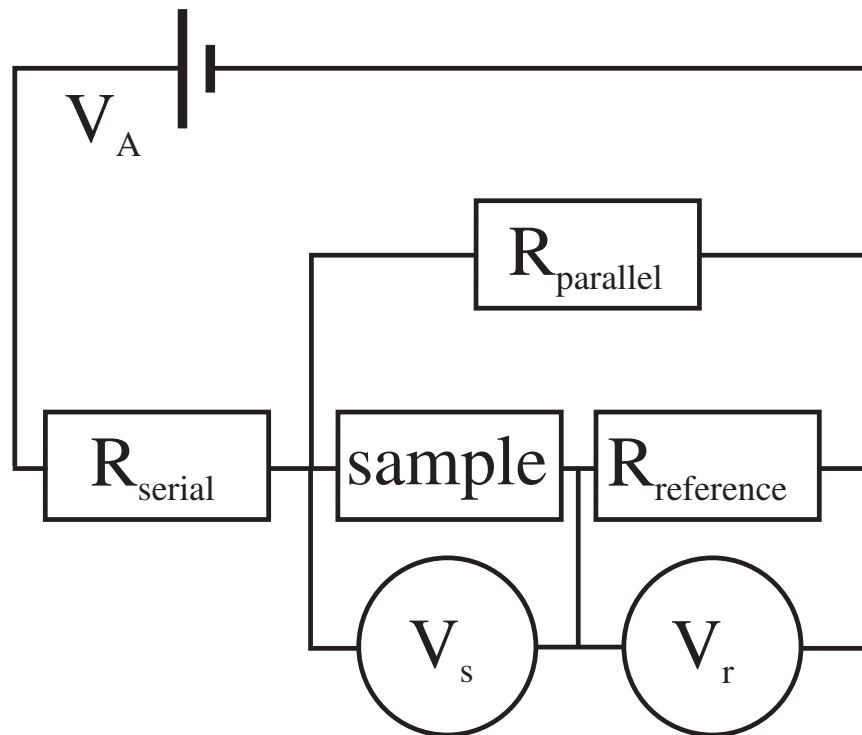


Figure 3.4: Circuit diagram for the measurement setup with a voltage divider $R_{\text{serial}} - R_{\text{parallel}}$

3.2.2 Charges in a RTD.

The charge distribution through an RTD structure has two characteristic features that play an important role in the functionality of the device. The first one is the principle of resonant tunneling based on charge accumulation in the QW. The accumulation is characterised by specific resonant state lifetime (2.10), broadening of the level (2.12) and the density of states (2.13).

Another, important charge accumulation region is placed in the injector of the device and attracts wide attention [WCL⁺90, KJP⁺90, WLC⁺91, Pri92, HGPB95]. A simplified picture of an RTD with the accumulation region is shown in Fig. 3.5(a). As one can see, quantization of the states in the injector accumulation region is possible and in many cases the effect was used to improve peak to value ratio. The basic idea behind it, is that the number of the resonant electrons at the peak voltage will be increased by the presence of a quantized level. For the mechanism of the resonant tunneling one can expect a diode current due to scattering into the resonance-associated levels from the cathode side and out of them to the anode side, for corresponding range of the external bias.

One of the successful approaches is the use of an emitter spacer layer as it is shown in Fig. 3.5(b) where the biased spacer layer is depicted in the inset. The influence of the spacer layer on peak to value ratio was shown experimentally by C. R. Wie and Y. W. Choi [WC91] and studied theoretically by the authors [CW92]. From these studies, it has been shown that the deeper the injector spacer layer, the better the peak to value ratio. Obviously one has to take into account

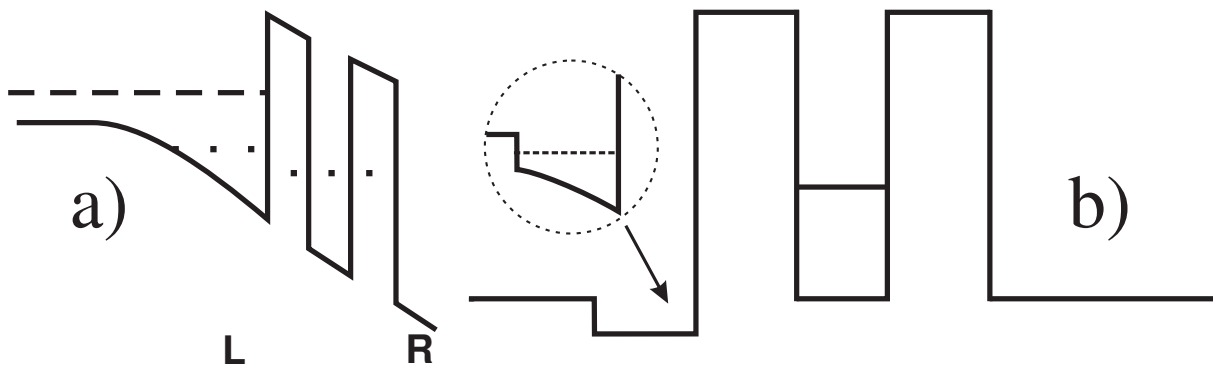


Figure 3.5: *The charge accumulation in RTD structures.*

the possible formation of two-dimensional electron gas in the injector, which will drastically influence the magnetic field dependence of the device. Furthermore, the investigations done by C. R. Wie and Y. W. Choi were done with the layer depth within a first quasi-bound state in the accumulation layer. With even deeper spacer layer, additional singularities in I-V characteristic (associated with higher quasi-bound states in the accumulation layer) can be seen.

Sequentially, presence of spacer layers in RTD was studied by using capacitance-voltage (C-V) measurements [WS94]. It is shown that the longer cathode spacer layer can result in a higher peak in the C-V characteristic, while the anode space layer has a relatively small effect on the peak and cut-off frequency.

3.2.3 Multistabilities in resonant tunneling structures.

A distinguishing feature of the I-V characteristic of an RTD is a negative differential resistance NDR on the upper voltage slope of the resonant peak. Because of the presence of NDR the device in series with a resistance can go to oscillations between two or more steady states “bistability” [GTC87a] and produce high (terahertz) frequencies [SKW⁺94].

One has to distinguish the two major origins of the oscillations. The first comes from the resistance that is in series with the RTD and is within the measured voltage. Then the measured voltage will be the voltage drop on the device plus the voltage drop on the series resistance. Basically, the real I-V characteristic of the RTD will be shifted in bias by the voltage drop across the series resistance. And, because the shift is proportional to the current, it is possible that the NDR region will not be reachable for standard constant voltage measurement setups. The situation is illustrated in Fig. 3.7(a) as compared to the original I-V curve shown in Fig. 2.8. One can see that even in the case of an ideal measurement setup in the NDR region there are few steady states with different currents. In this case the system will be oscillating between the states (A and B at applied V_A) and within short voltage range and will go from one state to another. The dashed area of the real I-V characteristic of the device will not be seen in the experiment. It is possible to investigate such kinds of transition and see some part of the hidden

I-V. For this one can sweep bias up and down and the “step” will happen at different voltages that will show a part of the I-V. In Fig. 3.7(a,b) the sweep directions are indicated by the arrows.

Another origin for such kind of bistability, which is also called as tristability [MLSE94] (because there is an additional “hidden” steady state at the same voltages) could be an internal property of the device, known as an internal (bi, tri) multistability [GTC87a]. The internal multistabilities are explained in terms of an electrostatic feedback due to charge build-up “charge accumulation” in the QW [LFM⁺96]. The idea is that the accumulated space-charge will modify the electric field in the collector barrier. Taking into account the fact that the QW density of states defining the charge accumulation is proportional to the broadening of the levels and the state lifetime (see Eqs. (2.13) (2.12) (2.10)) that in the last case $\tau \approx \frac{\hbar}{T_{max}E_0}$ where E_0 is a energy of the first level, the effect is bigger for wider barriers. In other words, the way to understand the intrinsic multistabilities is to treat the second (collector) barrier as a series resistance in the device that can bring the device to a multistable stage and is a necessary “intrinsic” device part (sequential tunneling picture). This simplified picture gives a good estimate for the origin of the intrinsic multistabilities which make it easy to explain the increased influence of the effect in the asymmetrical structures.

In a real experimental environment the multistabilities can be caused by using a non-optimal measurements setup. If the series resistance is not taken into account, there are two cases. One where the series resistance is within the measured voltage. Then the influence of the resistance is the same as internal multistabilities depicted in Fig. 3.7(a). And, the second case where the series resistance is outside measured voltage. The load line method can then be used to determine the slope of the “step” in I-V as it is shown in Fig. 3.7(b). Assuming there is a perfectly vertical load line (within value of the series resistance) the only difference in voltage at different currents will be caused by a series resistance. Taking this into account one can estimate a value of the series resistance in the measurement setup. For example for the measurement shown in Fig. 3.7(c) the estimated series resistance (difference in voltage divided by difference in current during the multistability step) is 82 Ohm.

The NDR region can be investigated using a voltage supply designed to have a load line with positive slope as it is shown in Fig. 3.6 [LMS⁺94], equivalent to a voltage source and negative series resistance. This enables the portion of the I-V characteristic inside the region of apparent bistability to be examined. Such a device is an active circuit designed to have a negative output resistance (NOR) [MLSE94] that compensate for the presence of the series resistance.

In the multistability regime the measurement setup goes into oscillations and, depending on the capacitance and conductance of the measurement setup and RTD, the frequency will vary. In the standard DC measurement setup the oscillations will be averaged and the resulting shape of the NDR region can have a complicated form as is seen in Fig. 3.7(d). Because of the high frequencies produced by the device (up to several terahertz) use of the NOR in the RTD devices is a complicated task and requires good technical and structural optimization.

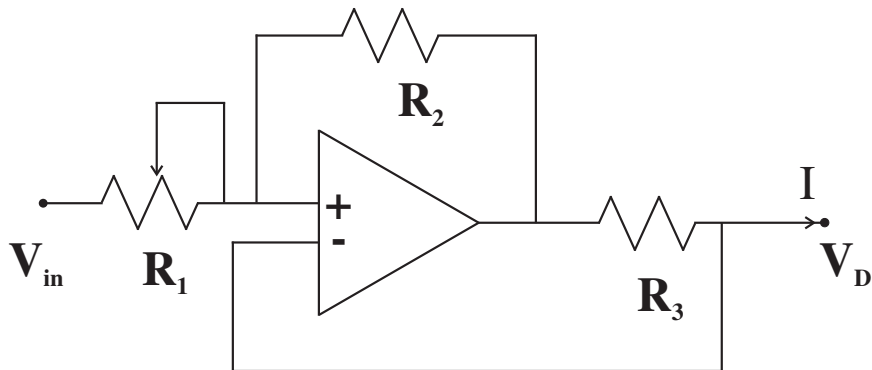


Figure 3.6: Circuit diagram for a NOR voltage supply. The output voltage is given by $V_D = V_{in} + (R_1 \cdot R_3 / R_2)$

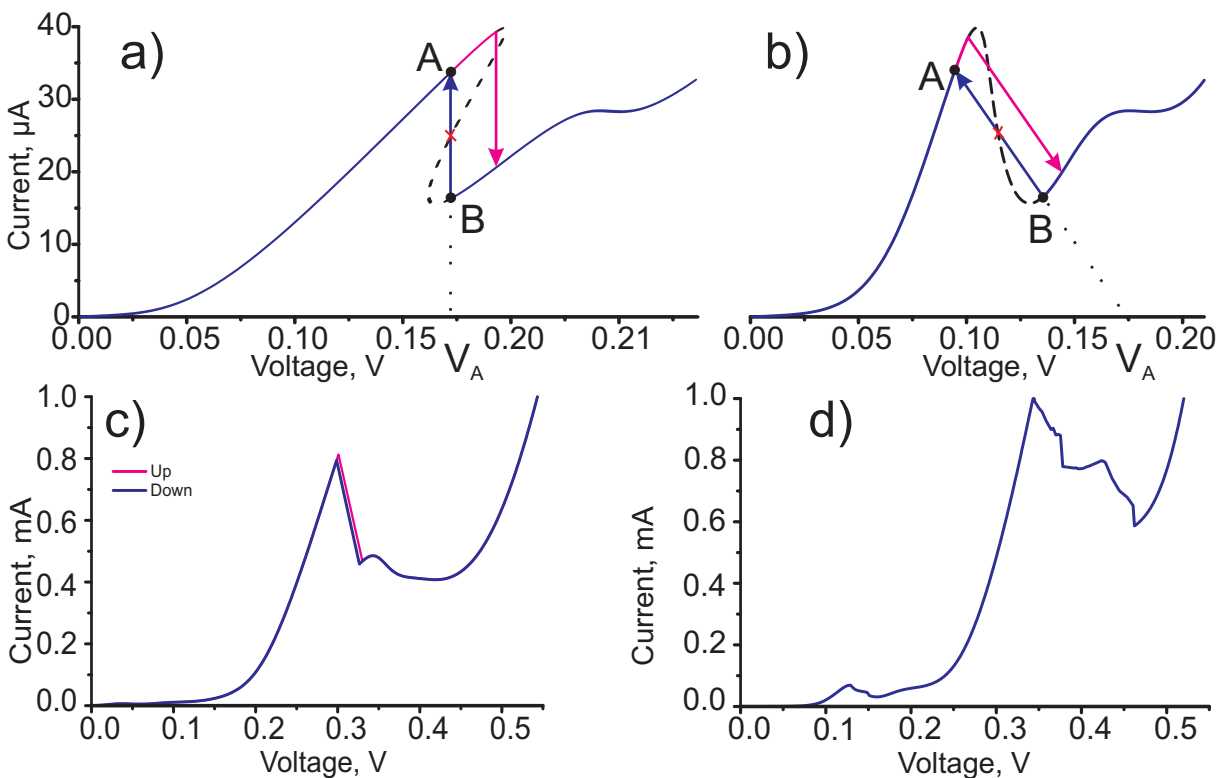


Figure 3.7: I-V characteristic of an RTD with series resistance at multistabilities.

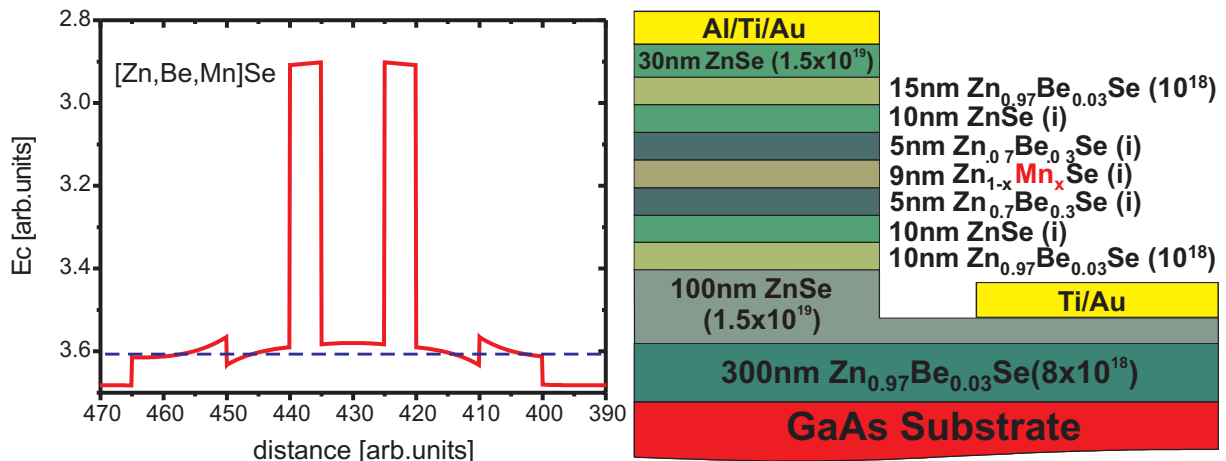


Figure 3.8: Left - conduction band profile of the double barriers quantum well structure with injector and collector regions. Right - layer structure of the device grown by MBE on GaAs substrate.

3.2.4 Sample design.

The versatility of the [Zn,Be,Mn]Se material is used to investigate properties of magnetic semiconductor structures. All-II-VI RTD structures from the material are grown by MBE.

One of the biggest concerns while designing the structure for MBE growth is the strain. That means that the lattice constant should not have rapid variation within the structure. Or, if this is the case, the strained layer should be sufficiently thin. This makes the design of the structures somewhat limited.

In Fig. 3.8 (left) the conduction band profile of the RTD is depicted. The dashed line in the figure represents the Fermi level. The undoped [Zn,Mn]Se DMS quantum well is sandwiched between $Zn_{0.7}Be_{0.3}Se$ tunnel barriers. The injector and collector regions consist of undoped ZnSe separated from highly n-type doped ZnSe by low n-type doped [Zn,Be]Se with 3% Be. The idea behind the injector and collector step-like structure is to improve peak to value ratio as is discussed in the section 3.2.2.

The indirect ($\Gamma - X$ or $\Gamma - L$) transitions in [Zn,Be]Se barriers are almost 1 eV higher than the direct ($\Gamma - \Gamma$) transition (with 30% Be) as it is shown in Fig. 3.2. The electron effective mass in the compound is the same as in the ZnSe semiconductor [Stu70] which avoids observation of inter Landau levels mixing [ZTSS89, dSM88].

In Fig. 3.8 (right) the layer structure of the RTD is presented. The bottom (red) layer is a GaAs substrate. After degassing the substrate, 300 nm of lattice matched $Zn_{0.97}Be_{0.03}Se$ buffer is grown by MBE. The buffer is doped until $n = 8 \times 10^{18} \text{ cm}^{-3}$. 100 nm of highly doped ($n = 1.5 \times 10^{19} \text{ cm}^{-3}$) ZnSe is grown over the buffer as a back side contacting layer. The collector region is formed by 10 nm of $n = 1 \times 10^{18} \text{ cm}^{-3}$ doped $Zn_{0.97}Be_{0.03}Se$ and 10 nm

of intrinsic ZnSe. 5 nm thick $Zn_{0.7}Be_{0.3}Se$ barriers are placed around 9 nm of intrinsic $ZnSe$ QW. The injector region consists of 10 nm of intrinsic $ZnSe$ and 15 nm of $Zn_{0.97}Be_{0.03}Se$ with $n = 1 * 10^{18} \text{ cm}^{-3}$ doping. 30 nm of highly $n = 1.5 * 10^{19} \text{ cm}^{-3}$ doped ZnSe top contact layer finalise MBE growth.

The top contacts are normally done by the deposition of a metal contact layer consisting of 10 nm Al to achieve good contact, 10 nm Ti as a diffusion barrier, and 30 nm Au to avoid oxidation. To increase the quality of the contacts the samples are transferred from MBE to the electron beam evaporation machine under ultra high vacuum conditions. This procedure reliably yields low contact resistivities of the order of 10^{-3} cm^2 . Heterostructures are patterned into square mesas with sides of 100, 120, and 150 μm by optical lithography with positive photoresist followed by metal evaporation and lift-off. Since the bottom contact can only be fabricated after processing, it must rely on an *ex situ* technique where the contact resistivity is typically 1–3 orders of magnitude higher. Its resistance is kept reasonably low by a combination of the incorporation of a highly n doped 100 nm ZnSe contact layer in the heterostructure, and the use of a relatively large ($500^2 \mu m^2$) Ti-Au contact pad.

Chapter 4

Spin selection in RTDs with magnetic QW.

4.1 Introduction.

The physics governing spin injection and detection in semiconductor structures is now well understood [SFM⁺00, Ras00, FJ01]. The problems associated with the impedance mismatch between a magnetic layer and the semiconductor can be overcome, e.g. by using dilute magnetic semiconductor injectors [FKR⁺99, OYB⁺99, SRG⁺01], or by fitting metallic magnetic contacts with tunnel barriers [MdBD⁺02]. However, these options can only be utilised to transfer majority spin from the magnetic material into the non-magnetic layer and, similar to the situation in magnetic metallic multilayers, contacts with different shape anisotropy must be used when the direction of the spin of the electrons in the semiconductor is to be detected. Rather than having to use an external magnetic field to switch the contact magnetisation, it would be very desirable to have devices where the spin character of the injected or detected electrons could be voltage selected. Here we report on the successful operation of a magnetic resonant tunnelling diode (RTD), which we hope will prove useful for voltage controlled spin-polarized injection and detection [DiV99].

The idea behind the RTD scheme is fairly straightforward but its realisation was previously hampered by material issues [GKF⁺01]. Since the well is made of a magnetic material, the energy levels in the well will split into spin-up and spin-down states, as sketched in Fig. 4.1(b). By selectively bringing the spin-up or spin-down state into resonance, one can dramatically increase the transmission probability of the desired spin species.

In this chapter, we describe our experimental investigations of an all-II-VI semiconductor RTD based on ZnBeSe, and with a ZnMnSe dilute magnetic semiconductor (DMS) quantum well. In the presence of a (constant) magnetic field, the DMS exhibits a giant Zeeman splitting that, at low temperatures, leads to an energy splitting of the Zeeman levels in the conduction band of about 15 meV at fields of one to two Tesla. Our samples show typical RTD-like current-voltage (I-V) characteristics with peak to valley ratios of over 2.5 to one. As a function of applied

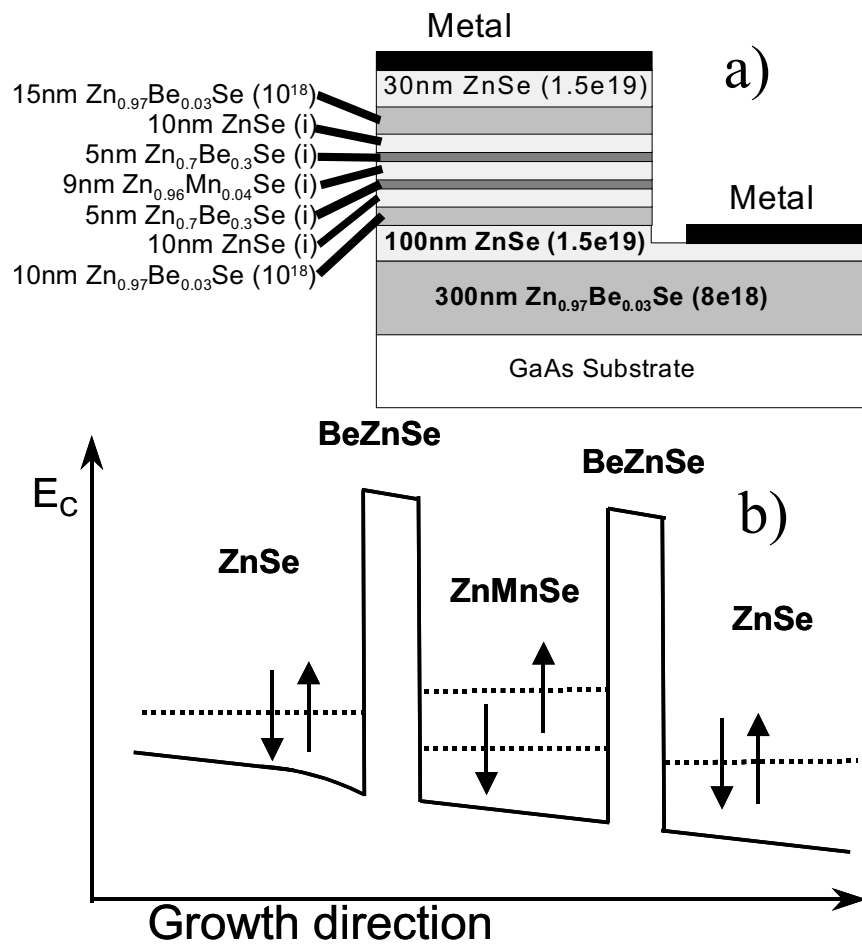


Figure 4.1: a) Layer structure of the device and b) schematic view of resonance tunnel diode band structure under bias.

magnetic field, the transmission resonance of the I-V curve splits into two peaks with a splitting corresponding to the separation of the energy levels in the well.

4.2 Details of the experiment.

The investigated II-VI semiconductor heterostructures were grown by molecular-beam epitaxy on insulating GaAs substrates. The active region of the device consists of a 9 nm thick undoped $\text{Zn}_{0.96}\text{Mn}_{0.04}\text{Se}$ quantum well, sandwiched between two 5 nm thick undoped $\text{Zn}_{0.97}\text{Be}_{0.03}\text{Se}$ barriers. The complete layer structure is shown in Fig. 4.1 along with a schematic of the potential energy profile of the double-barrier structure under bias. The bottom 300 nm of $\text{Zn}_{0.97}\text{Be}_{0.03}\text{Se}$, highly n-type doped with iodine to a concentration of $n=8 \times 10^{18} \text{ cm}^{-3}$, as well as the 15 and 10 nm thick $\text{Zn}_{0.97}\text{Be}_{0.03}\text{Se}$ layers with $n=1 \times 10^{18} \text{ cm}^{-3}$ in the injector and collector contain 3% Be in order to be lattice matched to the GaAs substrate. The barrier layers are clearly not lattice matched to the substrate, but are sufficiently thin to be grown as fully strained epitaxial layers. The heterostructure was patterned into square mesas with side of 100, 120 and 150 μm by optical lithography with positive photoresist followed by metal evaporation and lift off.

Special care must be taken in order to obtain good ohmic contact to the II-VI semiconductor. For the top contact, this can be achieved by in-situ growth of a metal contact layer consisting of 10 nm Al to achieve good contact, 10 nm Ti as a diffusion barrier, and 30 nm Au to avoid oxidation. This procedure reliably yields contact resistivities of the order of $10^{-3} \Omega \cdot \text{cm}^2$. Since the bottom contact can only be fabricated after processing, it must rely on an ex-situ technique where the contact resistivity is typically 1-3 orders of magnitude higher. Its resistance is kept reasonably low by a combination of the incorporation of a highly n doped 100 nm ZnSe contact layer in the heterostructure, and the use of a relatively large ($500^2 \mu\text{m}^2$) Ti-Au contact pad.

The samples were inserted into a ^4He bath cryostat equipped with a 6 T superconducting magnet, and were investigated using standard low noise electrical characterization techniques. Precautions were taken to prevent problems associated with the measurement circuit going into oscillations. A stabilised voltage source was used to apply bias to the circuit, which consists of the RTD, a 33 Ohm reference resistance in series and a 40 Ohm resistor in parallel. Such a setup is known to prevent bi-stability of the circuit in the region of negative differential resistance [LAE⁺89]. By measuring the voltage drop over the RTD and the reference resistor as the bias voltage is swept, I-V curves of the RTD can be extracted. The absence of charging in the device was confirmed by comparing I-V curves with a different sweep direction [MLSE94].

We studied devices with Mn concentrations of 4% and 8% in the quantum well layer. The layers' thicknesses of the 4% sample are given in Fig. 4.1, whereas those for the 8% Mn sample are all 6% thinner. For structures with 4% Mn in the well, the first resonance for positive bias occurs at 105 mV and has a peak to valley ratio of 2.5 whereas for the 8% Mn sample the resonance is at 127 mV with a peak to valley ratio 2.25. The size of the mesas had no effect on the position and strength of the resonance.

4.3 Results and simulation of spin resolved current through the device.

I-V characteristics of the RTDs were measured in different magnetic fields in a range from 0 to 6T applied either perpendicularly to or in the plane of the quantum well. The results for perpendicular magnetic fields are presented in Fig. 4.2 (lines). For clarity, subsequent curves are offset by 10 μ A. It is clear from the figure that the resonance is split into two parts and that the splitting grows as a function of the magnetic field. At 6 T, the separation between the maxima of the split peaks is 36.5 mV and 42 mV for 4% and 8% Mn samples respectively. The broader feature which can be seen most prominently in the zero field curve at approximately 165 mV (180 mV) for the 4% (8%) of Mn samples is an LO phonon replica [LAE⁺89].

To explain the magnetic field-induced behaviour of the resonance, we develop a model based on the Giant Zeeman splitting for the spin levels in the DMS quantum well. First, we extract the series contact resistance of the RTD from the measured I-V curve at zero magnetic field [MLSE94, LMS⁺94]. Then we assume that each of the two spin split levels have the same conductance, and therefore that each carries half of the current in the device.

We neglect the slight relative change of barrier height caused by the change in energy of the levels, and assume that the conductivity of each level is independent of magnetic field in the sense that for the same alignment between the emitter Fermi level and the well level, the conductivity will be the same. In other words, the conductivity of each level as a function of applied voltage in the presence of a magnetic field can be given by a simple translation of the zero field curve by a voltage corresponding to the energy shift of the pertinent spin level in the well.

After translation, we add the conductivity contributions of both the spin-up and the spin-down curves, and reinsert the series resistance to yield a modelled I-V curve at a given magnetic field. By comparing this I-V curve with the actual experimental curve at 6 T, we determine an optimal value of 330 Ohm (900 Ohm) for the series resistance for the 8% (4%) Mn sample. Using this value of the series resistance for all modelled curves, and fitting the modelled curves at each field to the experimental ones, we extract the voltage splitting of the levels ΔV as a function of the magnetic field. Fig. 4.2 shows the modelled I-V curves as the circles, which compare very well with the experimental data presented as the solid lines in the figure.

We now compare the values of ΔV extracted from this fitting procedure to the expected behaviour of the spin levels in the wells. The spin level splitting ΔE of the DMS as a function of magnetic field B is given by a modified Brillouin function [GPF79]:

$$\Delta E = N_0 \alpha x s_0 B_s (s g \mu_B B / k_B (T + T_{eff})),$$

where $N_0 \alpha$ is the s-d exchange integral, x , s , and g are the manganese concentration, manganese spin, and g-factor respectively, and μ_B is the Bohr magneton. B_s is the Brillouin function of

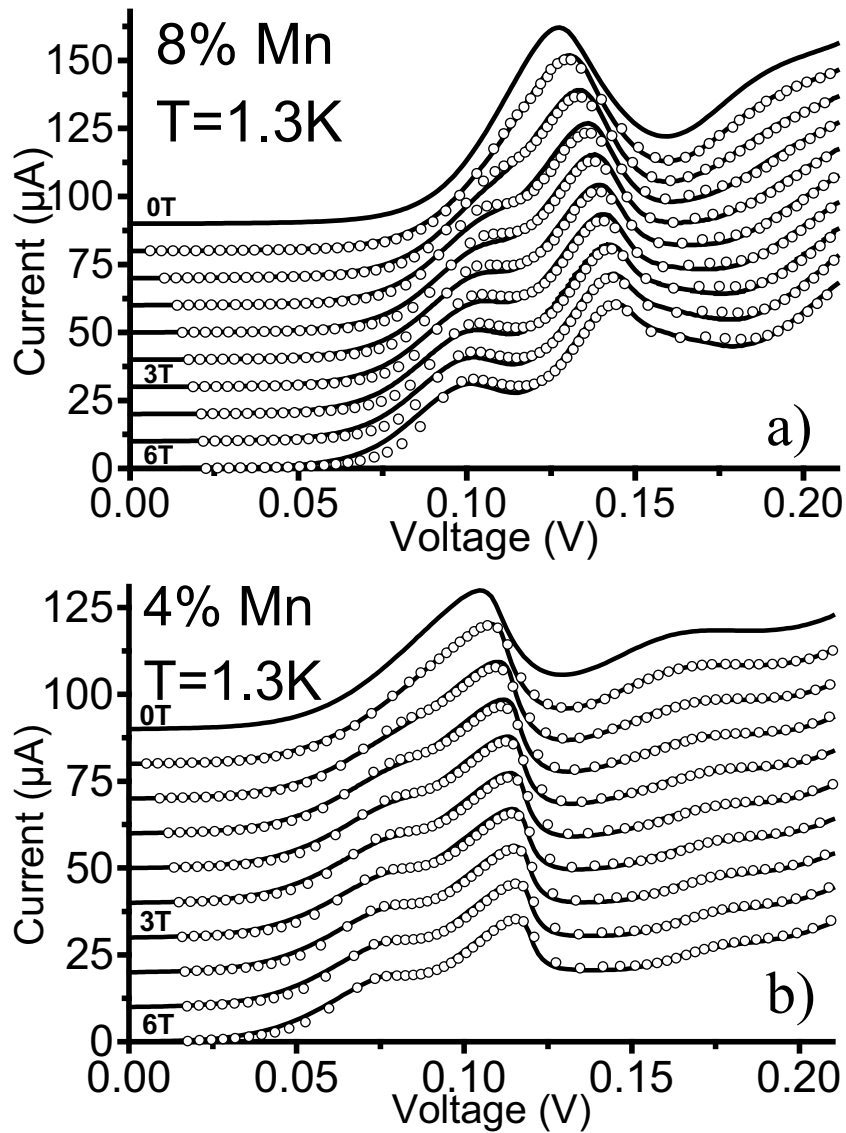


Figure 4.2: Experimental (lines) and modelled (circles) I-V curves for a resonance tunnel diode with a) $\text{Zn}_{0.92}\text{Mn}_{0.08}\text{Se}$ and b) $\text{Zn}_{0.96}\text{Mn}_{0.04}\text{Se}$ in the quantum well. Curves taken in $0.5T$ intervals from 0 to $3T$ and in $1T$ intervals from $3T$ to $6T$.

spin s . s_0 and T_{eff} are, respectively, the effective manganese spin and the effective temperature. These phenomenological parameters are needed to account for Mn interactions. Taking established values of $T_{eff} = 2.24$ K, $s_0 = 1.13$ [YTFP95] for $x=8\%$ ($T_{eff} = 1.44$ K, $s_0 = 1.64$ for $x = 4\%$) and $N_0\alpha = 0.26$ eV [TvODP84] from the literature, we obtain values for ΔE which are plotted as the solid lines in Fig. 4.3(a) for temperatures of 1.3, 4.2, and 8K and for Mn concentrations of 4% and 8%. These curves are compared with the values of ΔE extracted from the experiment (symbols in the same figure) for measurements taken at the respective temperatures. It is important to note that in order to correctly fit the amplitude to the Brillouin function, the measured values of ΔV must be divided by a lever arm of 2.1. The agreement between the magnetic field dependence of the experimental values and the Brillouin function is remarkable, suggesting that our model of two spin level splitting in a magnetic field captures the essential character of the device. More over an identical value of the lever arm is found for both the 4% and 8% Mn samples.

The existence of a lever factor between the experimental voltage splitting and the theoretical energy splitting in the well is a well-known feature of RTDs. It occurs because only part of the voltage applied to the device is dropped over the first barrier, and thus effective in determining the alignment condition for the resonance. Furthermore, extracting the lever factor for our diode by comparing the observed voltage splitting in the $B = 0$ I-V curve between the first resonance and the phonon replica to the known LO phonon energy of ZnSe (31.7 meV) [LB87] also yields a lever arm of around 2.

In Fig. 4.3(b) we compare measurements at 3T with magnetic field in the plane of, and perpendicular to the quantum well. The curves are offset for clarity. Evidently, the peaks in the I-V curve for in-plane magnetic fields are broader than those for perpendicular fields and are shifted slightly towards higher bias voltages. This effect is known from GaAs based RTDs [AMR⁺88] and can be explained in terms of momentum conservation. For magnetic field in-plane (perpendicular to the motion of the electrons) the Lorentz force will give the electrons an in-plane momentum. The conservation of in-plane momentum during the tunnelling process forces electrons to tunnel into finite momentum states of the quantum well, which are at a higher energy than the zero momentum ground state. Furthermore, the spread in in-plane k vectors leads to a broadening of the tunnelling resonance [AMR⁺88, DNP87]. From the figure, it is obvious that the splitting of the resonance peak is similar in both orientations of magnetic field. This is due to the isotropic g -factor in the DMS. This observation directly rules out any explanation of the peak structure as resulting from Landau level splitting in the quantum well.

Temperature dependent measurements of the 6T I-V curves are presented in Fig. 4.4, again with the curves offset for clarity. Qualitatively, an increase in temperature has a similar effect on the I-V curves as a reduction of the magnetic field (cf. Equ. 1). The peaks move closer together and eventually merge back into a single peak. On the other hand, the zero field I-V curves are practically temperature independent in the range from 1.3 Kelvin to 30 Kelvin. The reduction of the splitting as a function of field can be anticipated from the results of Fig. 4.3, and is simply a manifestation of the temperature dependence of the giant Zeeman splitting of the DMS. This suggests that any operational limit imposed on the device by temperature is purely a function of the material in the well, and that no inherent limit from the tunnelling process is detected.

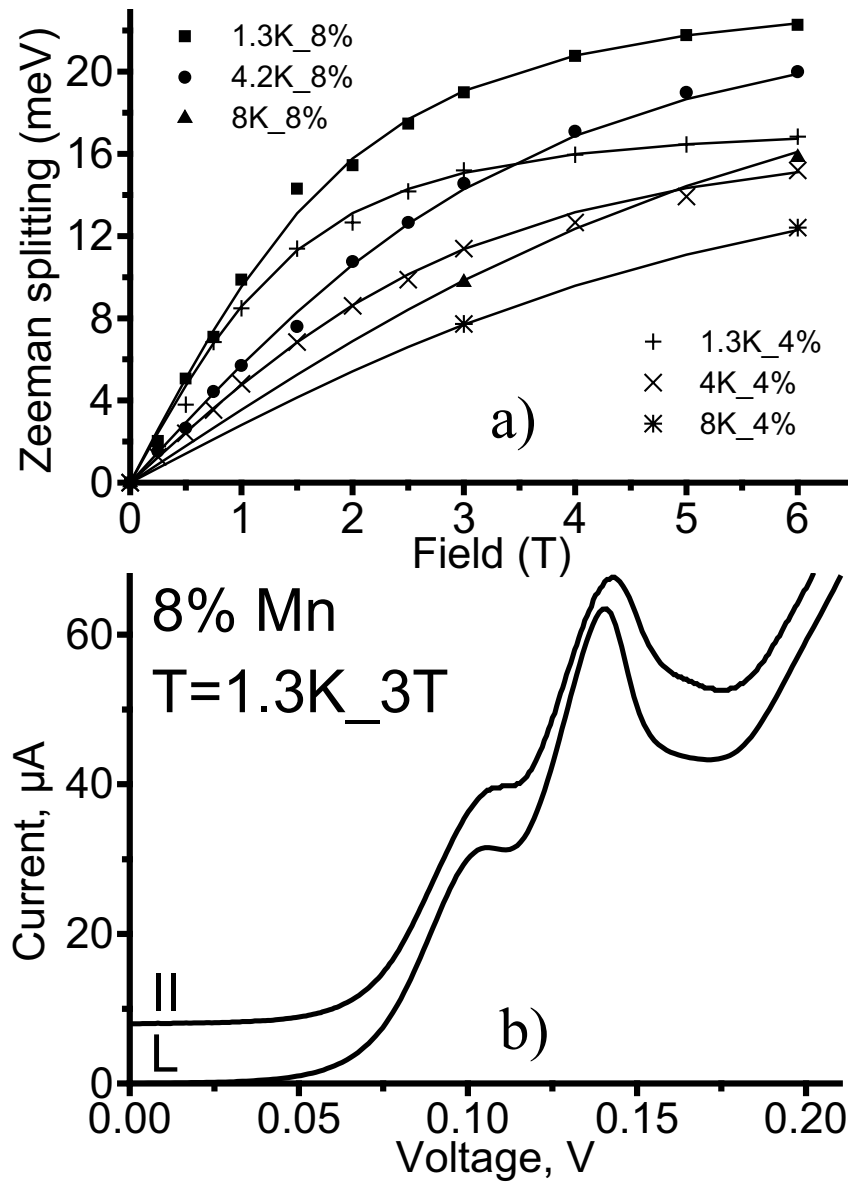


Figure 4.3: a) Giant Zeeman splitting versus magnetic field for both samples. The lines come from a Brillouin-like description of the well levels. The symbols represent the splitting in the peak positions extracted from the experimental data. b) I-V curves for sample with 8% Mn, under 3T in-plane (||) or perpendicular (L) magnetic field.

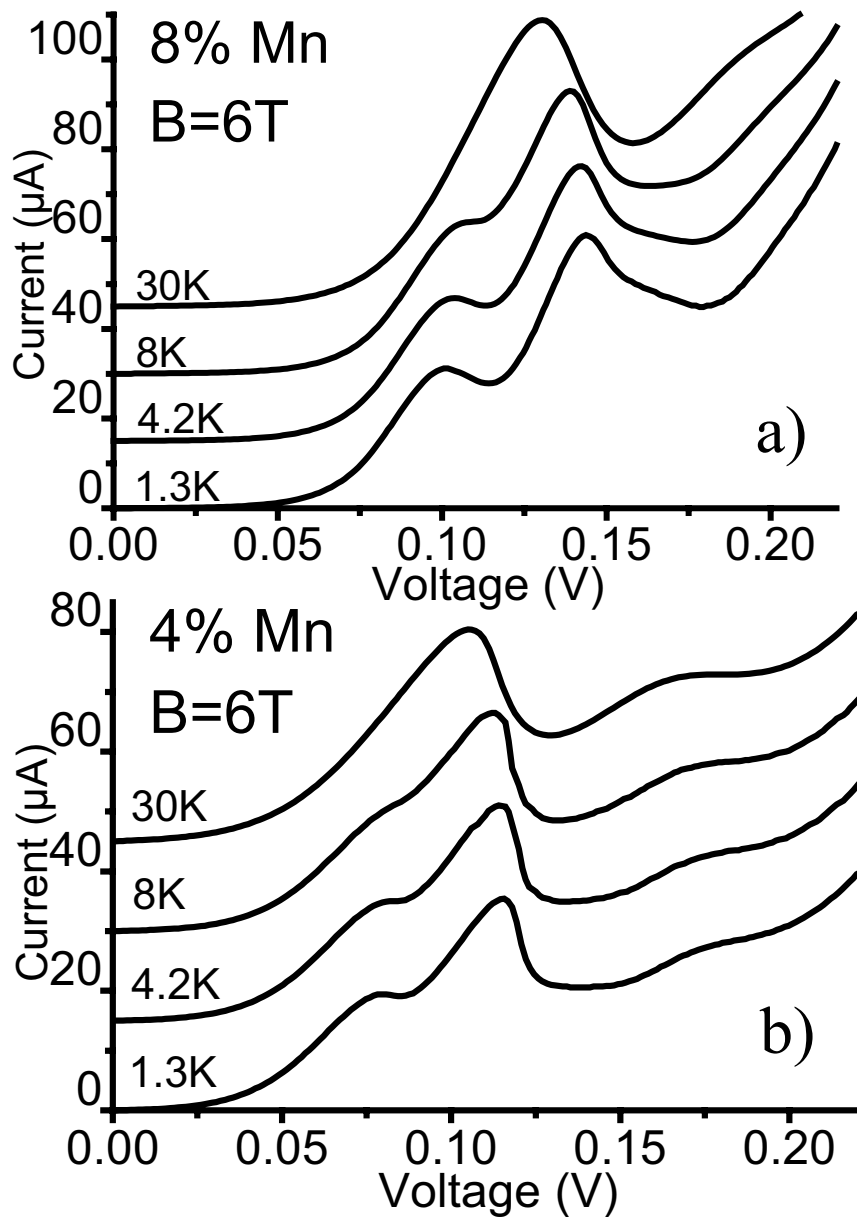


Figure 4.4: Temperature dependence of the I-V curves of the first resonance, shown for each of the diodes.

4.4 Summary.

To summarise, we have presented results of all II-VI semiconductor RTDs based on the (Zn,Be)Se system, with magnetic impurities (Mn) in the quantum well. A strong splitting of quantum well resonance is observed as a function of magnetic field, which originates from the Giant Zeeman splitting of the spin levels in the dilute magnetic semiconductor quantum well. An intuitive model that simulates the magnetic field dependence of the I-V characteristic of the device is discussed, and shows positive agreement with the experiment. The results therefore demonstrate the possibility of devices based on tunnelling through spin resolved energy levels. Experiments aiming to measure the spin polarization of the current flowing through such a device are currently underway.

Chapter 5

RTD with magnetic QW as a spin detector.

5.1 Spin polarization at high magnetic field.

As was already mentioned in the section 3.1.2, because of giant Zeeman splitting, a high spin polarization of the electron current (up to 100%) can be achieved in [Zn,Mn]Se DMS in intermediate magnetic fields [FKR⁺99]. Similarly, regular Zeeman splitting can, at high magnetic fields, lead to a spin-polarized current in the injector. Regular Zeeman splitting has a linear magnetic field dependence, and for ZnSe can be as big as 1.1 meV at 14 Tesla.

The conduction band profile for the RTD at high magnetic fields is shown in Fig. 5.1 with indication of the regular Zeeman splitting of the conduction band levels in the injector. The splitting is present throughout the entire device, but the injector spin polarization is most important for our experiment. Even though the Fermi energy in the injector is much larger than the regular Zeeman splitting, taking into account the conduction band profile, one can expect the incoming current to be spin-polarized. The spin polarization will change the electro-chemical potential in the injector and influence the resonance peaks. In the case of a nonmagnetic RTD, the spin polarization in the injector will be partially compensated. As the electro-chemical potential for one spin species decreases with increased spin polarization, the other will also increase.

In our case of giant Zeeman split levels in the QW, we expect current spin polarization in the injector to decrease the amplitude of the minority peak and increase that of the majority one. The majority current spin polarization is generated by the lower (in energy) regular Zeeman split states of the conduction band of the injector. The regular Zeeman splitting in ZnSe has the same sign as the giant Zeeman term for the [Zn,Mn]Se conduction band. This means that the majority current spin polarization corresponds to the lower giant Zeeman split level in the QW. The peak at higher bias (minority spin polarization) will thus decrease when the spin polarization of the current in the injector is increased. The effect of the current spin polarization is mainly observed at high magnetic fields because the regular Zeeman splitting at intermediate fields is relatively small compared to the estimated Fermi energy.

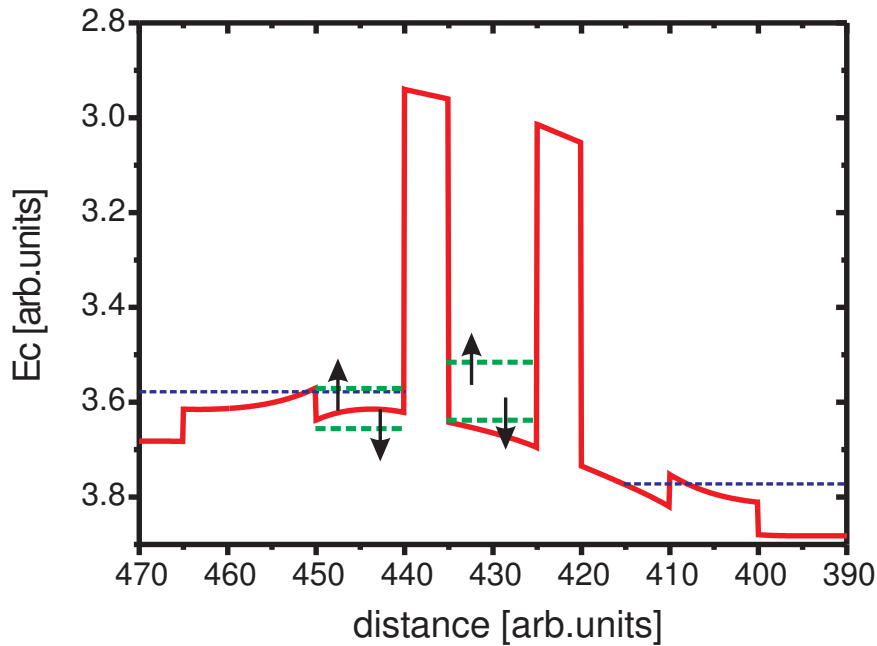


Figure 5.1: At very high magnetic fields, the regular Zeeman splitting in the nonmagnetic ZnSe injector spin polarizes the incoming current.

5.2 Influence of spin-polarized current on RTDs I-V characteristics.

The high magnetic field and low temperatures I-V dependence were measured in the 16 T ^4He bath cryostat and at Dilution Refrigerator.

In Fig. 5.2, I-V curves at 0 (red), 6 (blue) and 14 (magenta) T are shown. In the range of magnetic fields from 0 to 6 T the only major effect to be seen is the splitting of the levels in the QW that force the resonance peak to split in voltage. At magnetic fields higher than 6 T, the giant Zeeman splitting is basically saturated and does not have a strong influence on the position or the shape of the resonances with a greater increase in B. On the other hand, a very strong effect is still observable at magnetic fields above 6 T. The high voltage resonance decreases in amplitude and the low voltage one increases. This dependence is expected for spin-polarized current in the injector (see section 5.1).

The magnetic field dependence of the I-V characteristic for the sample with 8% Mn in the QW at 1 K is shown in Fig. 5.2 (left). The curves are offset by $25 \mu\text{A}$ for clarity. At the same time as the low voltage resonance increases in amplitude at high magnetic fields, the higher voltage resonance “practically” vanishes by 14 T.

I-V curves are shown in Fig. 5.2 (right) for the 4% Mn in the QW sample at 1.3 K. With the curves are offset by $15 \mu\text{A}$. The effect of spin-polarized current on this RTD I-V curve is not

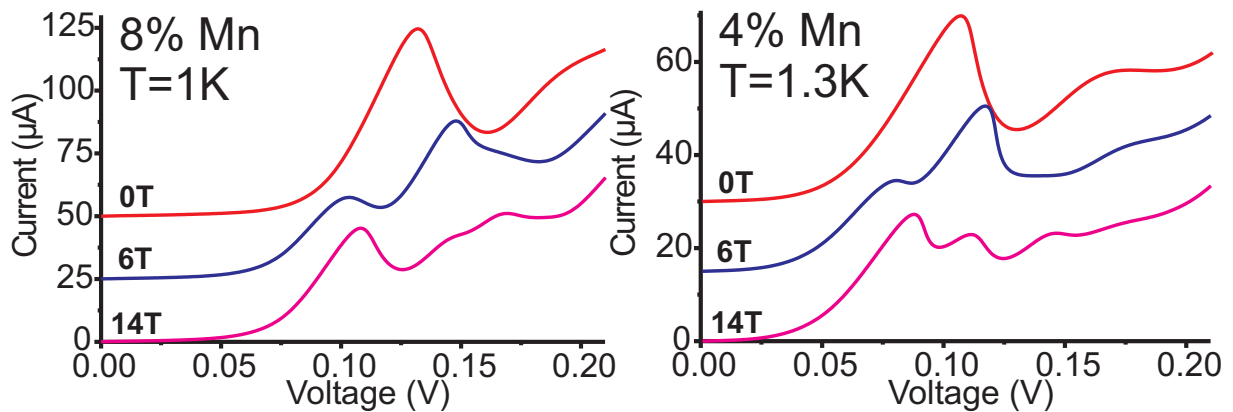


Figure 5.2: *I-V characteristics at high magnetic field are compared with 6 and 0 T curves. Left - the curves are shown for the sample with 8% Mn in the QW. Right - for the 4% Mn sample. In the range of magnetic fields from 6 to 14 T (when the giant Zeeman splitting is basically saturated) spin polarization of the current in the injector gradually suppresses the higher energy resonance and enhances the lower energy one.*

as big as for the sample with 8% Mn. On the other hand, the fact that both spin peaks and their phonon replicas are well pronounced at 14 T is obvious proof of the spin polarization in the injector changing the peak ratio.

In order to take into account orbital effects in a magnetic field perpendicular to the QW, very detailed (second derivative) analyses were performed. The negative of the second derivative plot is useful to analyse the position of the peaks because the peaks preserve their positions. Moreover, the appearance of the peaks is significantly magnified and even inflection on an I-V curve can become a full peak with a region of negative slope. For this reason, it is hard to interpret the shape of the resonance but the position of the maximum can be analysed.

In Fig. 5.3 the second derivative of the I-V characteristics of the 4% Mn sample are shown for perpendicular magnetic field ranging from 0 to 14 T in half Tesla steps. The measurements are done at 1.3 K and the curves are offset for clarity. Each resonance and its phonon replica pair at 14 T are identified by a number (1 or 2). The red line indicates a first Landau level quantized sub-peak in the phonon replica of the first resonance peak. In the presence of a perpendicular magnetic field, Landau level quantization within the phonon replica is expected [LAE⁺89] (see section 2.1.3). The voltage separation between the phonon replica peak and the Landau level at 14 T is indicated by the green arrow and corresponds to the expected energies of the first Landau level with a leverage factor near 2.1 (similar to the results obtained from the giant Zeeman splitting of the levels in the QW). No additional peaks were found in the I-V characteristics, even in the second derivative plot, indicating that the elastic scattering is reasonably low in our samples.

The in-plane high magnetic field dependence of the I-V characteristic for the sample with 4% Mn in the QW at 1.3 K is shown in Fig. 5.4. The curves are measured every half Tesla and offset for clarity. The giant Zeeman split resonant peak seen up to 5 Tesla seem to be gone on the 14 T

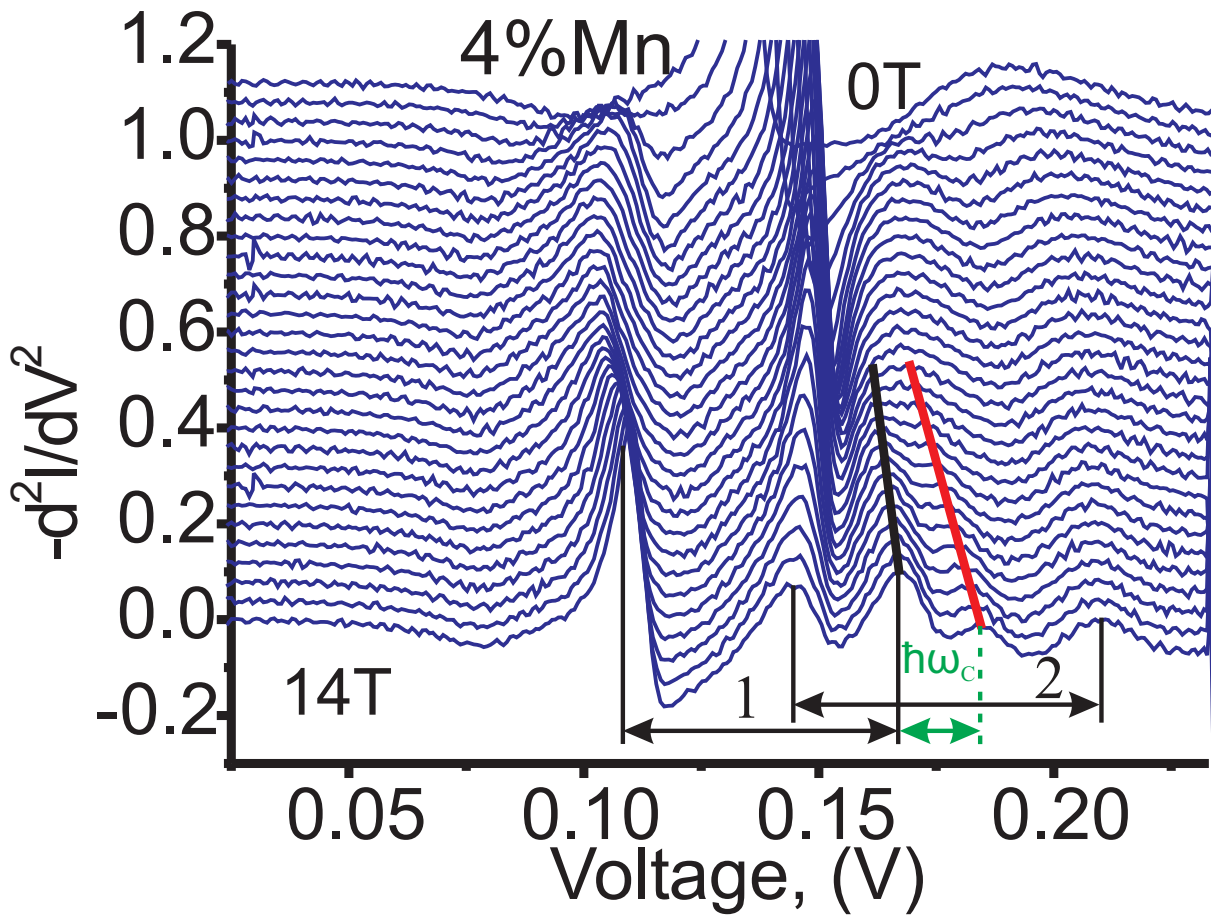


Figure 5.3: Negative of second derivative of the current versus voltage at 1.3 K measured in the perpendicular magnetic fields from 0 to 14 Tesla (see Fig. 5.2 right). The black line shows the phonon replica of the first resonance and the red line shows first Landau level.

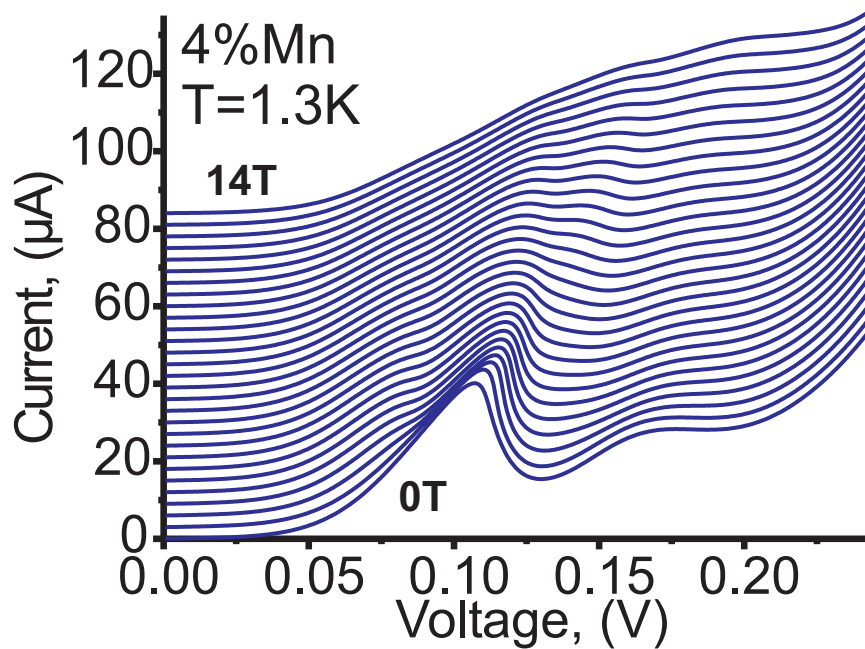


Figure 5.4: *In-plane to the QW magnetic field dependence of the I-V curve at high magnetic fields.*

curve. As was shown in section 2.2.2 under in-plane magnetic field the k-vector conservation and Lorentz force smooth the resonance peak and the extreme case of this effect is seen in the figure.

The second derivative analysis of the 14 T in-plane magnetic field I-V curve for the 4% Mn sample is shown in Fig. 5.5. As one can see, the resonances are well detectable even though they are not obvious in the I-V curve. Each resonance peak and its phonon replica pairs are indicated by a number (1 or 2). Additionally, the second LO phonon resonance of the first resonance is indicated by 1'. It results from tunneling electrons getting into the QW resonance level energies after losing the energy of LO phonon twice.

5.3 Temperature dependence of the effect.

For [Zn,Mn]Se with 8% Mn, the Mn concentration dependent effective temperature (T_{eff}) in the equation for the giant Zeeman splitting Eq. 3.2 has a value of 2.24 K [TvODP84]. Reducing the temperature to much lower than T_{eff} should not have a great effect on the value of giant Zeeman splitting, especially at high magnetic fields. On the other hand, from the phase diagram of the DMS ternary compound Fig. 3.3 (left) one can guess that at low temperatures a magnetic phase transition from paramagnetic to spin glass magnetic state can happen.

In Fig. 5.6, 40 mK I-V curves are shown in the magnetic field range from 0 to 16 T with 2 T

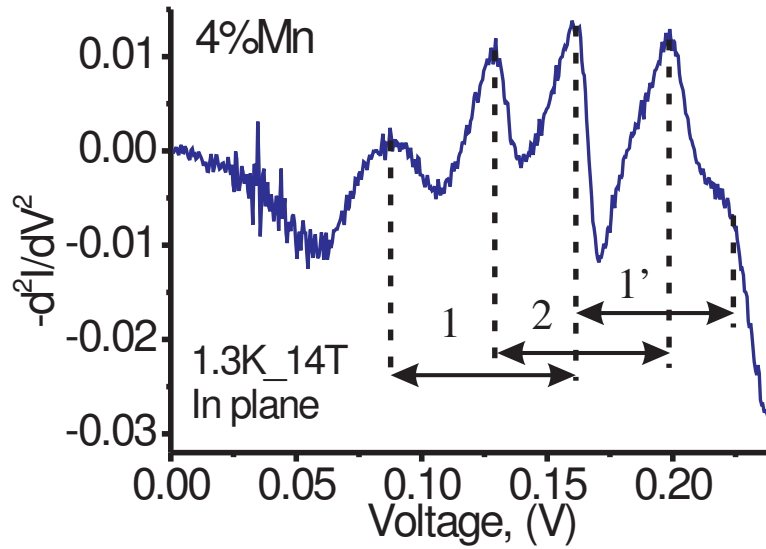


Figure 5.5: Reversed second derivative of the current versus voltage at 1.3 K measured in the in-plane magnetic field 14 Tesla (see Fig. 5.4). By 1' the second phonon replica of the first resonance is shown.

steps. The curves are offset for clarity. The limiting factor for the temperature was a current heating the sample but not the Dilution Refrigerator which has a base temperature of 5 mK. From the data, it is possible to conclude that the giant Zeeman splitting did indeed not change much in the temperature range between 1 K and 40 mK. Moreover, the fact that the splitting corresponds to the value expected for the giant Zeeman splitting in the paramagnetic [Zn,Mn]Se suggests that no magnetic phase transition took place at these temperatures.

In Fig. 5.7 (left), the regular Zeeman splitting dependence of the I-V characteristic of the RTD at various temperatures with a magnetic field chosen to keep giant Zeeman splitting (shown by $dE_{Gzeeman}$) constant, is presented. Under these conditions, one can see that at higher temperatures the spin resolved peak ratio is changed. The reason for this happening is simple. The giant Zeeman splitting has a strong temperature dependence and thus the magnetic field needed to reach the chosen value of $dE_{Gzeeman}$ at higher temperatures is much greater than at lower temperatures. The regular Zeeman splitting, however, is temperature independent and has a linear magnetic field dependence. At higher temperatures, and accordingly at higher magnetic fields, the regular Zeeman splitting in the injector polarizes the current and the peak ratio changes. When the temperature is decreased, a lower magnetic field is needed to preserve the value of the giant Zeeman splitting and the smaller value of the regular Zeeman splitting is not sufficient to polarize the current in the injector as efficiently. This is why the peak ratio returns to the values expected for a non polarized injector electrons. The temperatures at which the I-V curves were measured are shown in the legend on the left side, whereas the right side legend gives the corresponding values of the regular Zeeman splitting in the injector.

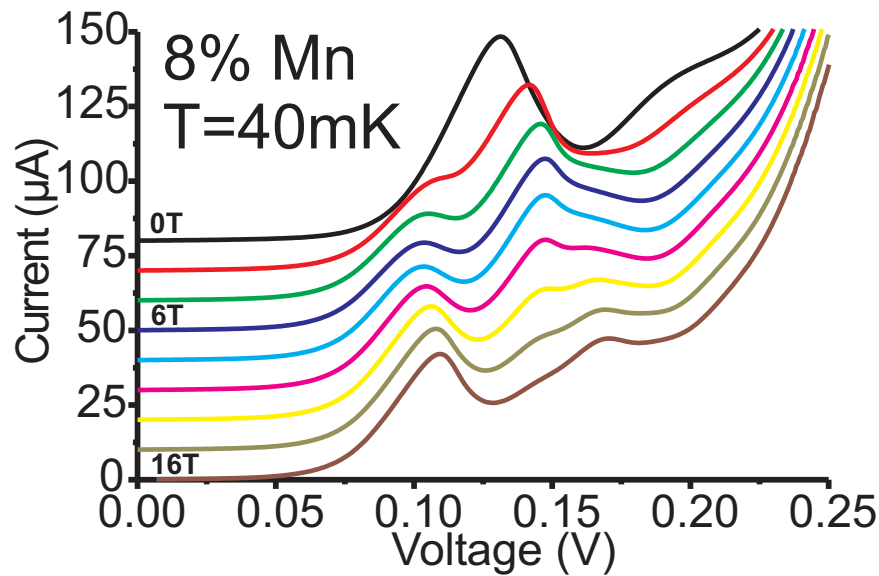


Figure 5.6: Very low temperature (40 mK) I-V curves measured to high magnetic fields showing no magnetic phase transition in the 8% Mn DMS at this temperature.

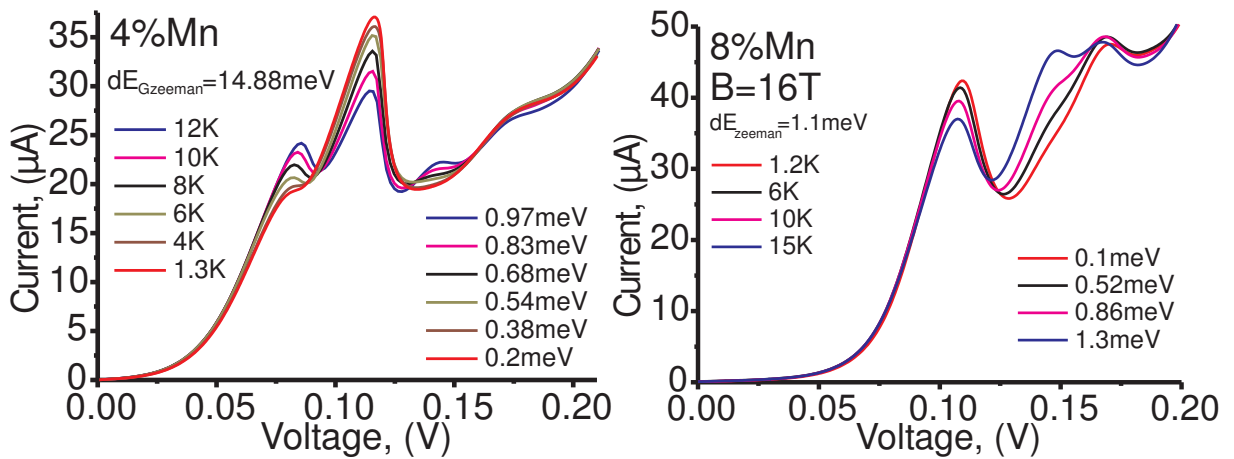


Figure 5.7: Left - the regular Zeeman splitting dependence of the I-V characteristic of the RTD at different temperatures with magnetic field chosen to keep giant Zeeman splitting (shown by $dE_{Gzeeman}$) constant. The temperatures are shown in the legend on the left and corresponding values of regular Zeeman splitting are shown in the legend on the right. Right - temperature dependence of the I-V curve at 16 Tesla (constant regular Zeeman splitting shown as dE_{zeeman}). In the right legend kT calculated from the temperatures in the left legend are shown.

In Fig. 5.7 (right), the temperature dependence of the effect of the spin polarization in the injector is shown. The I-V characteristics measured at different temperatures and constant (high) 16 T magnetic field. The regular Zeeman splitting (dE_{zeeman}) at the magnetic field is 1.1 meV . In this temperature range the giant Zeeman splitting has a weak temperature dependence. The temperatures at which the I-V curves were measured are shown on the left side and the corresponding values of kT are shown in the legend on the right. At higher temperatures the peak ratio changes its value to that observed at lower magnetic fields $\leq 6 \text{ T}$. This is caused by the temperature-induced decrease in spin polarization of the current in the injector. By comparing the values of the regular Zeeman spin splitting of the conduction band in the injector with the value of temperature broadening described by kT , one can already see at 12 K that kT is bigger than the Zeeman splitting, causing the reduced spin polarization seen in our measurement.

Chapter 6

Double RTD with magnetic QWs for current spin polarization and detection.

In Fig. 6.1, a schematic diagram of a non-local measurement scheme for a double RTD structure is shown. The RTDs are biased independently and connected (within spin flip length of each other) in the collector contact. Current spin polarization created by one of the RTDs influences potential drop over the other. The spin dependant difference in potential drop over the structure is caused by the difference in electro-chemical potential of spin polarized collector electrons. This can be understood in analogy to band bending in the injector when charge accumulation changes the band profile. If the sign of collector spin polarization matches the spin polarization of the resonance peak, the peak position is shifted to a lower bias at increased spin polarization. This shift is proportional to the increased electro-chemical potential for the corresponding spin orientation. Correspondingly, the electro-chemical potential for minority spin-polarized electrons decreases, and the spin resonant peak shifts to higher bias at higher spin polarization.

A simulation procedure similar to the one used for the magnetic field dependence of the RTD

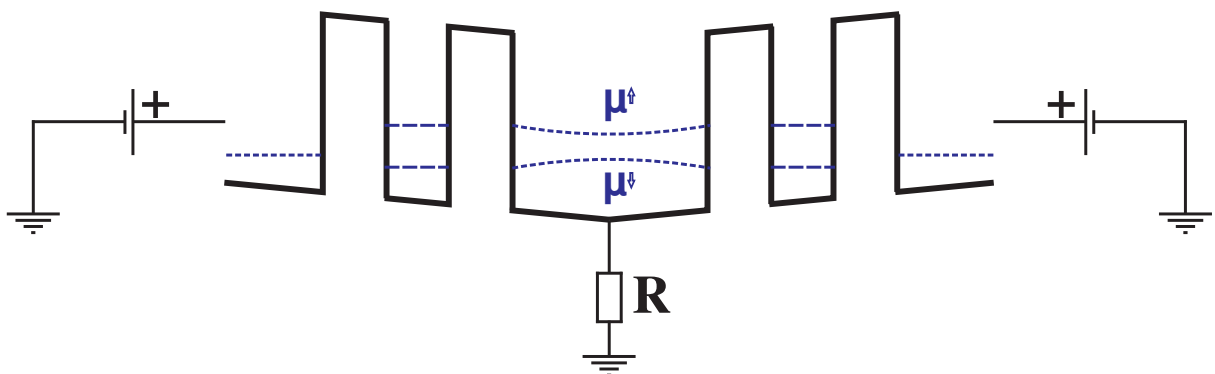


Figure 6.1: Schematic diagram of the double RTD with magnetic QW structure in magnetic field under bias.

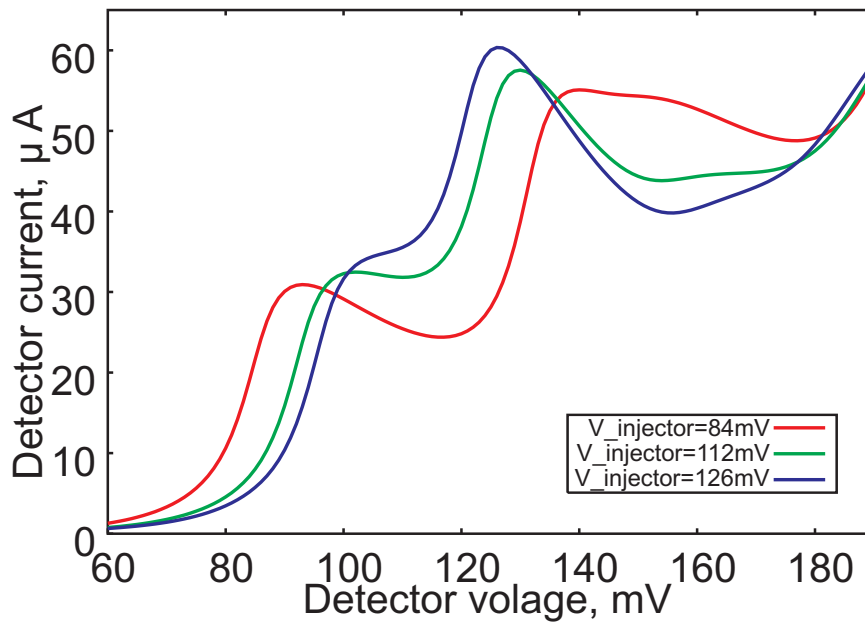


Figure 6.2: *I-V characteristics of the detector RTD as a function of the bias over the injector RTD.*

with magnetic QW (see section 4.3) is applied to predict the collector spin polarization dependence of the RTD I-V characteristic in constant magnetic field. The spin polarization is recalculated from the I-V curve of the simulated RTD with magnetic QW.

Fig. 6.2 presents results of a calculation of the detector RTD I-V characteristics in a magnetic field and with the incoming current polarized by a similar RTD structure. To simplify the discussion, one of the structures will be called the simulated RTD "detector" and the RTD producing the spin polarization "injector". In a real structure the devices will have a symmetric influence on each other and the problem should be solved self-consistently, but our simplified approach illustrates the ideas.

Depending on the voltage drop on the injector RTD, the collector current spin polarization of the detector RTD will correspond to the lower or higher energy resonant peak. In the case of spin polarization of the same sign as the lower energy peak, the first peak will shift to lower bias and the higher energy peak will shift to a higher bias. The separation between the peaks will thus increase. This situation is shown in Fig. 6.2 by the red curve. When the collector spin polarization corresponds to the spin polarization of the higher resonance, the separation between the peaks will decrease as shown by the blue curve in the figure. An intermediate state with lower spin polarization is shown by the green curve.

A three dimensional representation of the injector RTD voltage drop influence on the I-V characteristic of the detector RTD is shown in Fig. 6.3. The peaks move apart when the spin polarization corresponds to the lower resonance in the injector RTD and becomes closer when the spin polarization is the same sign as the higher resonance. The peaks move to the expected values when the spin polarization decreases.

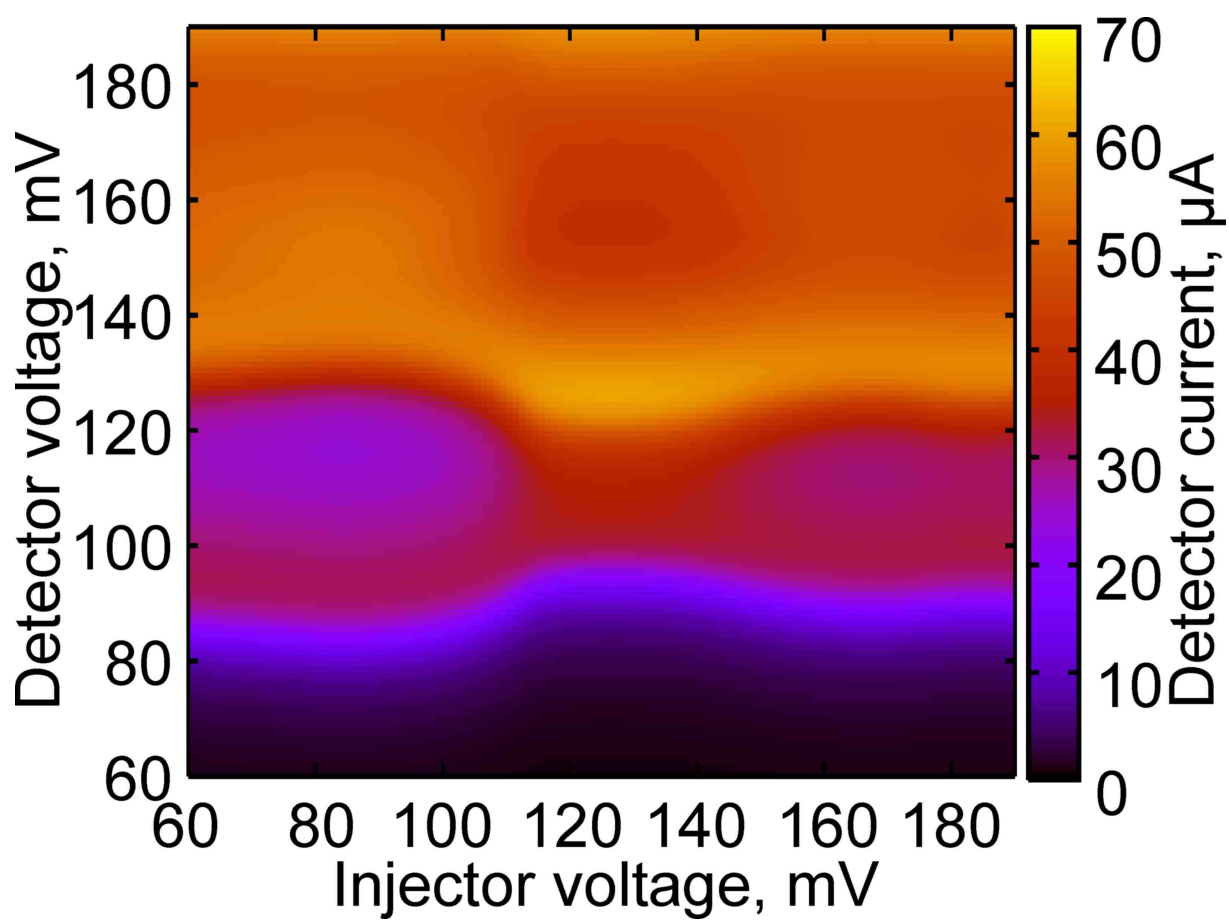


Figure 6.3: Colour plot of the detector RTD current as a function of the bias over the injector and the detector RTDs.

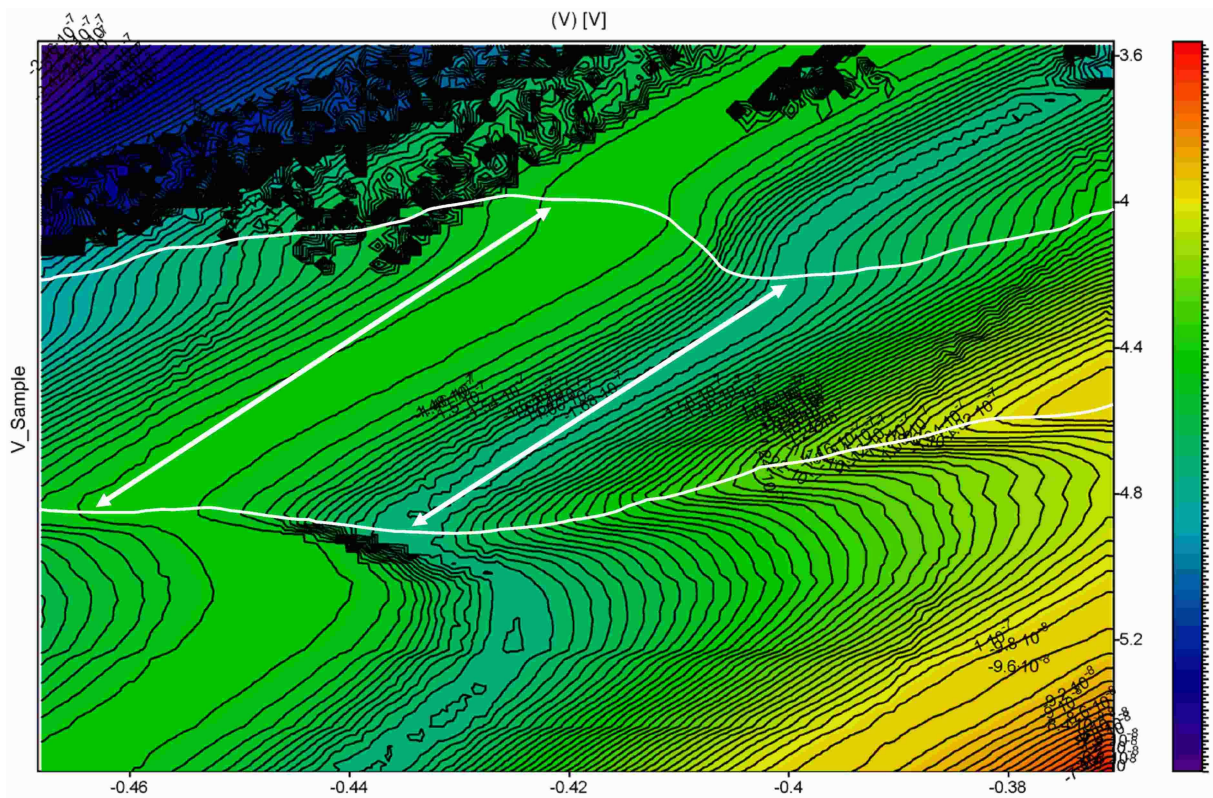


Figure 6.4: Colour plot of the measured detector RTD current as a function of the bias over the injector and the detector RTDs.

Fig. 6.4 presents preliminary results of measurements on a double RTD structure operated in the configuration sketched in Fig. 6.1, done by A. Gröger. The RTDs with [Zn,Mn]Se QW were patterned in two 800 nm square mesas separated by a distance of 200 nm and measured at 4 K and 6 T. The white lines are guides to the eye indicating the resonance peaks corresponding to one of the RTDs. The arrows show the crossing points of the resonance peaks of the injector and collector RTDs. The crossing points are separated differently, depending on the resonance with which the crossing is happening. The result could be interpreted as an effect of the collector spin polarization.

Chapter 7

RTD with magnetic injector or barriers for spin manipulation.

7.1 Introduction and the magnetic injector sample design.

Some interesting designs for eventual spintronics devices are structures based on magnetic semiconductor resonant tunneling diodes (RTDs) which have promising futures as spin filters and spin aligners. However, before these structures can make their way into actual devices, we must first understand the basic behaviours of these magnetic structures and how they differ from their non-magnetic counterparts. We have previously explored the behaviour of RTDs with a magnetic quantum well [SGS⁺03] and now turn our attention to RTDs fitted with magnetic injectors. Here, the polarization of spin originates in the bulk behaviour of the injector, and the RTD itself is ostensibly a non-magnetic device which is fed with a polarized source of electrons. As a magnetic field increases, we observe important changes in the transport characteristics of the RTD stemming from the realignment of the band profile in the device, and explain how this can be understood in the framework of a Landauer-Büttiker-type model. The correct understanding of this mechanism is therefore essential before proceeding to more sophisticated device structures combining spin injection, detection and manipulation.

The studied sample is an all II-VI semiconductor resonant tunneling diode structure with a conduction band profile similar to that used in previous work on II-VI and III-V [SGS⁺03] and fitted with a dilute magnetic semiconductor (DMS) injector layer. The tunneling region consists of a 9 nm thick ZnSe quantum well (QW) sandwiched between two 5 nm thick Zn_{0.7}Be_{0.3}Se barriers. Below the tunneling region is a 10 nm thick ZnSe collector layer. The injector is a 10 nm thick Zn_{0.94}Mn_{0.06}Se layer which is used to inject spin polarized electrons into the diode. The remaining layers are needed to ensure a proper doping profile and to allow for the fitting of high quality ohmic contacts. Full details of the layer stack are given in Fig. 7.1(a).

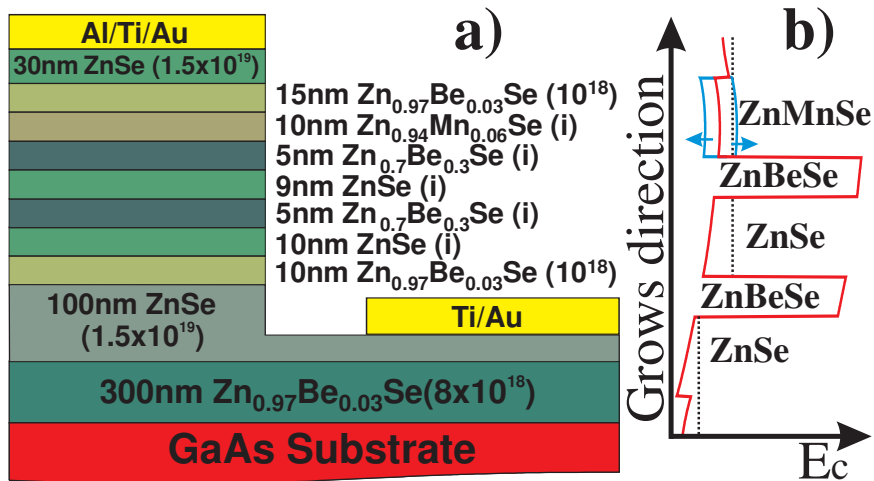


Figure 7.1: a) Layer structure of the device and b) schematic view of resonance tunnel diode band structure under an applied bias.

The contact resistance of the devices is kept to a minimum by using an in-situ Al(10 nm)/Ti (10 nm)/Au (30 nm) top contact, while the ex-situ bottom contact is fabricated by etching down to the very highly doped ZnSe layer, and using large area ($500^2 \mu\text{m}^2$) Ti-Au contact pad. The sample is patterned in $100 \mu\text{m}^2$ pillars using standard optical lithography, which wet each and lift-off.

Measurements are performed in ^4He bath cryostat equipped with a high field superconducting magnet using standard DC transport techniques. Care was taken to construct a circuit with a low (40Ω) resistor in parallel to the diode to prevent the diode from going into oscillations in the negative differential conductance region [LAE⁺89]. Current measurements consist of measuring the voltage drop across a relatively small 30 Ohm series resistor.

A schematic of the band profile is shown in Fig. 7.1. Both the injector and collector sides of the tunneling structure are gradient doped in order to insure a relatively low Fermi energy at the point of injection, and thus a sharp resonance [WC91]. Under the influence of an external magnetic field, the DMS injector exhibits giant Zeeman splitting of up to 20 mV in the conduction band, and the degeneracy of its spin states is lifted following a Brillouin function [GPF79], creating a spin-polarized carrier population via the transfer of electrons from the higher energy spin band to the lower one. In order to maintain proper alignment of the Fermi energy, this imbalance in the population of the two spin species must lead to a splitting of the bottom of the spin up and spin down conduction bands, leading to different band profiles for each of the spin species in the injector region, as indicated in the diagram.

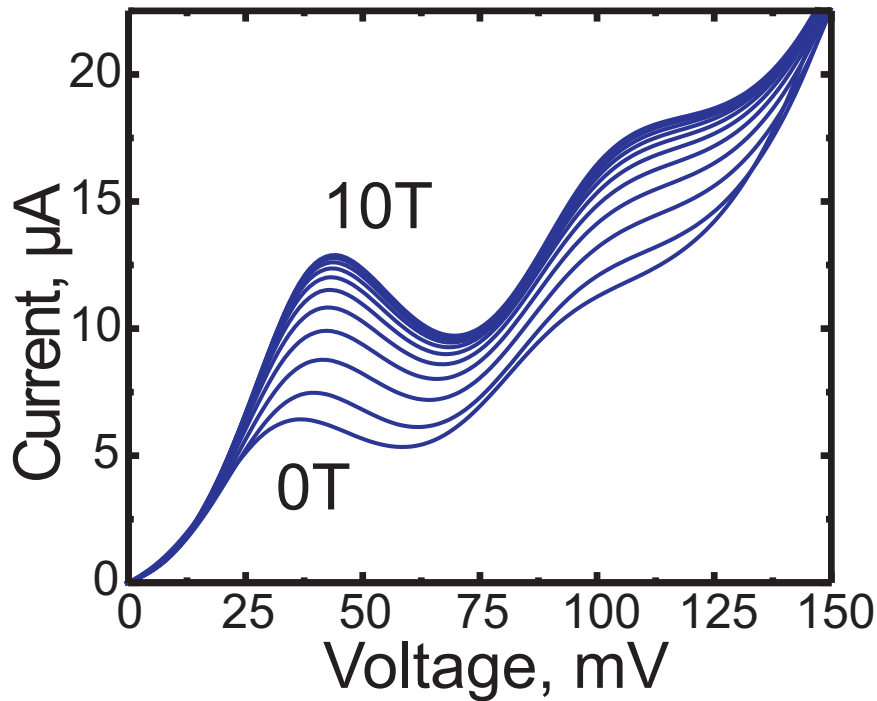


Figure 7.2: Magnetic field dependence of the I-V curves of the first resonance at 4.2 K.

7.2 Magnetic field induced change of I-V characteristic of RTD structure with magnetic injector.

Current-voltage characteristics for the device for different amplitudes of perpendicular-to-plane magnetic fields (B) are shown in Fig. 7.2. At zero field, the sample has typical RTD behaviour, showing a strong resonance peak at 36 mV with a peak to valley ratio of just over 1. The additional resonance visible at 96 mV in the $B = 0$ curve is the well known LO phonon replica [LAE⁺89], which is separated from the direct resonance by the energy of the LO phonon of the well material, and can be used to calibrate the voltage scale to energy levels in the QW. A resonance associated with the second well level occurs at around 0.3 V (not shown in the figure). As is often the case, the resonances for the negative bias direction are not as pronounced. We confirmed the absence of charging effects in the device by verifying that I-V curves for different sweep directions were identical [MLSE94].

As a magnetic field is applied, the peak shifts to higher voltages and strongly *increases* in amplitude. The strongest dependence of the peak amplitude and position on the magnetic field is observed at low fields, with the behaviour saturating before 10 T. The behaviour is therefore consistent with the Brillouin like behaviour expected from the giant Zeeman splitting of the injector. Note also that the phonon replica causes a higher energy echo of the QW state, but since the effects we are studying result from properties of the injector, the phonon replica peak simply follows the magnetic field dependence of the main resonance.

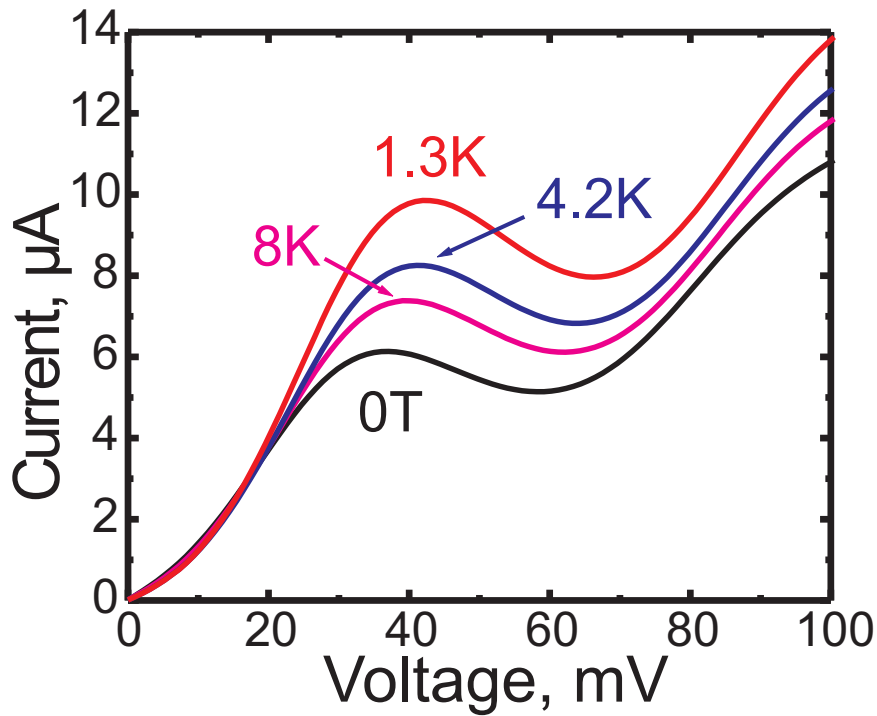


Figure 7.3: *Temperature dependence of the resonance.*

Figure 7.3 shows the temperature dependence of the 2 T I-V curve for temperatures from 1.3 to 8 K. The $B = 0$ curve, which is temperature independent in this range, is included for comparison. It is clear that the increase in temperature has a similar effect on the I-V curves as a lowering in the magnetic field would. Indeed, we verified that the only effect of temperature is to rescale the effect of the magnetic field on the Zeeman splitting in the injector, exactly as would be expected from the argument of the Brillouin function that scales as $B/(T + T_{\text{eff}})$ as described below.

7.3 Explanation of magnetic field influence on the transport in RTD with magnetic injector.

The slight shift of the peak to a higher bias with increasing magnetic field is fairly intuitive and can be directly expected from the schematic of Fig. 7.1. It is well established that the maximum of resonance occurs when the bottom of the conduction band is brought into alignment with the well level[Lur85]. As the field increases, the peak becomes evermore dominated by the majority spin conduction band. Since the bottom of this band is moving to lower energies, a higher bias will be required to bring this band into alignment with the well level, producing a shift of resonance towards a higher bias.

The large increase in the current amplitude is also related to the change of the conduction

band energy with magnetic field B , but its manifestation is somewhat more subtle. Let $E_\sigma = E_c + sh/2$ denote the spin-split band bottom with h as the spin splitting [$s = +(-)$ for $\sigma = \uparrow(\downarrow)$]. Due to the exchange interaction between localised Mn ions and band electrons there arises in the DMS a giant Zeeman splitting,

$$h = N_0\alpha x S_0 B_S [Sg\mu_B B / k_B(T + T_{\text{eff}})], \quad (7.1)$$

where $N_0\alpha$ is the exchange integral, x the Mn concentration of $S = 5/2$ Mn spins, g is the Lande factor, B_S the Brillouin function, and S_0 and T_{eff} are the Mn effective spin and temperature, respectively. One might naively expect that a spin splitting of the conduction band leaves the DMS injector electron density constant (keeping E_F fixed). This is indeed correct for a 2D injector [SMP02] since the spin-dependent density $n_\sigma = (m/2\pi\hbar^2)(E_F - E_\sigma)$ is independent of the energy because the density of states is constant. However, for a 3D system n_σ depends *nonlinearly* on h , thereby the total electron density $n = n_\uparrow + n_\downarrow$ is shown to be an *increasing* function of h provided E_F remains fixed. Since the current peak is mainly determined by n , it follows from Eq. 7.1 that the peak amplitude increases with B . Therefore, the current increase effect has a *geometrical* origin.

To gain further insight, we perform numerical simulations of the electron transport along the z -direction [growth direction, see Fig. 7.1(b)]. Because a similar peak amplitude increase is also observed when B is an in-plane magnetic field indicating that the effect is independent of the direction of the magnetic field, orbital effects are not taken into account. In addition, we neglect spin relaxation effects and the current density $J = J_\uparrow + J_\downarrow$ is thus carried by both spin species in parallel,

$$J_\sigma = \frac{em}{4\pi^2\hbar^3} \int_{eV+sh/2}^{\infty} dE_z dE_\perp T_\sigma(E_z, \varepsilon_0, V) \times [f_L(E_z + E_\perp) - f_R(E_z + E_\perp)], \quad (7.2)$$

with V the bias voltage applied to the structure. We take into account the spin splitting in the longitudinal energy E_z . The Fermi functions f_L and f_R describe the distribution of electrons with total energy $E_z + E_\perp$ in the left and right leads with electrochemical potentials $\mu_L = E_F$ and $\mu_R = E_F - eV$, respectively. Band-edge effects are incorporated in the lower limit of the integral.

In Eq. 7.2, the transmission T conserves the momentum parallel to the interfaces and depends, quite generally, on E_z , V and the subband bottom energy ε_0 of the quantum well. Close to resonance, it is a good approach to take a Lorentzian shape, $T_\sigma = \Gamma_\sigma^L \Gamma_\sigma^R / [(E_z - \varepsilon_0)^2 + \Gamma^2/4]$, where Γ_σ^L (Γ_σ^R) is the partial decay width due to coupling to the lead L (R) and $\Gamma = \Gamma_L + \Gamma_R$ the total broadening per spin. We hereinafter consider symmetric barriers for simplicity but it

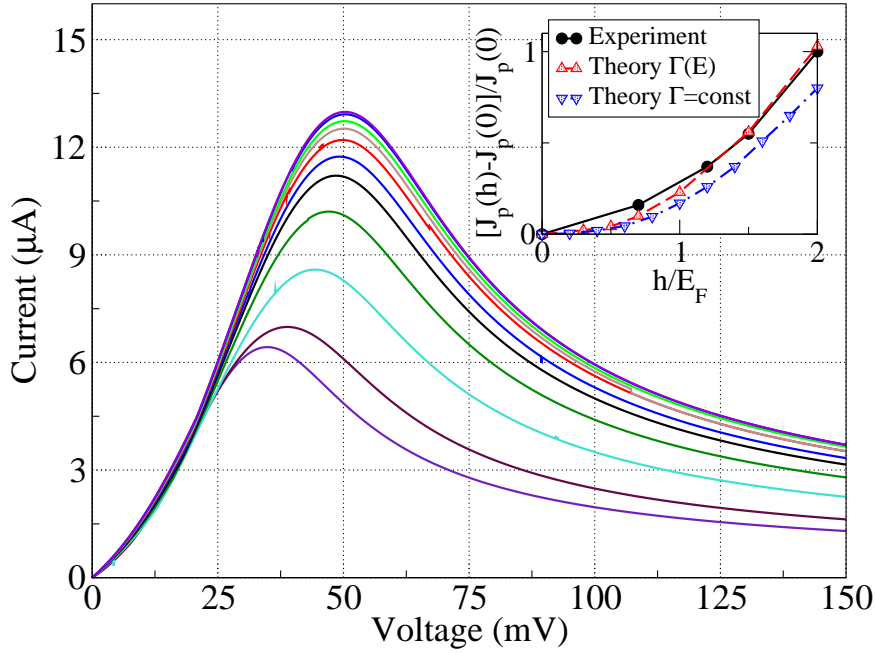


Figure 7.4: Theoretical I - V curves at 4 K for an RTD with a spin-polarized injector increasing the spin splitting from $h = 0$ to $h = 2E_F$ in steps of $h = 0.2E_F$ (from bottom to top). Inset: normalized current peak J_p as a function of h . Experimental and model data are shown for comparison.

is important in the strongly nonlinear regime (i.e. around the current peak) to take into account the energy (and voltage) dependence of the tunneling rates[BB99]. The barrier height is given by the conduction band offset between ZnSe and $\text{Zn}_{0.7}\text{Be}_{0.3}\text{Se}$, which is approximately 0.6 eV. Using ZnSe parameters we find for the first resonant level $\varepsilon_0 = 21$ meV. Now spin saturation takes place at around $h = 20$ meV, thereby $E_F = 10$ meV. This implies that for small resonance width the onset of the I - V curves of Fig. 7.2 should occur at $\varepsilon_0 - E_F = 11$ meV. This fact, together with the low peak-to-valley ratio that the I - V curves exhibit, suggests a large value of Γ , probably due to disorder or interface roughness. Therefore, we set $\Gamma = 15$ meV at $V = 0$ and $h = 0$ and fit the peak current at $B = 0$ with the experimental value.

We show the results in Fig. 7.4 from $h = 0$ to $h = 2E_F$. The I - V curves reproduce the experimental observations and the agreement is fairly good. The negative differential conductance region extends all the way from the resonance peak because we consider only the first resonant level. We note that in Fig. 7.4 the voltage axis is scaled with a lever arm $\mathcal{L} = 2$, consisted with that extracted from the position of the phonon replica. Since the broadening is a large energy scale, we can expand Eq. 7.2 at zero temperature in powers of $1/\Gamma$. We find for small spin splittings that the resonance peaks at $eV_{\text{res}}/\mathcal{L} = \varepsilon_0 - E_F/3 + h^2/3E_F$. Substituting the parameters, we obtain $V_{\text{res}} = 37$ mV at $h = 0$, in accordance with Fig. 7.2. Moreover, this expression clearly shows the shift of V_{res} with increasing h . Inserting this result into Eq. 7.2 we find to the leading order of $1/\Gamma$ that the current peak $J_p = (em/2\pi^2\hbar^3)E_F^2(1 + h^2/4E_F^2)$ is indeed an increasing function of the magnetic field. In the inset of Fig. 7.4 we present the current peak as a function of h , showing a remarkable agreement with the experimental observations.

In comparison, we provide the current increase when the energy dependence of Γ is neglected, which qualitatively agrees with our results, indicating that the simple model (7.2) captures the key points of the experiment.

The results we obtain are reminiscent of Ref. [CW92], where the In content of a GaInAs emitter in a III-V RTD is varied. As a consequence, the band alignment changes and the peak current increases. In our case, the increase is due exclusively to the giant spin splitting in the injector. Thus, the current increase can be tuned with a magnetic field without changing the sample parameters.

In conclusion, we have presented I - V characteristics of a II-VI resonant-tunneling diode attached to a diluted magnetic semiconductor injector. We have observed both an enhancement and a voltage shift of the resonance current peak when the applied magnetic field increases. The results are consistent with a giant Zeeman splitting in the injector since the current saturates at a few Tesla and the temperature dependence follows the magnetisation of a paramagnetic system. The Zeeman splitting induced redistribution of spin carriers in the injector leads to a modification of the conduction band structure of the device which is responsible for the changes in transport properties. We have discussed a transport model which replicates most of the features seen in the experiment. Our findings offer the unique possibility of producing high peak currents which arise from spin effects only.

7.4 RTD with magnetic barriers for spin manipulation.

An interesting sample design with diluted magnetic material in the barriers of the RTD device might also be expected to trigger a rise in spin selection in the structure. In a magnetic field the height of the barriers will be modified for each spin orientation. Taking into account that tunneling probability has an exponential dependence on the barrier height, even a small change in the barriers could drastically change the I - V characteristic.

The schematic conduction band profile for a sample with 6% Mn [Zn,Mn]Se DMS barriers under a bias and an external magnetic field is shown in Fig. 7.5 (left). The green lines indicate the splitting of the top of the barriers. In Fig. 7.5 (right) the sample layer structure as it is grown by MBE is depicted.

A 0 T and 4 K I - V characteristic is shown in Fig. 7.6. At positive bias the first resonance with a peak to valley ratio of 2.4 is seen at 69 mV and its phonon replica at around 135 mV . The structure is quite asymmetric and we will concentrate on the current direction with the most pronounced resonance peak.

Perpendicular to the plane of the QW magnetic field dependence of the I - V peak at 4 K is shown in Fig. 7.7 (left). The magnetic field is swept from 0 to 13 T in 1 T steps. The dependence is relatively small for such a large magnetic field range. The size of the effect can be understood

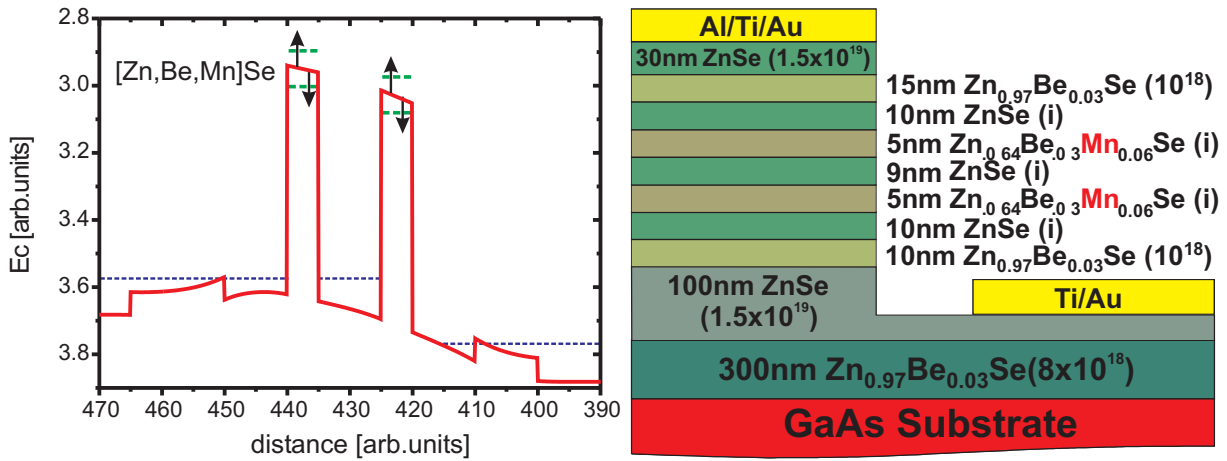


Figure 7.5: Right - schematic conduction band profile under bias and magnetic field. Left - the sample layer profile.

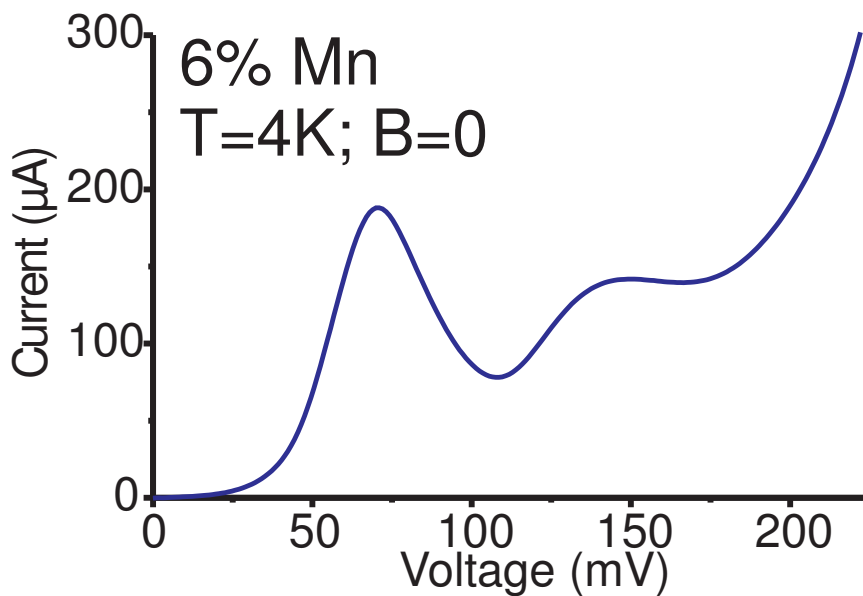


Figure 7.6: 0 T and 4 K I-V characteristic of the resonant tunneling structure with 6% Mn in both barriers.

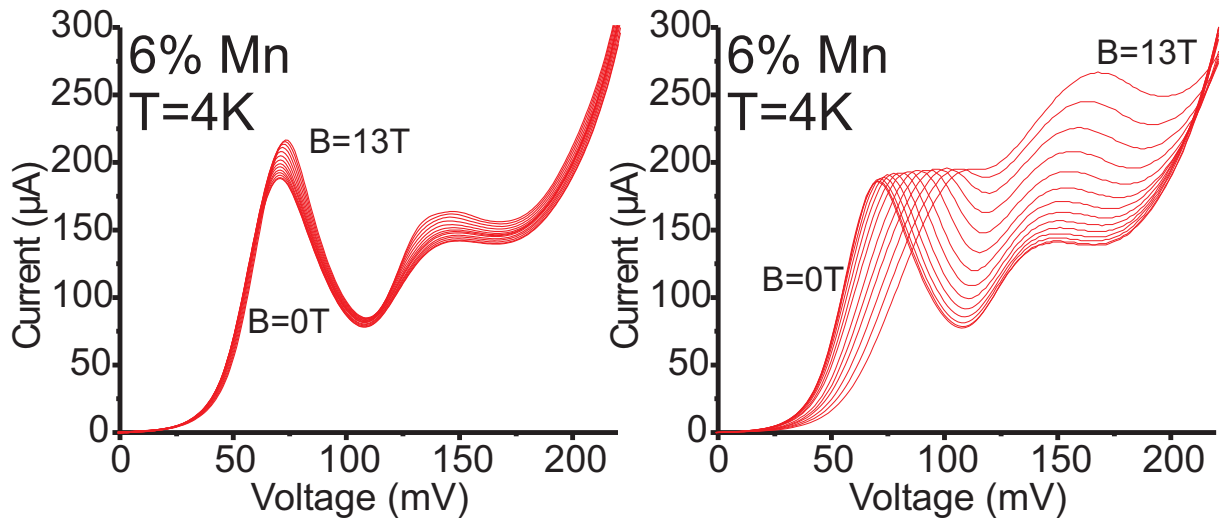


Figure 7.7: Left - perpendicular to the QW plane magnetic field dependence of the I-V characteristic for the sample with 6% Mn in the barriers. Right - in-plane of the QW magnetic field measurements for the same sample.

taking into account the facts that the giant Zeeman splitting is small compared to the barriers, which are around ~ 250 meV high, and the resonance peak is formed “basically“ at the bottom of the barriers. Moreover, in addition to the effect being small, its magnetic field behaviour is opposite to the one observed in the cases of the magnetic injector or quantum well. Namely, the magnetic field induced increase in the resonance current does not saturate, but instead the distance between I-V characteristics is increased at higher fields. Again, such dependence can be understood by assuming that the lower giant Zeeman split barrier starts to dominate the process exponentially. Under these conditions even a small change in the splitting at higher fields will produce great change in the I-V characteristic. This means that we could have much stronger spin polarization effects than seen on I-V, especially at high fields.

In Fig. 7.7 (right) an in-plane magnetic field measurement of the structure is presented. The effect is a manifestation of the Lorentz force modified k-vector of the tunneling electrons (see section 2.2.2).

Chapter 8

Spin resolved resonant tunneling in self-assembled quantum dots.

8.1 Self-Assembled II-V Quantum Dot as a Voltage-Controlled Spin-Filter.

Nanomagnetics has produced a series of fascinating and often unanticipated phenomena over the past few years. To name a few, molecular magnets exhibit quantum tunneling of the magnetisation [TLB⁺96], magnetic atoms on a surface exhibit giant magnetic anisotropies [GRV⁺03], and magnetic domain walls are being harnessed as data carriers [RBG⁺03]. Here, we report on another remarkable phenomenon: self-assembled quantum dots, fabricated from II-VI DMS that macroscopically exhibit paramagnetism, possess a remnant magnetisation at zero external field. This allows us to operate the dots as voltage controlled spin filters, capable of spin-selective carrier injection and detection in semiconductors. Such spin filter devices could provide a key element in the emergence of a full spintronics technology [WAB⁺01, Aws02, Ohn02]. We present the first experimental observation of such a device using an approach based on the incorporation of non-magnetic CdSe self-assembled quantum dots (SADs) in paramagnetic [Zn,Be,Mn]Se (see section 3.1.2).

We previously demonstrated a prototype of such a spin filter using a II-VI DMS-based resonant tunnelling diode [SGS⁺03]. However, while that device was tuned by a bias voltage, the spin filtering mechanism still requires an external magnetic field. Moreover, ferromagnetic III-V semiconductors like [Ga,Mn]As are not suitable for resonant tunneling devices due to the short mean free path of holes [MGJ⁺03]. Recent theoretical works [HGQ91, ERR01, FRB04] have suggested that spin selection may be achievable in II-VI DMS without any external magnetic field by creating localised carriers that might mediate a local ferromagnetic interaction between nearby Mn atoms.

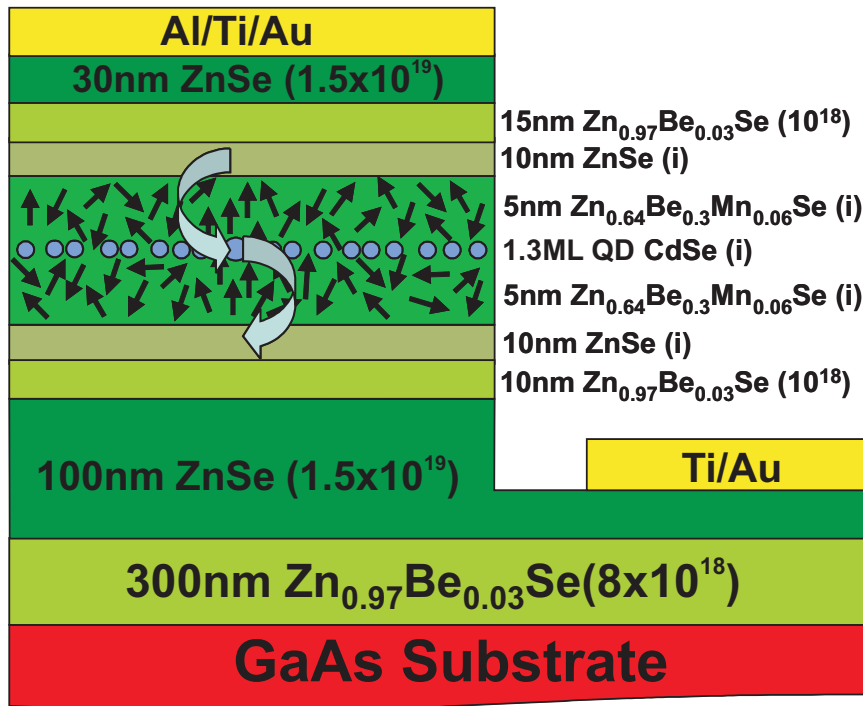


Figure 8.1: Full layer structure of the device and schematic of the transport mechanism. As electrons tunnel through the quantum dot, they mediate a local magnetic interaction between nearby Mn ions causing them to align ferromagnetically.

8.2 Sample and measurements details.

Our sample is an MBE-grown all-II-VI RTD structure consisting of a single 9 nm thick semi-magnetic $\text{Zn}_{0.64}\text{Be}_{0.3}\text{Mn}_{0.06}\text{Se}$ tunnel barrier, sandwiched between gradient doped $\text{Zn}_{0.97}\text{Be}_{0.03}\text{Se}$ injector and collector. Embedded within the barrier are 1.3 monolayers of CdSe. The lattice mismatch between the CdSe and the $\text{Zn}_{0.64}\text{Be}_{0.3}\text{Mn}_{0.06}\text{Se}$ induces a strain in the CdSe material, which is relaxed by the formation of isolated CdSe dots [MTB⁺01]. The full layer stack is given in Fig. 8.1. Standard optical lithography techniques were used to pattern the structure into $100\ \mu\text{m}$ square pillars and contacts were applied to the top and bottom ZnSe layers in order to perform transport measurements vertically through the layer stack. More details of the fabrication procedure are given in section 3.2.1. From the size of the pillars, and the typical density of the dots, one would expect some million dots within our device. However, despite this number, transport through similar III-V SAD-RTDs is usually dominated by only a few dots that come into resonance at lower bias voltages [HPM⁺01, VLP⁺00, TIM⁺98]. We, therefore, interpret the low bias transport through our sample as corresponding to electrons tunneling from the injector into a single quantum dot and out of the dot into the collector as schematically depicted in Fig. 8.1. Based on calculations of energy levels of strained quantum dots, we find several quantum dot levels populated by electrons at zero bias. Hence, the electrons tunnel through excited states of quantum dots containing a finite number of electrons.

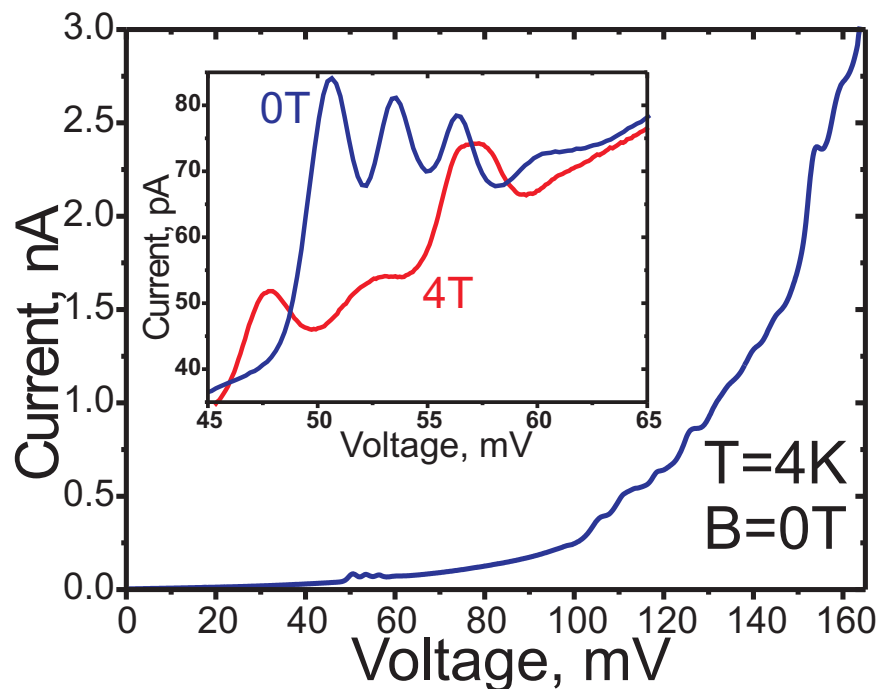


Figure 8.2: *Current-voltage characteristic of the device, with a high-resolution view of the first resonance feature in the inset, clearly showing a strong magnetic field dependence of the resonances.*

The experiments were carried out in a magnetocryostat and studied at temperatures as low as 1.3 K and in fields from 0 to 6 T. Fig. 8.2 shows a full current voltage curve up to a bias voltage of 170 mV. The first feature is observed at a bias of 55 mV, associated with the first dot coming into resonance. At a bias voltage above 100 mV, several resonances, due to the ensemble of dots, can also be observed. We will first focus on the low bias feature which is shown in the inset to the figure. These more detailed curves taken at 0 and 4 T clearly show that the feature actually has a complex structure, consisting of four distinct peaks, which evolve with the magnitude of the applied magnetic field. We verified that the evolution of the features does not appreciably depend on the direction of the magnetic field, indicating that the magnetic response of the system cannot be associated with artefacts such as two-dimensional states in the injector or wetting layer [SGS⁺03, HPM⁺01, VLP⁺00, TIM⁺98] and it must be a property of the dot or the barrier. We also verified that the sample does not exhibit any magnetic hysteresis.

8.3 Magnetic field evolution of the resonance peaks.

A better understanding of the evolution of the features with magnetic field can be obtained from Fig. 8.3. In Fig. 8.3(left), we plot the current through the device as a colour-scale surface with respect to a bias voltage and magnetic field. This proves two very important features of the data. Firstly, that as the magnetic field is increased, features split apart with a behaviour reminiscent

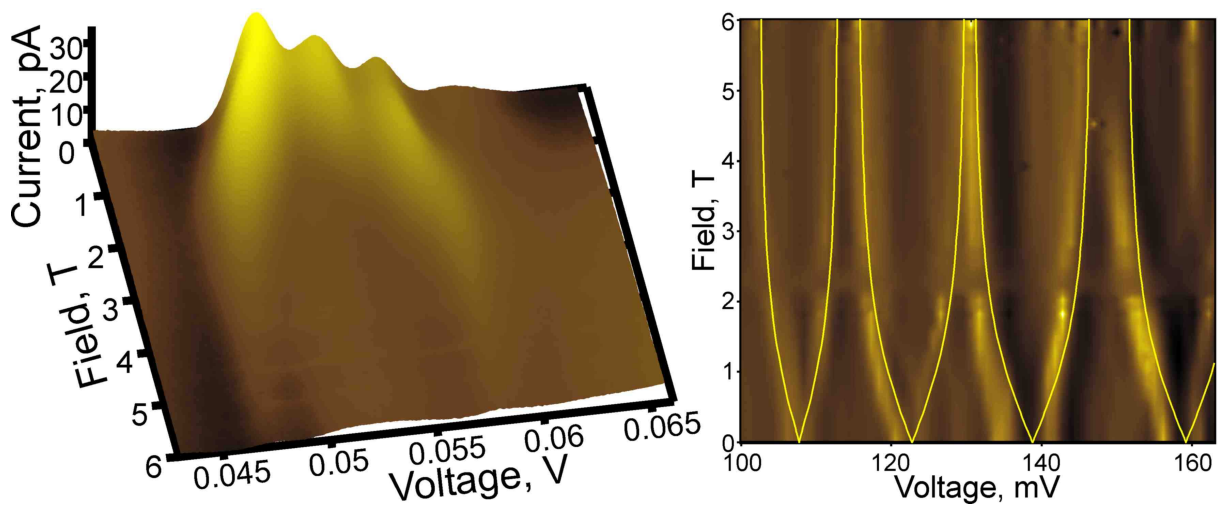


Figure 8.3: On the left - a surface plot of the current through the device as a function of a magnetic field and bias voltage in the region of the first resonance feature. On the right - a colour-scale image of the resonances as a function of a magnetic field and voltage for higher bias resonances. Since these higher resonances are weaker and on a significant background, the colour-scale on the right part is proportional to the voltage derivative of the current in order to better resolve the position of the resonances. In both cases, the data at higher magnetic fields clearly has Brillouin-like behaviour, as proved in the right figure, where Brillouin functions are plotted as lines. However, at fields below ~ 500 mT, the behaviour departs from a Brillouin function, with the splitting becoming constant and remaining finite even at zero magnetic field.

of the Brillouin function, and secondly, that the splitting remains finite in zero external magnetic field. The same behaviour can be seen for many of the higher bias resonances presented in Fig. 8.3(right). The first of these effects, that the levels should split following a Brillouin function, is not very surprising. It was previously observed in III-V devices that resonances split in a magnetic field following the Landé g factor of the material in the dots [TIM⁺98].

The main difference here is that in the present experiment it is the barrier, and not the dots, that are magnetic. Since the effect of the giant Zeeman splitting on the height of the barriers is negligible, the presence of Mn should have little effect on the barrier properties. However, given that electrons are not perfectly localised in the dots, but rather have wave functions which extend into the barrier, it is not surprising that the quantum levels in the dots spin-split following the magnetisation of the Mn in the barriers, yielding results reminiscent of those previously observed [SGS⁺03] in the case of tunneling through a dilute magnetic quantum well.

The observation that the splitting remains finite at $B = 0$ T is however more surprising since there is a priori nothing ferromagnetic in the sample. This observation can be understood by considering the effect of interactions between electrons in the dot and the Mn atoms in the vicinity of the dot.

8.4 Understanding the effect of an external magnetic field.

Electrons populate quantum dot levels according to the Pauli exclusion principle, and Hunds rules [HK03] whenever there is orbital degeneracy. For a parabolic dot, the total electron spin follows the sequence $S = \{1/2, 0, 1/2, 1, 1/2, 0, 1/2, 1, 3/2, \dots\}$ with increasing electron numbers. Hence, for almost all electron numbers, the total spin of the dot is finite. The interaction of this total net spin with the spin of Mn ions induces an effective ferromagnetic Mn-Mn interaction. This can be seen by considering the total Hamiltonian of the electronic and Mn system [HGQ91, ERR01, BIG97, HME⁺00]:

$$H = H_e + g^* \mu_B \vec{B} \cdot \sum_i \vec{S}_i - J_C \sum_{\vec{R}, i} \vec{M}_{\vec{R}} \cdot \vec{S}_i \delta(\vec{r}_i - \vec{R}) + \sum_{\vec{R}} g_{Mn} \mu_B \vec{B} \cdot \vec{M}_{\vec{R}} + \frac{1}{2} \sum_{\vec{R}, \vec{R}'} J_{\vec{R}, \vec{R}'} \vec{M}_{\vec{R}} \cdot \vec{M}_{\vec{R}'}$$

Here $\vec{M}_{\vec{R}}$ is the spin of Mn ions ($M=5/2$) at position \vec{R} , S_i is the spin of the i -th electron ($S=1/2$). J_c is the sp-d exchange constant between the conduction electrons and the d-electrons of the Mn shell and $J_{RR'}$ is the anti-ferromagnetic Mn-Mn interaction. The first term is the spin independent Hamiltonian of electrons confined to a quantum dot in a magnetic field, and interacting via a pair-wise potential. The full interaction between electron spins and Mn ions in the barrier is an extremely complicated issue. We restrict ourselves here to a demonstration that the electron spin is capable of compensating the anti-ferromagnetic interaction among Mn ions and lead to their ferromagnetic arrangement. We consider only a single electron in the ground state and in the absence of external magnetic field, leaving the problem of interacting many-electron dots for future analyses. The effective spin Hamiltonian now reads:

$$H = E_0 - J_C \sum_{\vec{R}} |\Phi(R)|^2 \vec{M}_{\vec{R}} \cdot \vec{S} + \frac{1}{2} \sum_{\vec{R}, \vec{R}'} J_{\vec{R}, \vec{R}'} \vec{M}_{\vec{R}} \cdot \vec{M}_{\vec{R}'} \quad (8.1)$$

where E_0 is the electron energy and $|\Phi(R)|^2$ is the probability of finding an electron at the position \vec{R} of a Mn ion. Even for such a simplified Hamiltonian the number of configurations is very large in the number of Mn ions. The physics of Mn-Mn interactions mediated by electron spin can however be understood by examining an exactly solvable problem of two anti-ferromagnetically coupled Mn ions. The energy spectrum of the coupled Mn-spin system is characterised by the total spin $J=M\pm 1/2$ where M is the total Mn spin and the $\pm 1/2$ corresponds to the direction of the electron spin. The evolution of the energy of the system as a function of the total Mn spin depends on the direction of the electron spin in the following way:

$$E(M, +) = -\left(\frac{\hat{J}_C}{2}\right)M + \left(\frac{J_{NN'}}{2}\right)[M(M+1) - \frac{35}{2}]$$

$$E(M, -) = \left(\frac{\hat{J}_C}{2}\right)(M+1) + \left(\frac{J_{NN'}}{2}\right)[M(M+1) - \frac{35}{2}]$$

as shown in Fig. 8.4(left). In the absence of coupling to the electron spin ($J_c = 0$), it is obvious that the minimum energy state for either electron spin corresponds to the total Mn spin $M=0$, i.e. an antiferromagnetic arrangement. However, as shown in Fig. 8.4(left), with coupling to the electron spin, the $E(M, +)$ ground state of the combined system has a finite total Mn spin $M^* = (\frac{\hat{J}_C}{J_{NN'}} - 1)/2$. To estimate the value of M^* we approximate our quantum dot by a spherical CdSe dot with radius $R=4$ nm and a barrier potential of 1 eV estimated from strain and the Bir-Pikus Hamiltonian. The effective electron-Mn exchange interaction for Mn ions on the surface of the sphere is then given by $\hat{J}_C = J_C |\Phi(R)|^2 = 4.5 \mu\text{eV}$. For a typical Mn separation in the barrier of $R_{12} = 1.2$ nm, we estimate the antiferromagnetic interaction strength $J_{12} = 1 \mu\text{eV}$. Hence for our model system we find $M^* = 2$ and the coupling to electron spin aligns spins of nearest neighbouring Mn ions. Independent mean field calculations involving tens of Mn ions randomly distributed in the barrier around a spherical or disk shaped quantum dots confirm the existence of ferromagnetic ordering of Mn ions in the vicinity of quantum dots [FRB04]. In Fig. 8.4(right), we show the calculated averaged Mn and electron spin magnetisation as a function of temperature for Mn ions localised in the barrier surrounding a spherical CdSe quantum dot with radius of 4 nm and Mn concentration of 4%. We find the existence of the magnetic polaron, with the Mn magnetisation decaying as one moves away from the quantum dot. These findings are in agreement with previous calculations of magnetic polarons [HGQ91, ERR01, FRB04], and for reasonable parameters for our system shows that the presence of electrons in the dot will mediate a local ferromagnetic interaction between Mn atoms near this dot.

The interpretation of our experimental observations is therefore clear. Electrons localised in the dot mediate a local ferromagnetic interaction which causes a finite spin splitting even in the absence of an external applied field. Our experiment is therefore tantamount to measuring transport through a single magnetic polaron. The local interaction has a strength corresponding to an effective field of the order of some hundreds of mT, and can be randomly oriented. When an external magnetic field is then applied, the ferromagnetic order will first rotate towards the direction of the applied field, but this will have no effect on the transport, which explains why in the experimental data, the resonance positions are independent of the magnetic field for fields below ~ 500 mT. However, as the magnetic field is further increased, it will start to dominate and the spin splitting will grow following the normal paramagnetic interaction of the dilute Mn system [SGS⁺03]. A question remains as to why the zero magnetic field splitting is observed here while it was not seen in the optical measurements of Ref. [HME⁺00, MGN⁺04]. This however can be understood by the fact that once current begins flowing through the dot, a feedback mechanism sets in where spin polarization of the current enhances the polarization of Mn spins which in turn enhances the polarization of the current [HGQ91, ERR01]. This

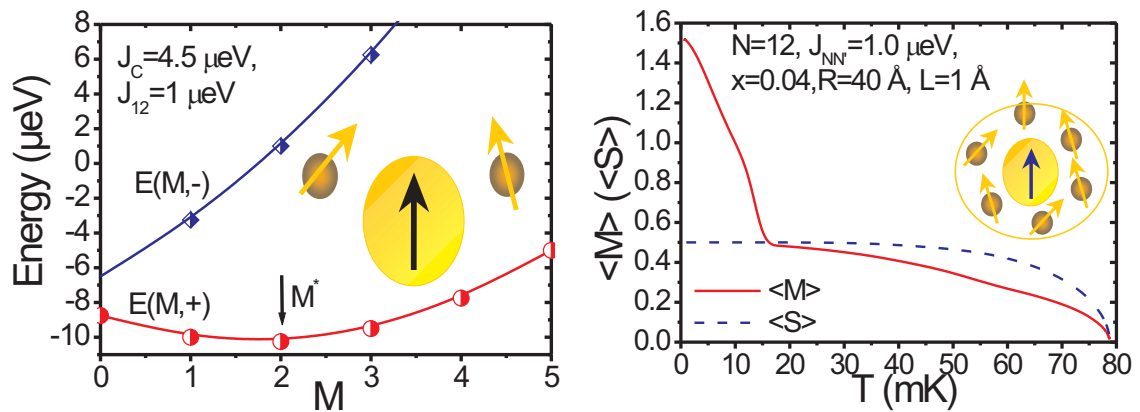


Figure 8.4: On the left - the energy levels $E[+,M]$, $E[-,M]$ for two different electron spin orientations as a function of total spin of two Mn ions M localised on a surface of spherical quantum dot and on the right - average magnetisation as a function of temperature of Mn ions randomly distributed on a surface of spherical quantum dot.

dynamical effect also explains why spin polarization is observed at much a higher temperature than the predicted temperature dependence of magneto-polaron of Fig. 8.4(right).

In conclusion, we have shown that electrons in a quantum dot can mediate a local ferromagnetic interaction in a surrounding dilute Mn system and that this leads to a finite energy splitting of spin levels in the dot in the absence of an external magnetic field. Coupled with the resonant tunneling scheme which allows the bias controlled selection of which dot level is used in tunneling, our results open up exciting new possibilities of a voltage controlled spin filter, which can operate in the absence of any external magnetic field, without relying on an inherent ferromagnetism of the component materials.

Summary

Spintronics is a rapidly growing field in physics and presently attracts much attention. Spintronics aims to exploit the spin properties of the electron instead of, or in addition to, charge degrees of freedom, for the development of a novel generation of devices.

In this work we investigate magnetic resonant tunneling diode (RTD) structures for spin manipulation. All-II-VI semiconductor RTD structures based on [Zn,Be]Se are grown by MBE. We observe a strong, magnetic field induced, splitting of the resonance peaks in the I-V characteristics of RTDs with [Zn,Mn]Se diluted magnetic semiconductors (DMS) quantum well (QW). The splitting saturates at high fields and has strong temperature dependence. A phonon replica of the resonance is also observed and has similar behaviour to the peak.

We develop a model based on the giant Zeeman splitting of the spin levels in the DMS quantum well in order to explain the magnetic field induced behaviour of the resonance. First, we extract the series contact resistance of the RTD from the measured I-V curve at zero magnetic field [MLSE94, LMS⁺94]. Then we assume that each of the two spin split levels have the same conductance and that each, therefore, carries half of the current in the device. We also assume that the conductivity of each level as a function of applied voltage, and in the presence of a magnetic field can be given by a simple translation of the zero field curve by a voltage corresponding to the energy shift of the pertinent spin level in the well. After translation, we add the conductivity contributions of both the spin-up and spin-down channels, and reinsert the series resistance. By comparing this modelled I-V curve with the experimental curve we are able to determine the optimal value of series' resistance and the voltage splitting of the levels. The modelled I-V curves compare very well with the experimental data. Moreover, the series resistance is magnetic field independent. We find a remarkable agreement between the magnetic field dependence of the experimental values and the modified Brillouin function [GPF79] describing giant Zeeman splitting. The agreement is valid at all temperatures and Mn concentrations. In order to correctly fit the amplitude to the Brillouin function, the measured voltage splitting must be divided by a lever arm of ~ 2.1 . This value is confirmed by the voltage distance between the resonance and its LO phonon replica.

At magnetic fields higher than 6 T, the giant Zeeman splitting is basically saturated and no longer has a strong influence on the position nor the shape of the resonances as B is further increased. On the other hand, a very strong effect is still observable at magnetic fields above

6 T. The high voltage resonance decreases in amplitude and the low voltage one increases. This is explained as an effect of spin polarized current in the injector created by a regular Zeeman splitting.

In the case of giant Zeeman split levels in the QW, we expect a current spin polarization in the injector to decrease the amplitude of the minority peak and increase that of the majority one. The majority current spin polarization is generated by the lower (in energy) regular Zeeman split states of the conduction band of the injector. The regular Zeeman splitting in ZnSe has the same sign as the giant Zeeman term for the [Zn,Mn]Se conduction band. This means that the majority current spin polarization corresponds to the lower giant Zeeman split level in the QW. The peak at higher bias (minority spin polarization) will thus decrease when the spin polarization of the current in the injector is increased. The effect of the current spin polarization is mainly observed at high magnetic fields because the regular Zeeman splitting at intermediate fields is relatively small compared to the estimated injector Fermi energy.

A study of the dependence of the I-V characteristic of the RTD on the regular Zeeman splitting in the injector was performed by measuring I-V curves at various temperatures with magnetic field chosen to keep the giant Zeeman splitting constant. This clearly illustrates that at lower regular Zeeman splitting, the peak ratio returns to the values expected for non-polarized injector electrons. On the other hand, I-V characteristics measured at different temperatures and constant (high) 16 T magnetic field, at which the giant Zeeman splitting has a weak temperature dependence and the regular Zeeman splitting is constant, show that at higher temperatures the peak ratio changes its value to that observed at lower magnetic fields ≤ 6 T. This is caused by the temperature induced decrease in spin polarization of the current in the injector. By comparing the values of the regular Zeeman spin splitting of the conduction band in the injector with the value of temperature broadening described by kT , one can see already at 12 K that kT is bigger than the Zeeman splitting, causing the reduced spin polarization seen in our measurement.

After having understood the influence that a spin splitting in the magnetic QW has on the transport properties of RTD, we now turn to the influence of other parts of the structure being magnetic. The resonance peak of an RTD with a $\text{Zn}_{0.94}\text{Mn}_{0.06}\text{Se}$ DMS injector layer, used to inject spin polarized electrons into the diode, shows a strong magnetic field dependence. The peak shifts to higher voltages and strongly *increases* in amplitude as a magnetic field is applied. The strongest dependence of the peak amplitude and position in the magnetic field is observed at lower fields, with the behaviour saturating before 10 T. The behaviour is therefore consistent with the Brillouin-like behaviour expected from the giant Zeeman splitting of the injector. The phonon replica causes a higher energy echo of the QW state and the corresponding peak simply follows the magnetic field dependence of the main resonance. An increase in temperature has a similar effect on the I-V curves as a lowering in the magnetic field would. Indeed, the only effect of temperature is to rescale the effect of the magnetic field on the Zeeman splitting in the injector exactly as would be expected from the argument of the Brillouin function scales as $B/(T + T_{\text{eff}})$. The slight shift of the peak to higher bias with increasing magnetic field is fairly intuitive and can be understood as a higher bias being required to bring the giant Zeeman split bottom of the majority spin conduction band (dominating the peak as magnetic field increases) in alignment with the QW level. The strong increase in the current amplitude is also related

to the change of the conduction band energy with magnetic field B . The results we obtain are reminiscent of Ref. [CW92], where the band alignment was changed by varying the In content of a GaInAs emitter in a III-V RTD. In our case, the increase is exclusively due to the giant spin splitting in the injector. Thus, the current increase can be tuned with a magnetic field without changing the sample parameters.

Another potentially interesting sample design using diluted magnetic material in the barriers of RTD devices, which might be expected to give rise to spin selection in the structure, did not show strong magnetic field dependence. Moreover, in addition to the effect being small, its magnetic field induced increase in the resonance current does not saturate, the distance between I-V characteristics is increased at higher fields. Although, such dependence can be qualitatively understood, more detailed analysis is required in order to correctly explain the change in the I-V characteristic.

In order to design real applications from the investigated structures it will be necessary to combine multiple devices. As a first step we analysed a non-local measurement scheme for a double RTD with magnetic QWs for current spin polarization and detection. As a result of current spin polarization created by one of the RTDs influencing the potential drop over the other, the resonant peaks in the I-V characteristic shift. In the case of spin polarization of the same sign as the lower energy peak, the peak will shift to a lower bias and the higher energy peak will shift to a higher bias. The separation between the peaks will thus increase. When the collector spin polarization corresponds to the spin polarization of the higher resonance separation between the peaks will decrease.

Even though voltage *controlled* spin selection and detection are demonstrated in the magnetic RTDs, an external magnetic field is still needed to achieve spin selection or detection. Surprisingly, the field is not needed in the case of a spin resolved resonant tunneling in self-assembled CdSe quantum dots embedded (instead of the QW) in a semi-magnetic $\text{Zn}_{0.64}\text{Be}_{0.3}\text{Mn}_{0.06}\text{Se}$ tunnel barrier of a II-VI RTD. Despite the fact that there are many dots in the pillar structure, resonance peaks originating from the levels of a single quantum dot are known to be observed at low bias. The first separate low bias feature in the I-V curve of the RTD is associated with a single dot levels go into resonance. At higher bias voltage, several resonances due to the ensemble of dots can also be observed. Firstly, we find that as the magnetic field is increased, features split apart with a behaviour reminiscent of the Brillouin function, and secondly, that the splitting remains finite in zero external magnetic field. Given that electrons are not perfectly localised in the dots, but rather have wave functions which extend into the barrier, it is not surprising that the quantum levels in the dots spin-split following the magnetisation of the Mn in the barriers as for the case of the magnetic QW sample. The observation that the splitting remains finite at $B = 0$ T is however more surprising since there is a priori nothing ferromagnetic in the sample. This observation is explained by considering the effect of interactions between electrons in the dot and the Mn atoms in the vicinity of the dot, which results in a local carrier mediated ferromagnetic interaction between Mn ions in the vicinity of the dot.

In this work we demonstrate the usefulness of magnetic resonant tunneling devices for spin detection and manipulation. Spin resolved transport has a strong influence on the magnetic RTD

I-V characteristic, which could potentially be exploited in real applications. Spin selection and detection in RTDs with magnetic QW, spin injection in an RTD with magnetic injector, spin resonant transport in quantum dots (even at zero external magnetic field) and the first steps in combining the components have been achieved.

Zusammenfassung

Die Spintronik ist ein schnell expandierendes Feld der Physik und seit einiger Zeit wird ihr große Aufmerksamkeit gewidmet. Hierbei wird versucht, anstatt bzw. zusätzlich zur Ladung des Elektrons seinen Spin auszunutzen, um damit die Entwicklung einer neuen Generation von Bauelementen zu ermöglichen.

In dieser Arbeit werden magnetische resonante Tunneldioden (RTD) hinsichtlich ihrer Eignung zur Spin-Manipulation untersucht. [Zn, Be]Se basierende II-VI RTD-Strukturen wurden mittels Molekularstrahlepitaxie (MBE) gewachsen. Man beobachtet eine starke, vom Magnetfeld induzierte Aufspaltung der Resonanz in der U-I Kennlinie derjenigen RTDs, die über einen Quantentrog (QW) aus [Zn, Mn]Se verdünnt magnetischen Halbleiter (DMS) verfügen. Diese Aufspaltung hat eine starke Temperaturabhängigkeit und erreicht bei hohen Feldern eine Sättigung. Eine Phononen-Replika der Resonanz wird ebenfalls beobachtet und hat ähnliche Eigenschaften wie die Resonanz selbst.

Es wird ein Modell entwickelt, welches auf der Giant-Zeeman-Aufspaltung der Spin-Aufgespalteten Niveaus des DMS-Quantentrogs basiert, um das magnetfeldabhängige Verhalten der Resonanz zu erklären. Dafür wird zuerst der Reihenwiderstand der RTD von der gemessenen U-I Kennlinie ohne angelegtes Magnetfeld abgeleitet [MLSE94, LMS⁺94]. Dann wird angenommen, daß jedes der beiden Spinniveaus dieselbe Leitfähigkeit aufweist und demzufolge auf beide die Hälfte des Stroms entfällt. Man nimmt außerdem die Leitfähigkeit jedes Niveaus als Funktion der Spannung an und passt in Anwesenheit eines magnetischen Feldes die Nullfeldfunktion durch die entsprechende Energieverschiebung der Niveaus an. Nach dieser Anpassung können beide Leitfähigkeiten addiert und der Serienwiderstand wieder einbezogen werden. Durch einen Vergleich der simulierten U-I Kennlinie mit der Experimentellen ist es möglich, den optimalen Serienwiderstand und die Aufspaltung des Niveaus zu bestimmen. Die Simulation stimmt gut mit experimentellen Daten überein. Der Serienwiderstand ist unabhängig vom Magnetfeld. Es ergibt sich eine auffällige Übereinstimmung zwischen der Magnetfeldabhängigkeit der experimentellen Daten und der modifizierten Brillouinfunktion [GPF79], welche die Giant-Zeeman-Aufspaltung beschreibt. Diese Übereinstimmung ist bei allen Temperaturen und Mn-Konzentrationen gültig. Um die Amplitude der Brillouinfunktion anzupassen muß ein Umrechnungsfaktor für die gemessene Spannung von etwa 2.1 eingeführt werden. Dieser Wert wird durch den Spannungsabstand zwischen der Resonanz und ihrer LO-Phononen Replika bestätigt.

Ab Magnetfeldern von etwa 6T ist die Giant-Zeeman-Aufspaltung gesättigt und hat keinen starken Einfluß mehr auf die Position oder die Kontur der Resonanz bei weiter steigender Magnetfeldstärke. Andererseits ist ein sehr starker Effekt oberhalb von 6T zu beobachten. Die Amplitude der zweiten Resonanz nimmt ab, während die Erste zunimmt. Dies kann als ein Effekt des spinpolarisierten Stroms im Injektor erklärt werden, der durch die normale Zeeman-Aufspaltung polarisiert wird.

Im Falle von durch den Giant-Zeeman-Effekt aufgespalteten Niveaus im Quantentrog ist von einem spinpolarisierten Injektorstrom zu erwarten, daß die Amplitude der Minoritätsladungsträgerresonanz abnimmt und die der Majoritätsladungsträger zunimmt. Die Spinmajorität im spinpolarisierten Strom wird von dem energetisch niedrigeren Zustand der normalen Zeeman-Aufspaltung des Injektorleitungsbandes gebildet. Die normale Zeeman-Aufspaltung in ZnSe hat das selbe Vorzeichen wie die Giant-Zeeman-Aufspaltung im Leitungsband von [Zn,Mn]Se. Dadurch entspricht die Spinmajorität des spinpolarisierten Stroms dem des niedrigeren Niveaus der Giant-Zeeman-Aufspaltung im Quantentrog. Die Resonanz bei höherer Spannung (Minoritätsspinpolarisation) wird daher abnehmen, wenn sich die Spinpolarisation des Stroms im Injektor erhöht. Der Effekt der Stromspinpolarisation wird erst bei hohen Magnetfeldern beobachtet, da die normale Zeeman-Aufspaltung bei geringeren Feldstärken relativ klein im Vergleich zur erwarteten Fermi-Energie im Injektor ist.

Die Abhängigkeit der U-I Kennlinie der RTD von der normalen Zeeman-Aufspaltung im Injektor wurde ermittelt, indem U-I Kennlinien bei verschiedenen Temperaturen im Magnetfeld gemessen wurden, wobei das Magnetfeld so gewählt wurde, daß die Giant-Zeeman-Aufspaltung konstant ist. Damit läßt sich zeigen, daß für niedrigere normale Zeeman-Aufspaltung das Verhältnis der Resonanzen auf den Wert für einen unpolarisierten Injektorstrom zurückkehrt. Messungen bei unterschiedlichen Temperaturen und bei hohem, konstantem Magnetfeld (16T), für welches die Giant-Zeeman-Aufspaltung nur schwach und die normale Zeeman-Aufspaltung gar nicht temperaturabhängig ist, zeigen, daß bei höheren Temperaturen das Verhältnis der Resonanzen wieder demjenigen von niedrigen Magnetfeldern ≤ 6 T entspricht. Dies wird durch den Rückgang der Stromspinpolarisation im Injektor durch die Temperaturerhöhung verursacht. Der Vergleich der Werte der normalen Zeeman-Aufspaltung des Injektorleitungsbandes mit der thermischen Verbreiterung zeigt, daß bereits bei 12K kT größer als die Zeeman-Aufspaltung ist, was zur beobachteten Reduktion der Spin-Polarisation führt.

Nachdem der Einfluß der Spinaufspaltung im magnetischen Quantentrog auf die Transporteigenschaften der RTD verstanden ist, wird nun der Einfluß des Einbaus magnetischer Materialien an anderen Stellen in der Struktur untersucht. Die Resonanz einer RTD mit $\text{Zn}_{0.94}\text{Mn}_{0.06}\text{Se}$ DMS als Injektor, um spinpolarisierte Elektronen zu injizieren, zeigt eine starke Magnetfeldabhängigkeit. Im Magnetfeld verschiebt sich die Resonanz zu höheren Spannungen und ihre Amplitude *vergrößert* sich stark. Die stärkste Abhängigkeit der Amplitude zeigt sich bei niedrigen Feldern. Außerdem zeigt sich eine Sättigung bei 10T, womit das Verhalten konsistent ist mit einem Brillouinartigen Verhalten, welches man von der Giant-Zeeman-Aufspaltung im Injektor erwartet. Die Phononenreplika verursacht ein Echo des QW Zustands bei höherer Energie und das zugehörige Maximum folgt der Magnetfeldabhängigkeit des Hauptmaximums. Eine Temperaturzunahme hat einen ähnlichen Effekt wie eine Magnetfeldab-

nahme. Tatsächlich liegt dieser Temperatureffekt nur in der Anpassung des Magnetfeldeffekts der Zeeman-Aufspaltung im Injektor, genau, wie man es von der $B/(T + T_{\text{eff}})$ Abhängigkeit aus der Brillouinfunktion erwartet. Die Verschiebung des Maximums zu höheren Spannungen mit größerem Magnetfeld kann intuitiv verstanden werden, da eine größere Spannungsdifferenz zwischen dem unteren Niveau des Leitungsbandes, welches das Majoritätsspinniveau ist und somit die Resonanz bei steigendem Magnetfeld dominiert, und dem QW-Zustand liegt. Die starke Zunahme in der Stromamplitude hängt auch mit der Änderung der Leitungsbandenergie durch das Magnetfeld zusammen. Diese Resultate sind vergleichbar mit Ergebnissen an III-V RTDs deren Bandverlauf durch veränderten In-Gehalt im GaInAs-Emitter verändert wurde [CW92]. In unserem Fall ist die Zunahme ausschließlich auf die große Spinaufspaltung im Injektor zurückzuführen. Daher kann die Stromzunahme mit einem Magnetfeld beeinflusst werden, ohne die Probenparameter zu verändern.

Eine andere potentiell interessante Probenstruktur mit DMS in den Barrieren der RTD, was zu einer Spinselektion führen sollte, zeigte keine starke Magnetfeldabhängigkeit. Zudem sättigt die magnetfeldinduzierte Stromerhöhung nicht, sondern die Differenz der U-I Kennlinien erhöht sich mit steigenden Magnetfeldern. Obwohl diese Abhängigkeit qualitativ verstanden werden kann, sind weitere Untersuchungen notwendig, um dieses Ergebnis korrekt zu erklären.

Für die Anwendung solcher Strukturen in Bauelementen, wird es notwendig sein, mehrere RTDs zu kombinieren. In einem ersten Schritt wird ein nicht-lokales Messungsschema einer Doppel-RTD mit magnetischen QWs zur Spinpolarisation und -detektion analysiert. Als Resultat der von der ersten RTD erzeugten Spinpolarisation, die den Spannungsabfall über der Zweiten beeinflusst, verschieben sich die Resonanzen dieser RTD. Im Falle einer Spinpolarisation desselben Vorzeichens wie des niederenergetischen Maximums verschiebt sich dieses zu niedrigeren Spannungen und das höherenergetische Maximum verschiebt sich zu höheren Spannungen. Daher erhöht sich die Aufspaltung der Maxima. Im umgekehrten Fall verringert sich die Aufspaltung.

Obwohl *spannungskontrollierte* Spinselektion und -detektion in magnetischen RTDs gezeigt werden, wird immer noch ein externes Magnetfeld benötigt. Überraschenderweise wird kein Feld bei selbstorganisierten CdSe Quantenpunkten (anstatt des Quantentrog) benötigt, die in einer semimagnetischen $\text{Zn}_{0.64}\text{Be}_{0.3}\text{Mn}_{0.06}\text{Se}$ Tunnelbarriere einer II-VI RTD eingeschlossen sind. Trotz der Tatsache, daß viele Punkte in einer Struktur sind, sind die Resonanzmaxima einzelner Quantenpunkte bekanntermaßen bei niedrigen Spannungen zu beobachten. Die erste isolierte Struktur bei niedriger Spannung in der U-I Kennlinie der RTD kann mit einem einzelnen, resonierenden Quantenpunkt in Verbindung gebracht werden. Bei höheren Spannungen können weitere Resonanzen der restlichen Punkte beobachtet werden. Es wird ein brillouinartiges Auseinanderdriften der Spitzen mit zunehmenden Magnetfeld beobachtet, allerdings bleiben die Maxima selbst ohne externes Feld aufgespalten. Unter der Annahme, daß die Elektronen nicht perfekt in den Quantenpunkten lokalisiert sind, sondern ihre Wellenfunktion in die Barriere reicht, dann ist es nicht erstaunlich, daß die Quantenniveaus in den Punkten vergleichbar mit dem Fall des magnetischen Quantentrog mit dem Magnetfeld aufspalten. Wesentlich überraschender ist die Tatsache, daß die Aufspaltung auch bei $B = 0$ T bestehen bleibt, da a priori kein Ferromagnet in der Probe ist. Dies lässt sich durch die Interaktion

zwischen den Elektronen im Quantenpunkt und den Mn-Atomen in der Umgebung des Punktes erklären, welche zu einer lokalen durch die Ladungsträger vermittelten ferromagnetischen Wechselwirkung zwischen den Mn-Atomen in der Nachbarschaft des Quantenpunkts führt.

In dieser Arbeit wird die Nützlichkeit von magnetischen resonanten Tunnelnioden zur Detektion und Manipulation von Spins gezeigt. Der spinabhängige Transport hat einen starken Einfluß auf die U-I Kennlinie der magnetischen RTDs, welche das Potential für echte Anwendungen besitzen. Die Selektion und Detektion von Spin in RTDs mit magnetischem Quantentrog, Spininjektion in eine RTD mit magnetischem Injektor, spinresonanter Transport in Quantenpunkten (sogar ohne externes Magnetfeld) und die ersten Schritte zur Kombination dieser Komponenten wurden gezeigt.

Bibliography

- [AHD84] M. Ya. Azbel, A. Hartstein, and D. P. DiVincenzo. T dependence of the conductance in quasi one-dimensional systems. *Phys. Rev. Lett.*, 52:1641, 1984.
- [AMR⁺88] S. Ben Amor, K. P. Martin, J. J. L. Rascol, R. J. Higgins, A. Torabi, H. M. Harris, and C. J. Summers. Transverse magnetic field dependence of the current-voltage characteristics of double-barrier quantum well tunneling structures. *Appl. Phys. Lett.*, 53:2540–2542, 1988.
- [ARM⁺90] S. Ben Amor, J. J. L. Rascol, K. P. Martin, R. J. Higgins, R. C. Potter, and H. Hier. Transverse magnetic field studies in $Al_{1-y}In_yAs/Ga_{1-x}In_xAs$ quantum-well tunneling structures. *Phys. Rev. B*, 41:7860–7863, 1990.
- [ASDR88] Akhilesh K. Arora, E. K. Suh, U. Debska, and A. K. Ramdas. Raman-scattering study of the high-pressure phase transition in $Zn_{1-x}Mn_xSe$. *Phys. Rev. B*, 37:2927–2932, 1988.
- [Aws02] *Semiconductor Spintronics and Quantum Computation*. Springer, 2002.
- [BB98] L. S. Braginskii and E. M. Baskin. Inelastic resonant tunneling. *Physics of the solid state*, 40:1051, 1998.
- [BB99] Ya. M. Blanter and M. Büttiker. Transition from sub-poissonian to super-poissonian shot noise in resonant quantum wells. *Phys. Rev. B*, 59:10217–10226, 1999.
- [BBF⁺88] M. N. Baibich, J. M. Broto, A. Fert, F. Nguyen Van Dau, F. Petroff, P. Eitenne, G. Creuzet, A. Friederich, and J. Chazelas. Giant magnetoresistance of $(001)Fe/(001)Cr$ magnetic superlattices. *Phys. Rev. Lett.*, 61:2472–2475, 1988.
- [BBK⁺86] R. B. Bylsma, W. M. Becker, J. Kossut, U. Debska, and D. Yoder–Short. Dependence of energy gap on x and t in $Zn_{1-x}Mn_xSe$: The role of exchange interaction. *Phys. Rev. B*, 33:8207–8215, 1986.
- [BKR⁺03] F. A. Baron, A. A. Kiselev, H. D. Robinson, K. W. Kim, K. L. Wang, and E. Yablonovitch. Manipulating the l-valley electron g factor in si-ge heterostructures. *Phys. Rev. B*, 68:195306, 2003.

- [BIG97] A.K. Bhattacharjee and C. Benoit à la Guillaume. Exciton magnetic polaron in semimagnetic semiconductor nanocrystals. *Phys. Rev. B*, 55:10613–10620, 1997.
- [BR84] Y. A. Bychkov and E. I. Rashba. *J. Phys. C*, 17:6039, 1984.
- [But88] M. Buttiker. Coherent and sequential tunneling in series barriers. *IBM. J. Res. DEVELOP.*, 32(1), 1988.
- [BW36] G. Breit and E. Wigner. Capture of slow neutrons. *Phys. Rev.*, 49:519, 1936.
- [CC76] J. R. Chelikowsky and M. L. Cohen. Nonlocal pseudopotential calculations for the electronic structure of eleven diamond and zinc-blende semiconductors. *Phys. Rev. B*, 14:556, 1976.
- [CET74] L. L. Chang, L. Esaki, and R. Tsu. Resonant tunneling in semiconductor double barriers. *Appl. Phys. Lett.*, 24:593, 1974.
- [CTF00] C. Chauvet, E. Tournié, and J.-P. Faurie. Nature of the band gap in $Zn_{1-x}Be_xSe$ alloys. *Phys. Rev. B*, 61:5332, 2000.
- [CW92] Y. W. Choi and C. R. Wie. Increased peak current in alas/gaas resonant tunneling structures with $GaInAs$ emitter spacer. *Journal of Applied Physics*, 71(4):1853–1859, 1992.
- [DD90] Supriyo Datta and Biswajit Das. Electronic analog of the electro-optic modulator. *Appl. Phys. Lett.*, 56(7):665–667, 1990.
- [dGMvE83] R. A. de Groot, F. M. Mueller, P. G. van Engen, and K. H. J. Buschow. New class of materials: Half-metallic ferromagnets. *Phys. Rev. Lett.*, 50:2024–2027, 1983.
- [DiV99] David P. DiVincenzo. Quantum computing and single-qubit measurements using the spin-filter effect (invited). *J. Appl. Phys.*, 85:4785–4787, 1999.
- [DLR⁺04] P. Van Dorpe, Z. Liu, W. Van Roy, V. F. Motsnyi, M. Sawicki, G. Borghs, and J. De Boeck. Very high spin polarization in $GaAs$ by injection from a $(Ga, Mn)As$ zener diode. *Appl. Phys. Lett.*, 84:3495–3497, 2004.
- [DNPK87] R A Davies, D J Newson, T G Powell, and M J Kelly. Magnetotransport in semiconductor superlattices. *Semicond. Sci. Technol.*, 2:61–64, 1987.
- [Dre55] G. Dresselhaus. Spin-orbit coupling effects in zinc blende structures. *Phys. Rev.*, 100:580–586, 1955.
- [dSM88] C. E. T. Gonçalves da Silva and E. E. Mendez. Resonant tunneling via landau levels in $GaAs - Ga_{1-x}Al_xAs$ heterostructures. *Phys. Rev. B*, 38:3994–3997, 1988.
- [EC74] L. Esaki and L. L. Chang. New transport phenomenon in a semiconductor ‘super-lattice’. *Phys. Rev. Lett.*, 33:495–498, 1974.

- [ERR01] Al. L. Efros, E. I. Rashba, and M. Rosen. Paramagnetic ion-doped nanocrystal as a voltage-controlled spin filter. *Phys. Rev. Lett.*, 87:206601, 2001.
- [Esa73] Leo Esaki. Long journey into tunneling. *Nobel Lecture*, 1973.
- [ET70] L. Esaki and R. Tsu. Superlattice and negative differential conductivity. *IBM J. Res. Dev.*, 14:61, 1970.
- [FGO⁺03] R. Fiederling, P. Grabs, W. Ossau, G. Schmidt, and L. W. Molenkamp. Detection of electrical spin injection by light-emitting diodes in top- and side-emission configurations. *Appl. Phys. Lett.*, 82:2160–2162, 2003.
- [FHS90] H. A. Fertig, Song He, and S. Das Sarma. Elastic-scattering effects on resonant tunneling in double-barrier quantum-well structures. *Phys. Rev. B*, 41:3596–3607, 1990.
- [FJ01] A. Fert and H. Jaffrès. Conditions for efficient spin injection from a ferromagnetic metal into a semiconductor. *Phys. Rev. B*, 64:184420, 2001.
- [FK86] J. K. Furdyna and J. Kossut. *Semiconductors and Semimetals*, volume 25. Academic, Boston, 1986.
- [FKR⁺99] R. Fiederling, M. Keim, G. Reuscher, W. Ossau, G. Schmidt, A. Waag, and L. W. Molenkamp. Injection and detection of a spin-polarized current in a light-emitting diode. *Nature*, 402:787–790, 1999.
- [FRB04] J. Fernández-Rossier and L. Brey. Ferromagnetism mediated by few electrons in a semimagnetic quantum dot. *Phys. Rev. Lett.*, 93:117201, 2004.
- [FS89] H. A. Fertig and S. Das Sarma. Elastic scattering in resonant tunneling systems. *Phys. Rev. B*, 40:7410–7412, 1989.
- [Fur88] J. K. Furdyna. Diluted magnetic semiconductors. *Journal of Applied Physics*, 64(4):R29–R64, 1988.
- [Gal79] R. R. Galazka. *Physics of Semiconductors*. Institute of Physics, Bristol, 1979.
- [GBGV91] Y. Galvao Gobato, J. M. Berroir, Y. Guldner, and J. P. Vieren. Selection-rule breakdown in coherent resonant tunneling in a tilted magnetic field. *Phys. Rev. B*, 44:13795–13798, 1991.
- [GKF⁺01] Th. Gruber, M. Keim, R. Fiederling, G. Reuscher, W. Ossau, G. Schmidt, L. W. Molenkamp, and A. Waag. Electron spin manipulation using semimagnetic resonant tunneling diodes. *Appl. Phys. Lett.*, 78:1101–1103, 2001.
- [GPF79] J. A. Gaj, R. Planel, and G. Fishman. Relation of magneto-optical properties of free excitons to spin alignment of Mn^{2+} ions in $Cd_{1-x}Mn_xTe$. *Solid State Commun.*, 29:435, 1979.

- [GRV⁺03] P. Gambardella, S. Rusponi, M. Veronese, S. S. Dhesi, C. Grazioli, A. Dallmeyer, I. Cabria, R. Zeller, P. H. Dederichs, K. Kern, C. Carbone, and H. Brune. Giant magnetic anisotropy of single cobalt atoms and nanoparticles. *Science*, 300:1130–1133, 2003.
- [GTC87a] V. J. Goldman, D. C. Tsui, and J. E. Cunningham. Evidence for lo-phonon-emission-assisted tunneling in double-barrier heterostructures. *Phys. Rev. B*, 36:7635–7637, 1987.
- [GTC87b] V. J. Goldman, D. C. Tsui, and J. E. Cunningham. Resonant tunneling in magnetic field: Evidence for space-charge buildup. *Phys. Rev. B*, 35:9387–9390, 1987.
- [HGPB95] C. Van Hoof, J. Genoe, J. C. Portal, and G. Borghs. Charge accumulation in the two-dimensional electron gas emitter of a resonant-tunneling diode. *Phys. Rev. B*, 52:1516–1519, 1995.
- [HGQ91] Pawel Hawrylak, Marek Grabowski, and J. J. Quinn. Tunneling in a periodic array of semimagnetic quantum dots. *Phys. Rev. B*, 44:13082–13084, 1991.
- [HK86] Naoki Harada and Shigeru Kuroda. Lifetime of resonant state in resonant tunneling system. *Japanese Journal of Applied Physics*, 25(11):L871–L873, 1986.
- [HK03] P. Hawrylak and M. Korkusinski. Single quantum dots: Fundamentals, applications, and new concepts. *Topics in Appl. Phys.*, 9:25–92, 2003.
- [HME⁺00] D. M. Hoffman, B. K. Meyer, A. I. Ekimov, I. A. Merkulov, Al. L. Efros, M. Rosen, G. Couino, T. Gacoin, and J. P. Boilot. Giant internal magnetic fields in mn doped nanocrystal quantum dots. *Phys. Rev. Lett.*, 114:547–550, 2000.
- [HPE⁺89] M. Helm, F. M. Peeters, P. England, J. R. Hayes, and E. Colas. Resonant tunneling in a transverse magnetic field: Transition from the electric to the magnetic quantum limit. *Phys. Rev. B*, 39:3427–3430, 1989.
- [HPM⁺01] R. J. A. Hill, A. Patané, P. C. Main, L. Eaves, B. Gustafson, M. Henini, S. Tarucha, and D. G. Austing. Magnetotunneling spectroscopy of an individual quantum dot in a gated tunnel diode. *Appl. Phys. Lett.*, 79:3275–3277, 2001.
- [IP96] G. Iannaccone and B. Pellegrini. Compact formula for the density of states in a quantum well. *Phys. Rev. B*, 53:2020–2025, 1996.
- [JHLK⁺02] E. Johnston-Halperin, D. Lofgreen, R. K. Kawakami, D. K. Young, L. Col-dren, A. C. Gossard, and D. D. Awschalom. Spin-polarized zener tunneling in $(Ga, Mn)As$. *Phys. Rev. B*, 65:041306, 2002.
- [Kan69] E. O. Kane. *Tunneling Phenomena in Solids*. Plenum, New York, 1969.
- [Kan98] B. E. Kane. A silicon-based nuclear spin quantum computer. *Nature*, 393:133–137, 1998.

- [KJP⁺90] E. T. Koenig, B. Jogai, M. J. Paulus, C. I. Huang, and C. A. Bozada. Charge-quantization effects on current-voltage characteristics of *AlGaAs/GaAs* resonant tunneling diodes with spacer layers. *Appl. Phys. Lett.*, 68(7):3425–3430, 1990.
- [KKL⁺00] M. Kim, C. S. Kim, S. Lee, J. K. Furdyna, and M. Dobrowolska. Band offset determination in *ZnSe*-based heterostructures involving *ZnBeSe*. *Journal of Crystal Growth*, 214-215:325–329, 2000.
- [KOT⁺01] M. Kohda, Y. Ohno, K. Takamura, F. Matsukura, and H. Ohno. A spin esaki diode. *Jpn. J. Appl. Phys.*, 40:L1274–L1276, 2001.
- [KYK⁺02] D. Keller, D. R. Yakovlev, B. König, W. Ossau, Th. Gruber, A. Waag, L. W. Molenkamp, and A. V. Scherbakov. Heating of the magnetic ion system in (Zn,Mn)Se/(Zn,Be)Se semimagnetic quantum wells by means of photoexcitation. *Phys. Rev. B*, 65:035313, 2002.
- [LAE⁺89] M. L. Leadbeater, E. S. Alves, L. Eaves, M. Henini, O. H. Hughes, A. Celeste, J. C. Portal, G. Hill, and M. A. Pate. Magnetic field studies of elastic scattering and optic-phonon emission in resonant-tunneling devices. *Phys. Rev. B*, 39:3438–3441, 1989.
- [LB87] Landolt-Börnstein. *New Series III/22a*. Springer-Verlag, Berlin, 1987.
- [LD98] Daniel Loss and David P. DiVincenzo. Quantum computation with quantum dots. *Phys. Rev. A*, 57:120–126, 1998.
- [LFM⁺96] M. L. F. Lerch, D. J. Fisher, A. D. Martin, C. Zhang, and L. Eaves. Charge accumulation over a ration of electrical multistability in a double barrier structure. *Surf Science*, 361:226–230, 1996.
- [LKW⁺98] U. Lunz, M. Keim, A. Waag, W. Faschinger, and G. Landwehr. Transverse magnetic field studies in *ZnSe/BeTe* resonant tunneling structures. *Appl. Phys. Lett.*, 72:2120–2122, 1998.
- [LL77] L. D. Landau and E. M. Lifshitz. *Quantum Mechanics (Non-Relativistic Theory)*. Pergamon Pres, Oxford, 1977.
- [LMS⁺94] M. L. F. Lerch, A. D. Martin, P. E. Simmonds, L. Eaves, and M. L. Leadbeater. A new technique for directly probing the intrinsic tristability and its temperature dependence in a resonant tunneling diode. *Solid State Electron.*, 37:961, 1994.
- [Lur85] S. Luryi. Frequency limit of double-barrier resonant-tunneling oscillators. *Appl. Phys. Lett.*, 47:490–492, 1985.
- [Lur89] S. Luryi. Coherent versus incoherent resonant tunneling and implications for fast devices. *Superlattices and Microstructures*, 5:375–382, 1989.

- [MBSA01] I. Malajovich, J. J. Berry, N. Samarth, and D. D. Awschalom. Persistent sourcing of coherent spins for multifunctional semiconductor spintronics. *Nature*, 411:770–772, 2001.
- [MdBD⁺02] V.F. Motsnyi, J. de Boeck, J. Das, W. Van Roy, G. Borghs, E. Goovaerts, and V.I. Safarov. Electrical spin injection in a ferromagnet/tunnel barrier/semiconductor heterostructure. *Appl. Phys. Lett.*, 81:265–267, 2002.
- [MGJ⁺03] R. Mattana, J.-M. George, H. Jaffrès, F. Nguyen Van Dau, A. Fert, B. Lépine, A. Guivarc’h, and G. Jézéquel. Electrical detection of spin accumulation in a p-type gaas quantum well. *Phys. Rev. Lett.*, 90:166601, 2003.
- [MGN⁺04] S. Mackowski, T. Gurung, T. A. Nguyen, H. E. Jackson, L. M. Smith, G. Karczewski, and J. Kossut. Optically-induced magnetization of cdmnte self-assembled quantum dots. *Appl. Phys. Lett.*, 84:3337–3339, 2004.
- [MLSE94] A. D. Martin, M. L. F. Lerch, P. E. Simmonds, and L. Eaves. Observation of intrinsic tristability in a resonant tunneling structure. *Appl. Phys. Lett.*, 64:1248–1250, 1994.
- [MTB⁺01] P. Möck, T. Topuria, N. D. Browning, L. Titova, M. Dobrowolska, S. Lee, and J. K. Furdyna. Self-ordered cdse quantum dots in znse and (zn,mn)se matrices assessed by transmission electron microscopy and photoluminescence spectroscopy. *J. Electron. Mater.*, 30:748–755, 2001.
- [Ohn02] H. Ohno. Special issue on semiconductor spintronics. *Semicond. Sci. Tech.*, 17(4), 2002.
- [OMW90] H. Ohno, E. E. Mendez, and W. I. Wang. Effects of carrier mass differences on the current-voltage characteristics of resonant tunneling structures. *Appl. Phys. Lett.*, 56:1793–1795, 1990.
- [OYB⁺99] Y. Ohno, D. K. Young, B. Beschoten, F. Matsukura, H. Ohno, and D. D. Awschalom. Electrical spin injection in a ferromagnetic semiconductor heterostructure. *Nature*, 402:790–792, 1999.
- [PBT89] G. Platero, L. Brey, and C. Tejedor. Coherent and sequential tunneling in double barriers with transverse magnetic fields. *Phys. Rev. B*, 40:8548–8551, 1989.
- [PPV⁺82] A. Petrou, D. L. Peterson, S. Venugopalan, R. R. Galazka, A. K. Ramdas, and S. Rodriguez. Zeeman effect of the magnetic excitations in a diluted magnetic semiconductor: A raman scattering study of $Cd_{1-x}Mn_xTe$. *Phys. Rev. Lett.*, 48:1036–1039, 1982.
- [Pri87] P. J. Price. Coherence of resonant tunneling in heterostructures. *Phys. Rev. B*, 36:1314, 1987.
- [Pri92] Peter J. Price. Resonant tunneling via an accumulation layer. *Phys. Rev. B*, 45:9042–9045, 1992.

- [RA84] B. Ricco and M. Ya. Azbel. Physics of resonant tunneling. the one-dimensional double-barrier case. *Phys. Rev. B*, 29:1970, 1984.
- [Ras60a] E. I. Rashba. *Fiz. Tverd. Tela (Leningrad)*, 2:1224, 1960.
- [Ras60b] E. I. Rashba. *Sov. Phys. Solid State*, 2:1109, 1960.
- [Ras00] E. I. Rashba. Theory of electrical spin injection: Tunnel contacts as a solution of the conductivity mismatch problem. *Phys. Rev. B*, 62:R16267–R16270, 2000.
- [RBG⁺03] C. Rüster, T. Borzenko, C. Gould, G. Schmidt, L. W. Molenkamp, X. Liu, T. J. Wojtowicz, J. K. Furdyna, Z. G. Yu, and M. E. Flatté. Very large magnetoresistance in lateral ferromagnetic (ga,mn)as wires with nanoconstrictions. *Phys. Rev. Lett.*, 91:216602, 2003.
- [RBMC04] D. Rugar, R. Budakian, H. J. Mamin, and B. W. Chui. Single spin detection by magnetic resonance force microscopy. *Nature*, 430:329–332, 2004.
- [RLZ59] Laura M. Roth, Benjamin Lax, and Solomon Zwerdling. Theory of optical magneto-absorption effects in semiconductors. *Phys. Rev.*, 114:90–104, 1959.
- [RSL00] Patrik Recher, Eugene V. Sukhorukov, and Daniel Loss. Quantum dot as spin filter and spin memory. *Phys. Rev. Lett.*, 85:1962, 2000.
- [Sch68] L. I. Schiff. *Quantum Mechanics*. 3rd ed. New York, McGraw-Hill, 1968.
- [SFM⁺00] G. Schmidt, D. Ferrand, L. W. Molenkamp, A. T. Filip, and B. J. van Wees. Fundamental obstacle for electrical spin injection from a ferromagnetic metal into a diffusive semiconductor. *Phys. Rev. B*, 62:R4790–R4793, 2000.
- [SGG⁺04] G. Schmidt, C. Gould, P. Grabs, A. M. Lunde, G. Richter, A. Slobodskyy, and L. W. Molenkamp. Spin injection in the nonlinear regime: Band bending effects. *Phys. Rev. Lett.*, 92:226602, 2004.
- [SGS⁺03] A. Slobodskyy, C. Gould, T. Slobodskyy, C. R. Becker, G. Schmidt, and L. W. Molenkamp. Voltage-controlled spin selection in a magnetic resonant tunneling diode. *Phys. Rev. Lett.*, 90:246601, 2003.
- [Sha86] Y. Shapira. Magnetoresistance and hall effect near the metal-insulator transition of $Cd_{1-x}Mn_xSe$. *Phys. Rev. B*, 34:4187–4198, 1986.
- [SKW⁺94] J. S. Scott, J. P. Kaminski, M. Wanke, S. J. Allen, D. H. Chow, M. Lui, and T. Y. Liu. Terahertz frequency response of an $In_{0.53}Ga_{0.47}As/AlAs$ resonant-tunneling diode. *Appl. Phys. Lett.*, 64(15):1995–1997, 1994.
- [SL85] A. D. Stone and P. A. Lee. Effect of inelastic processes on resonant tunneling in one dimension. *Phys. Rev. Lett.*, 54:1196, 1985.

- [SMP02] D. Sánchez, A.H. MacDonald, and G. Platero. Field-domain spintronics in magnetic semiconductor multiple quantum wells. *Phys. Rev. B*, 65:035301–035311, 2002.
- [SO87] Y. Shapira and Jr. N. F. Oliveira. High-field magnetization steps and the nearest-neighbor exchange constant in $Cd_{1-x}Mn_xS$, $Cd_{1-x}Mn_xTe$, and $Zn_{1-x}Mn_xSe$. *Phys. Rev. B*, 35:6888–6893, 1987.
- [SRG⁺01] G. Schmidt, G. Richter, P. Grabs, C. Gould, D. Ferrand, and L.W. Molenkamp. Large magnetoresistance effect due to spin injection into a nonmagnetic semiconductor. *Phys. Rev. B*, 87:227203, 2001.
- [Stu70] D. J. Stukel. Energy-band structure of BeS , $BeSe$, and $BeTe$. *Phys. Rev. B*, 2:1852, 1970.
- [TE73] R. Tsu and L. Esaki. Tunneling in finite superlattice. *Appl. Phys. Lett.*, 22:562, 1973.
- [TIM⁺98] A. S. G. Thornton, T. Ihn, P. C. Main, L. Eaves, and M. Henini. Observation of spin splitting in single inas self-assembled quantum dots in alas. *Appl. Phys. Lett.*, 73:354–356, 1998.
- [TLB⁺96] L. Thomas, F. Lioni, R. Ballou, D. Gatteschi, R. Sessoli, and B. Barbara. Macroscopic quantum tunnelling of magnetization in a single crystal of nanomagnets. *Nature*, 383:145–147, 1996.
- [TvODP84] A. Twardowski, M. von Ortenberg, M. Demianiuk, and R. Pauthenet. Magnetization and exchange constants in $Zn_{1-x}Mn_xSe$. *Solid State Communications*, 51(11):849–852, 1984.
- [VLP⁺00] E. E. Vdovin, A. Levin, A. Patané, L. Eaves, P. C. Main, Yu. N. Khanin, Yu. V. Dubrovskii, M. Henini, and G. Hill. Imaging the electron wave function in self-assembled quantum dots. *Science*, 290:122–124, 2000.
- [WAB⁺01] S. A. Wolf, D. D. Awschalom, R. A. Buhrman, J. M. Daughton, S. von Molnár, M. L. Roukes, A. Y. Chtchelkanova, and D. M. Treger. Spintronics: A spin-based electronics vision for the future. *Science*, 294:1488–1495, 2001.
- [WC91] C. R. Wie and Y. W. Choi. Designing resonant tunneling structures for increased peak current density. *Appl. Phys. Lett.*, 58(10):1077–1079, 1991.
- [WCL⁺90] J. S. Wu, C. Y. Chang, C. P. Lee, K. H. Chang, D. G. Liu, and D. C. Liou. Resonant tunneling of electrons from quantized levels in the accumulation layer of double-barrier heterostructures. *Appl. Phys. Lett.*, 57(22):2311–2312, 1990.
- [WLC⁺91] J. S. Wu, C. P. Lee, C. Y. Chang, K. H. Chang, D. G. Liu, and D. C. Liou. Improved $AlGaAs/GaAs$ double-barrier resonant tunneling structures using two-dimensional source electrons. *Appl. Phys. Lett.*, 69(2):1122–1123, 1991.

- [WLP⁺88] E. Wolak, K. L. Lear, P. M. Pitner, E. S. Hellman, B. G. Park, T. Weil, J. S. Harris, Jr., and D. Thomas. Elastic scattering centers in resonant tunneling diodes. *Appl. Phys. Lett.*, 53(3):201–203, 1988.
- [WS94] T. Wei and S. Stapleton. Effect of spacer layers on capacitance of resonant tunneling diodes. *Journal of Applied Physics*, 76(2):1287–1290, 1994.
- [YF02] Z. G. Yu and M. E. Flatté. Electric-field dependent spin diffusion and spin injection into semiconductors. *Phys. Rev. B*, 66:201202(R), 2002.
- [YTFP95] W. Y. Yu, A. Twardowski, L. P. Fu, and A. Petrou. Magnetoanisotropy in $Zn_{1-x}Mn_xSe$ strained epilayers. *Phys. Rev. B*, 51:9722–9727, 1995.
- [ZC92] Nanzhi Zou and K. A. Chao. Inelastic electron resonant tunneling through a double-barrier nanostructure. *Phys. Rev. Lett.*, 69:3224–3227, 1992.
- [ZLT⁺90] A. Zaslavsky, Yuan P. Li, D. C. Tsui, M. Santos, and M. Shayegan. Transport in transverse magnetic fields in resonant tunneling structures. *Phys. Rev. B*, 42:1374–1380, 1990.
- [ZTSS89] A. Zaslavsky, D. C. Tsui, M. Santos, and M. Shayegan. Magnetotunneling in double-barrier heterostructures. *Phys. Rev. B*, 40:9829–9833, 1989.

List of publications

- I *Ferromagnetic ordering in diluted magnetic semiconductors*, A.H. Slobodskyy, V.K. Dugaev, and M. Vieira, *Condensed Matter Physics*, Vol. 5, No. 3(31), 531 (2002)
- II *Mechanism of ferromagnetism in diluted magnetic semiconductors at low carrier density*, V.K. Dugaev, V.I. Litvinov, J. Barnas, A.H. Slobodskyy, W. Dobrowolski, and M. Vieira, *Journal of Superconductivity: Incorporating Novel Magnetism*, Vol. 16, No. 1, 67 (2003)
- III *Molecular beam epitaxial growth of CdMnSe on InAs and AlGaSb*, Peter Grabs, Anatoliy Slobodskyy, Georg Richter, Roland Fiederling, Charles Gould, Charles R. Becker, Georg Schmidt, and Laurens W. Molenkamp, *Journal of Crystal Growth*, 251 (1-4), 347-352 (2003)
- IV *Ferromagnetism in diluted magnetic semiconductors at low carrier density*, V.K. Dugaev, V.I. Litvinov, J. Barnas, A.H. Slobodskyy, W. Dobrowolski, and M. Vieira, *Physica Status Solidi B*, Vol. 236, No. 2, 507 (2003)
- V *Voltage-Controlled Spin Selection in a Magnetic Resonant Tunneling Diode*, A. Slobodskyy, C. Gould, T. Slobodskyy, C. R. Becker, G. Schmidt, and L.W. Molenkamp, *Phys. Rev. Lett.* 90, 246601 (2003)
- VI *Spin Injection in the Nonlinear Regime: Band Bending Effects*, G. Schmidt, C. Gould, P. Grabs, A. M. Lunde, G. Richter, A. Slobodskyy, and L. W. Molenkamp, *Phys. Rev. Lett.* 92, 226602 (2004)
- VII *Self Assembled II-VI Magnetic Quantum Dot as a Voltage-Controlled Spin-Filter*, C. Gould, A. Slobodskyy, T. Slobodskyy, P. Grabs, D. Supp, P. Hawrylak, F. Qu, G. Schmidt, and L.W. Molenkamp, Submitted for publication in *Phys. Rev. Lett.*
- VIII *Resonant tunneling diode with spin polarized injector*, A. Slobodskyy, D. Sánchez, C. Gould, T. Slobodskyy, G. Schmidt, and L.W. Molenkamp, Submitted for publication in *Appl. Phys. Lett.*

APPENDIX

Spin Injection in the Nonlinear Regime: Band Bending Effects

G. Schmidt, C. Gould, P. Grabs, A. M. Lunde,* G. Richter, A. Slobodskyy, and L.W. Molenkamp

Physikalisches Institut (EP3), Universität Würzburg, Am Hubland, 97074 Würzburg, Germany

(Received 14 June 2002; published 4 June 2004)

We report on electrical spin-injection measurements into a nonmagnetic semiconductor in the nonlinear regime. For voltage drops across the interface larger than a few mV the spin-injection efficiency decreases strongly. The effect is caused by repopulation of the minority spin level in the magnetic semiconductor due to band bending at the interface.

DOI: 10.1103/PhysRevLett.92.226602

PACS numbers: 72.25.Dc, 72.25.Hg, 81.05.Dz

Electrical spin injection into semiconductors can be understood [1] using a current-imbalance model originally developed for metals [2]. This model reveals [1] the importance of a conductance mismatch between ferromagnetic metals and semiconductor that precludes spin injection. While in the meantime several methods of avoiding the conductance mismatch have been proposed, by far the most robust route towards spin injection to date [3,4] is the use of dilute II-VI magnetic semiconductors (DMSs) that exhibit the giant Zeeman effect [5], have a conductivity comparable to that of nonmagnetic semiconductors, and can boast spin polarizations close to 100% at a small applied magnetic field. Recently, we used a simple DMS—nonmagnetic semiconductor (NMS) heterostructure [consisting of (Zn,Mn,Be)Se as DMS and lattice matched (Zn,Be)Se as NMS] to demonstrate [4] the magnetic field dependence of the spin-induced boundary resistance, which increases with field as the magnetization of the paramagnetic DMS increases. The experiments reported in Ref. [4] were all done in the regime of linear response, where the current-imbalance model is appropriate.

However, spin-injection experiments in semiconductors allow one to very easily enter the regime of nonlinear response, where corrections to the model of Ref. [1] are necessary. In this Letter we report on spin-injection measurements in the nonlinear regime. We find that a first correction to [1] occurs due to the strong effects that band bending and charge accumulation have on the nonlinear transport. We model the observed phenomena by generalizing Ref. [1] to include these typical semiconductor phenomena, and obtain good agreement with the experiments. It should be noted that the effects found here are of a fundamentally different nature than the drift-induced effects discussed recently by Yu and Flatté [6] (which occur at still larger electric fields [7]).

The devices are all-II-VI semiconductor heterostructure fabricated by molecular beam epitaxy, consisting of three semiconductor layers. From bottom to top these layers are a nonmagnetic *n*-type $\text{Zn}_{0.97}\text{Be}_{0.03}\text{Se}$ layer (thickness 500 nm, $n \approx 10^{19} \text{ cm}^{-3}$), a dilute magnetic $\text{Zn}_{0.89}\text{Be}_{0.05}\text{Mn}_{0.06}\text{Se}$ layer (thickness 100 nm, $n \approx 5 \times 10^{18} \text{ cm}^{-3}$), which acts as a spin aligner, and a top layer of

10 nm highly *n*-doped ZnSe ($n \approx 2 \times 10^{19} \text{ cm}^{-3}$). The latter ensures good quality Ohmic contacts and was covered *in situ* with aluminum. In the Al layer, $200 \times 250 \mu\text{m}$ contact pads were defined and used as a mask for a subsequent wet etching step down to the $\text{Zn}_{0.97}\text{Be}_{0.03}\text{Se}$, leaving only two contacts and the transport layer in between. The resulting sample is schematically shown as an inset in Fig. 1.

The samples were inserted in a magnetocryostat and their transport properties were determined at 1.6, 3, 4.2, and 6 K. The magnetoresistance of the devices was measured using dc techniques and a quasi-four-probe geometry, excluding the wiring resistance of the setup, while still including the contact resistance of the device [8]. For bias voltages V_{bias} in the regime of linear response (300 μV or less) the device showed a positive magnetoresistance. Figure 1 plots the relative magnetoresistance $\Delta R/R$ for a sample with a distance $x_0 = 10 \mu\text{m}$ between the contact pads, taken at 1.6 K, where the zero-field resistance $R = 420 \Omega$. As described in Ref. [4], the magnetoresistance results from the increase of the spin-induced boundary resistance with magnetic field. All

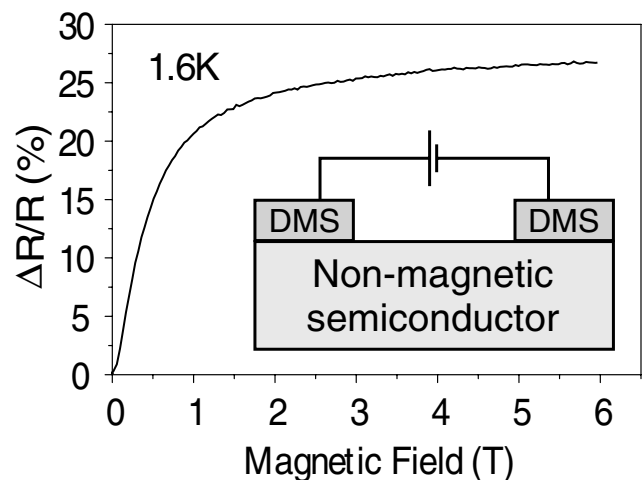


FIG. 1. Inset: spin injection device used in the experiment consisting of a nonmagnetic semiconductor layer with two DMS top contacts. The graph gives the resistance change $\Delta R/R$ versus magnetic field B .

data discussed here were taken on the same sample as in Fig. 1; we verified that the effects discussed occur in samples with varying doping concentrations and dimensions. We found experimentally that both R and the saturated magnetoresistance $\Delta R/R \approx 0.25$ are independent of temperature in the investigated range.

We now leave the regime of linear response and in Fig. 2 plot the current versus V_{bias} curves for the sample at $B = 0$ T, $B = 0.57$ T, where the magnetoresistance is strongly positive, and $B = 3$ T, when the magnetoresistance is well saturated. At first glance, the curves of Fig. 2 appear rather linear and fairly similar; however, a careful inspection shows a crucial difference between the curves, which is put into evidence in the inset of the figure, where we plot the difference in voltage drop between the 0.57 T curve and the $B = 0$ T curve. It is clear that at low currents, an additional voltage drop is observed in the at field curve and that this additional voltage drop vanishes as the current is increased.

The results are easier to view when, instead of current versus V_{bias} plots, we plot the magnetoresistance of the sample. The main experimental result of this Letter is summarized in Fig. 3(a). When the applied voltage is increased, a pronounced and very rapid drop of the magnetoresistance is observed, reducing the effect by 2 or more orders of magnitude on applying a voltage of around 10 mV across the junction. At higher voltages, the device resistance is no longer dependent on the magnetic field, indicating that a reduction of the spin injection is responsible for the effect. The experimental data in Fig. 3(a) were taken starting from three different values of $\Delta R/R$ (i.e., at different values of the magnetic field B) in the linear response regime (i.e., $\Delta R/R \approx 0.05, 0.1,$ and 0.15 , respectively), at the four different temperatures mentioned above. We chose starting points below the saturation

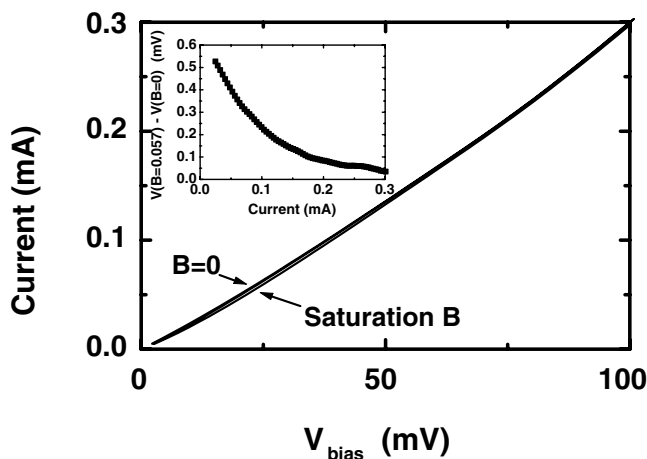


FIG. 2. Current versus voltage curves for the sample in B fields of 0, 0.57, or 3 T. On this scale, the 0 and 0.57 T curves cannot be distinguished. Inset: the difference in voltages between the 0.57 and the 0 T curve is plotted as a function of current, showing that the two curves are, in fact, remarkably different.

226602-2

tion value of the magnetoresistance because at saturation, the simulations can give only a lower limit for the Zeeman splitting, while below saturation, the Zeeman splitting can be determined exactly.

Obviously, the nonlinearities show a marked temperature dependence. Moreover, while the horizontal axis displays the bias voltage applied to the device, only the drop over the junction V_j (roughly $V_j \approx 0.15V_{\text{bias}}$) contributes to the quenching of the effect, and it is therefore V_j that illustrates the energy scales involved in the nonlinearities. We detail below how V_j is defined and can be calculated from V_{bias} .

The drop of the magnetoresistance can be understood if we combine the model for diffusive spin-polarized transport with the band structure of the semiconductor heterostructure. When a current is driven from a

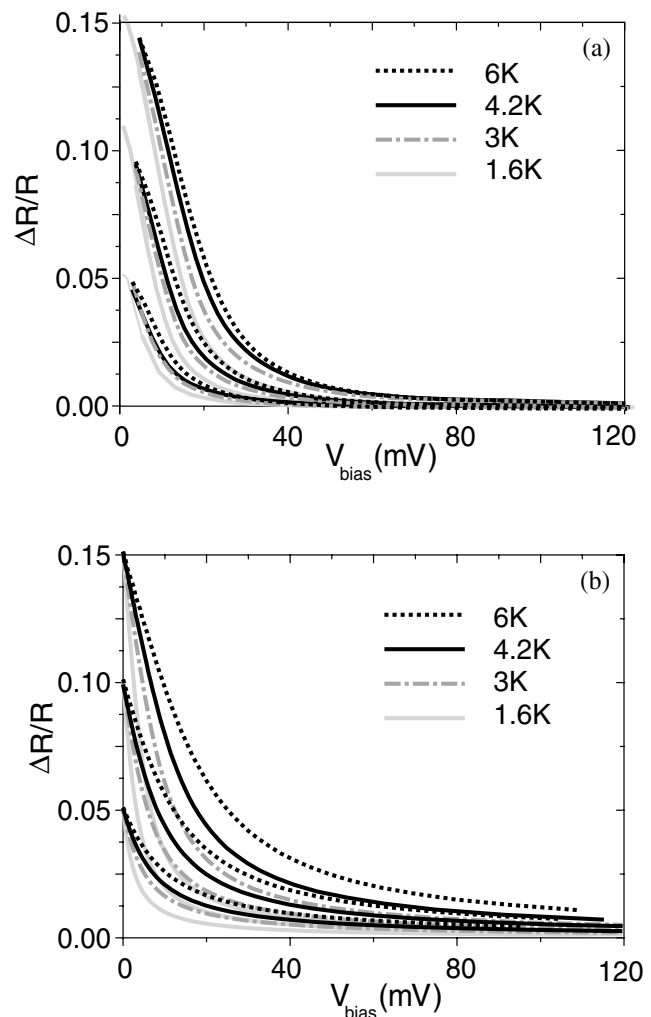


FIG. 3. (a) Experimental and (b) theoretical nonlinear magnetoresistance $\Delta R/R$ data plotted as a function of the applied voltage V_{bias} . (Note that only $V_j \approx 0.15V_{\text{bias}}$ drops over the interface, as described in the text.) To facilitate comparison between experiment and theory, curves are plotted starting at several fixed values of $\Delta R/R$ (obtained by carefully adjusting B), for temperatures of 1.6, 3, 4.2, and 6 K. The parameters involved in the modeling are discussed in the text.

226602-2

spin-polarized material into a nonpolarized material, the electrochemical potentials for spin-up (μ^\uparrow) and spin-down (μ^\downarrow) split at the interface. In linear response, the length scale of this splitting is given by the spin scattering length of each material. The situation is depicted in Fig. 4, where the Zeeman-split conduction band (full drawn lines) and relevant potentials (dash-dotted lines) of the DMS are shown on the left side of the figure. The interface is indicated by the dotted vertical line at $x = 0$, with the NMS in the right half of the plane. The splitting of μ^\uparrow and μ^\downarrow is the driving force which leads to a spin-polarized current in the nonmagnetic material. Because the conductivities for spin-up and spin-down are equal in the NMS, only a difference in the derivative of the electrochemical potential can lead to different currents in both spin channels. Since the *electrical* potential must

be equal for both spin directions, this difference can be introduced only through the *chemical* potential, i.e., by spin accumulation. Spin injection thus leads to a potential drop at the interface which drives the spin conversion. This voltage drop, which may alternatively be regarded as a spin-induced boundary resistance, is indicated in Fig. 4 by the potential difference at $x = 0$ between the thin drawn lines, denoted $\mu_{\text{DMS}}^{\text{av}}$ and $\mu_{\text{NMS}}^{\text{av}}$, that depict the conductivity-weighted average of the electrochemical potential in DMS and NMS, respectively.

While in the NMS the splitting of the Fermi levels is symmetrical because the conductivities for spin-up and spin-down electrons are identical, in the DMS, the splitting for the majority- [$c^\uparrow \equiv \mu_{\text{DMS}}^\uparrow(0) - \mu_{\text{DMS}}^{\text{av}}(0)$] and minority- [$c^\downarrow \equiv \mu_{\text{DMS}}^{\text{av}}(0) - \mu_{\text{DMS}}^\downarrow(0)$] spin electrons can, in one dimension, be expressed as [4,9]

$$c^\uparrow, c^\downarrow = -\frac{\lambda_N}{\sigma_N(1 + e^{-x_0/\lambda_N} + 2(\lambda_N/x_0)e^{-x_0/\lambda_N}) + (\lambda_N\sigma_D/\sigma_N\lambda_D)(1 - \beta^2)} I\beta(\beta \pm 1) \quad (1)$$

where in the numerator the plus (minus) sign applies to c^\uparrow (c^\downarrow), respectively. In Eq. (1), λ_D , λ_N , σ_D , σ_N are the spin flip length and the conductivity in the DMS and the NMS, respectively, x_0 is the spacing between the contacts, I is the current, and β is the degree of spin polarization in the bulk of the contacts. Note that c^\uparrow and c^\downarrow are defined setting $\mu_{\text{DMS}}^{\text{av}}(0)$ as the reference level for the energy scale; i.e., $\mu_{\text{DMS}}^{\text{av}}(0) = 0$. For the potential drop ΔU at the interface, and the resulting magnetoresistance, we simply have

$$e\Delta U = \mu_{\text{DMS}}^{\text{av}}(0) - \mu_{\text{NMS}}^{\text{av}}(0) = (c^\uparrow + c^\downarrow)/2, \quad (2a)$$

$$\Delta R = \Delta U/I, \quad (2b)$$

where e is the fundamental charge. Equations (1) and (2) are quite general and describe spin injection in metals as well as semiconductors—but only in the linear regime. The magnitude of the Fermi-level splitting (and thus of ΔU) is different for different types of junctions: since the spin-polarized current is driven solely by the spin accumulation, the Fermi-level splitting has to be of the order of the current imbalance between the spin channels times the resistivity of the normal metal. When magnet and nonmagnet are both semiconductors as in the present experiment, the splitting can easily be in the range of mV. This implies that in a spin-injecting DMS the Fermi energy, the Zeeman splitting and the Fermi-level splitting are all in the range of mV, and nonlinear effects are to be expected for bias of similar magnitude.

This situation, applied to the present experiment, is pictured in some detail in Fig. 4. The conduction band of the NMS is some tens of mV below that of the DMS, which is split by the Zeeman energy into two subbands, $E_{\text{C}\downarrow}^{\text{DMS}}$ and $E_{\text{C}\uparrow}^{\text{DMS}}$. From previous spin-injection experiments [3,4] and from spin flip Raman scattering we know that the DMS is fully spin polarized at low temperatures and moderate magnetic fields, which recent band structure calculations understand as resulting from

the formation of an impurity band [10]. This implies that the Fermi energy is situated above the lower and at least a few mV below the upper Zeeman level.

As discussed above, spin injection will lead to the occurrence of a “built-in potential” ΔU at the interface. This is an actual electrochemical potential step (i.e., not spin dependent). In order to preserve both charge conservation and the band offset at the junction, ΔU has to be compensated by band bending and charging at the interface. In Fig. 4, this is indicated by the dashed lines emanating from $E_{\text{C}\downarrow}^{\text{DMS}}$ and $E_{\text{C}\uparrow}^{\text{DMS}}$. (In principle, one also expects band bending at the NMS side of the junction. For clarity, we have not included this in Fig. 4, nor in

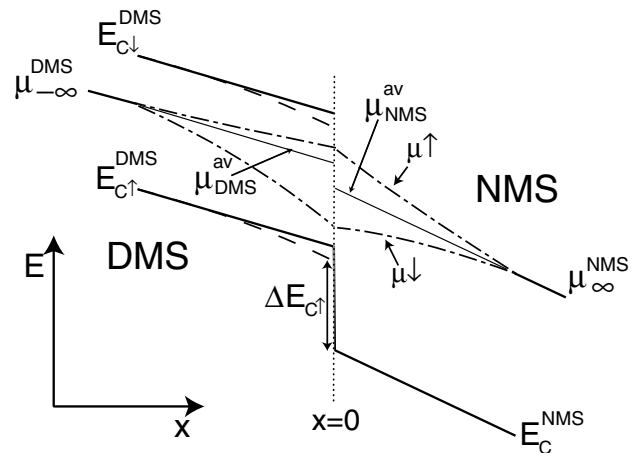


FIG. 4. Diagram of the band bending at the spin-injecting DMS/NMS interface. $\Delta E_{\text{C}\downarrow}$ denotes the location of the conduction band offset between $E_{\text{C}\downarrow}^{\text{DMS}}$ and $E_{\text{C}}^{\text{NMS}}$ when band bending is taken into account; all other symbols are discussed in the text. Note the discontinuity between $\mu_{\text{DMS}}^{\text{av}}$ and $\mu_{\text{NMS}}^{\text{av}}$ at the junction ($x = 0$), which is the potential difference ΔU in Eqs. (2).

the modeling we describe below. Its inclusion is straightforward.)

It is now obvious that the spin-injection process can be seriously affected by any strong band bending, as must occur at higher current levels. At the interface, the majority spin electrochemical potential μ^\uparrow then approaches the upper Zeeman level $E_{\text{Cl}}^{\text{DMS}}$, thus reducing the spin polarization β in the DMS close to the interface. β being close to 1, however, is a prime prerequisite for injecting a highly spin-polarized current into the NMS [1]. We can thus expect the spin injection (and thus the magnetoresistance) to collapse as soon as the band bending starts to reduce β .

Since β and ΔU depend on each other, a modeling of the phenomena as a function of V_{bias} should be done in a self-consistent manner. One can avoid a recursive calculation when starting from a given value of $\Delta R/R$ in the linear response regime (this is the main reason for presenting the data emanating from the same $\Delta R/R$ value in Fig. 3.) We first use Eqs. (1) and (2) to calculate the bulk polarization β in the DMS. In the linear regime, the bulk value of β equals $\beta(x=0)$, the spin polarization at the interface. Assuming Boltzmann statistics, we then directly have the energy splitting between $E_{\text{Cl}}^{\text{DMS}}(0)$ and $\mu^\uparrow(0)$ from

$$\beta(x=0) = \tanh\left[\frac{E_{\text{Cl}}^{\text{DMS}}(0) - e\Delta U - \mu^\uparrow(0)}{2k_{\text{B}}T}\right], \quad (3)$$

where $\Delta U = 0$ for infinitesimally small bias. For modeling the dependence on V_{bias} , we gradually increase ΔU (note that here we assume all band bending to occur in the DMS), calculate the reduced $\beta(x=0)$ using Eq. (3), and substitute this value for the bulk polarization in Eqs. (1) and (2) to calculate $\Delta R/R$. At the same time, ΔU can be converted in a voltage drop across the junction, V_j .

The latter quantity is conveniently accessible for comparison with the experiment. This is because $\Delta R \rightarrow 2\lambda_{\text{N}}/\sigma_{\text{N}}$ for $B, (x_0/\lambda_{\text{N}}) \rightarrow \infty$, as can easily be verified from Eqs. (1) and (2). Experimentally, we have (within our one-dimensional modeling) $\sigma_{\text{N}} = 2.5 \times 10^{-4} \Omega^{-1} \text{cm}$, yielding $\lambda_{\text{N}} = 1.25 \mu\text{m}$. For comparing the experimental [Fig. 3(a)] and theoretical [Fig. 3(b)] plots of the nonlinear behavior, we may now calibrate the voltage axis according to $V_j = I\Delta R + V_{\text{bias}}(\lambda_{\text{N}}/x_0)$.

As to the remaining parameters, we have from experiments on single DMS layers that σ_{D} , converted to one dimension, equals $1.0 \times 10^{-4} \Omega^{-1} \text{cm}$. The only free parameter now left in the model is λ_{D} . Since there is no easy method to measure λ_{D} , and moreover its magnetic field dependence is unknown, the ratio $\lambda_{\text{N}}\sigma_{\text{D}}/\sigma_{\text{N}}\lambda_{\text{D}}$ in Eq. (1) cannot be precisely determined. However, since it is of order unity, and given that the fitting does not strongly depend on the exact value of this ratio, we simply set it equal to 1, yielding $\lambda_{\text{D}} = 0.5 \mu\text{m}$.

The modeling of the band bending effect as described above leads to the plots shown in Fig. 3(b). We find that indeed a few mV of voltage drop across the junction are enough to reduce the spin polarization of the injected current to almost zero. The computed curves closely resemble the experimental results in shape, magnitude, voltage range, and temperature dependence.

At this point, we should address the drift effects introduced by Yu and Flatté [6], which also can induce a reduction of $\Delta R/R$ in our experiments. For the highly (i.e., above the metal-insulator transition) doped samples used here, one can show that drift effects occur only for much higher electric fields than those used here [7]. Moreover, within the drift model one would not expect any temperature dependence for degenerate semiconductors, again in contradiction with the experiments.

In conclusion, we have shown that when spin injection into semiconductors is used beyond the regime of linear response, band bending in the spin-injecting junction can strongly reduce the spin-injection efficiency. Appropriate tailoring of the band structure may be able to circumvent the problems described here.

We acknowledge the financial support of the BMBF, of the DFG (SFB 410), and of the DARPA SPINS program. We thank V. Hock for device fabrication and I. D'Amico, M. Flatté, K. Flensberg, and E. Rashba for useful discussions.

*Present and permanent address: Ørsted Laboratory, Niels Bohr Institute, DK-2100 Copenhagen, Denmark.

- [1] G. Schmidt, D. Ferrand, L.W. Molenkamp, A.T. Filip, and B.J. van Wees, *Phys. Rev. B* **62**, R4790 (2000).
- [2] P.C. van Son, H. van Kempen, and P. Wyder, *Phys. Rev. Lett.* **58**, 2271 (1987); M. Johnson and R.H. Silsbee, *Phys. Rev. B* **35**, 4959 (1987); *Phys. Rev. Lett.* **60**, 377 (1988).
- [3] R. Fiederling, M. Keim, G. Reuscher, W. Ossau, G. Schmidt, A. Waag, and L.W. Molenkamp, *Nature (London)* **402**, 787 (1999).
- [4] G. Schmidt, G. Richter, P. Grabs, D. Ferrand, and L.W. Molenkamp, *Phys. Rev. Lett.* **87**, 227203 (2001).
- [5] J. K. Furdyna, *J. Appl. Phys.* **64**, R29 (1988).
- [6] Z. G. Yu and M. E. Flatté, *Phys. Rev. B* **66**, 235302 (2002).
- [7] I. D'Amico and G. Vignale, *Phys. Rev. B* **69**, 165305 (2004).
- [8] A true four-probe measurement technique is not possible for any sample bigger than the spin flip length in the material, since the voltage leads would be located in a region where the spin splitting has already relaxed.
- [9] G. Schmidt and L.W. Molenkamp, *Semicond. Sci. Technol.* **17**, 310 (2002).
- [10] K. Sato and H. Katayama-Yoshida, *Jpn. J. Appl. Phys.* **40**, L651 (2001).

Curriculum vitae

Personal data:

Birth date: October 24, 1976

Place of birth: Ivano-Frankivsk, Ukraine

Nationality: Ukrainian

School:

1984 - 1986 Public school in Odessa, Ukraine

1986 - 1994 Public school in Chernivchi, Ukraine

University:

1994 - 1999 Student Chernivtsi State University - Y. Fedkovich. Chernivtsi, Ukraine.
Specialized in “Semiconductor physics”

Work after the university:

1999 - 2000 Programmer at various commercial institutions. “Delphi, C++, perl, SQL database, . . . ”

Ph.D. studying:

2000 - 2002 Ph.D. student Chernivtsi Department of the Institute of Materials Sciences Problems, National Academy of Sciences of Ukraine. Chernivtsi, Ukraine “Theory, spintronics”

2002 - 2005 Ph.D. student EP3, Physikalisches Institut der Universität Würzburg. Würzburg, Germany. “Transport investigations of semiconductor structures for spintronics”

Ehrenwörtliche Erklärung

Hiermit versichere ich an Eides statt,

- dass ich die Dissertation eigenständig, d.h. selbständig und ohne Hilfe eines Promotionsberaters angefertigt und keine anderen als die angegebenen Quellen und Hilfsmittel benutzt habe.
- dass die Dissertationsschrift bisher weder in gleicher noch in anderer Form in einem anderen Prüfungsfach vorgelegen hat.

Würzburg, den

(Anatoliy Slobodskyy)

Acknowledgments

I would like to thank to all EP3 members who made the pleasant and friendly working atmosphere. Special thanks to:

- Prof. Dr. L. W. Molenkamp for the possibility of working in EP3 and for the continues support and supervision,
- Privatdozent Dr. G. Schmidt for the possibility of working in his group, useful advices and supervision,
- Dr. C. Gould for the support, useful discussions and supervision of my thesis,
- T. Slobodskyy, P. Grabs, I. Chado for the growth of samples and useful discussions,
- Andreas Gröger, D. Supp, C. Rüster, R. Fiederling, D. Keller, G. Astakhov, R. Scheibner, M. König and V. Daumer for a variety of useful discussions and good working atmosphere in the labs,
- G. Manger and R. Ebert for assistance in cryogenics and general help with the lab equipment. As well as V. Hock for sample processing.